Performance and Core Loss Validation of Concentrated Winding IPMSM with Different Core Treatment

by

Shah Asifur Rahman

A thesis submitted in partial fulfillment of the requirements for the degree of

Doctor of Philosophy
in
Energy Systems

Electrical and Computer Engineering
University of Alberta

ABSTRACT

Designing and selecting the type of electrical machines for hybrid electrical vehicles (HEV) is a particular challenge due to system requirements that include high power and torque densities, low losses, low weight, small installation space and wide speed range with constant power operation. The main objective of this research is to predict the core losses of an interior permanent magnet synchronous machine (IPMSM) in the design stage and verify the losses. The core loss of the machine is affected by the magnetic properties of the core materials. However, even using the same core materials, the magnetic properties such as B-H loop, DC magnetisation and permeability depend on how the core materials were treated.

There are two research phases in this project. In the first stage is simulation to estimate and analyze the core losses are carried out. The simulations include design studies and stress analysis of the designed motor. To ensure that the simulations use accurate material data, toroid and Epstein frame tests are conducted quantifying the effect of material properties and assembly methods on magnetic performance. Finite Element (FE) analysis is used to calculate lumped parameter values, which are used to predict the various performance of the IPMSM over wide speed range. Detailed FE models are used to investigate performance at specific operating conditions.

The second phase quantifies the core loss and motor performance through experimental tests. Factors affect on machine performances such as core losses at open circuit and loaded conditions. Two identical machines are tested. In the first, the core materials are subject to Stress Relief Annealing (SRA). In the second, the core has not been SRA. Experiments verified that SRA machine gives the higher efficiencies in the rage of 2-7.5% compared with non-SRA machine. However both machines are also investigated for different torque point without applying the field weakening current which

gives a comparative study of both machines. The novelty of this work is investigation and verification the harmonic components core losses of the machines from the knowledge of final stage magnetic properties in core materials obtained directly from Epstein frame tester.

To

My Parents

Amatullah Begum & Shah Md. Shahjahan

ACKNOWLEDGEMENTS

I am extremely grateful to my supervisor Professor Andy knight for all his time, guidance, support, enthusiasm, trust, friendly behavior and invaluable advices given to me over the duration of my PhD program. Dr. Knight has taught and encouraged me to meet challenges that I had never before thought possible. His overall commitment to my success in the program is extraordinary praiseworthy.

Very special thanks to the General Motors Canada for their financial support in my research work. I would like to thank my friends and collogues who helped me during my PhD program. Moreover, thanks to Albert Terheide for his excellent support to me; his help in experimental setup is commendable. I would also like to thank the faculty members of Electrical and Computer Engineering Department.

A special thank to my parents, especially my mother Amatullah Begum who motivated me to complete the PhD program successfully and has given great effort selflessly to raise us; my elder brother Arif, younger brother Atiq and my wife Genia for their support in my PhD study. Even my little son Jawad helped me in his way. I also like to thank to my friend Rana for his excellent support to complete my thesis paper. Finally, I would like to thank all of my wonderful friends and colleagues for making my time unforgettable in the University of Alberta.

Contents

LIST OF FIGURES

LIST OF TABLES

LIST OF SYMBOLS

B	Magnetic flux density
Φ	magnetic flux
A	Area
H	Magnetic field strength
N	number of turns
l	effective magnetic path length
i	current
E_{loop}	energy per cycle
W	core loss per unit volume
f	frequency
K_h	hysteresis loss constant
K_e	eddy current loss constant
K_a	excess loss constant
α	Steinmetz constant
γ	coefficient of the empiric formula
δ	coefficients of the empiric formula
P_{Fe}	Iron loss
P_h	Hysteresis loss
P_e	Eddy current loss
H_{irr}	irreversible peak field
ρv	volumetric mass density
w_h	hysteresis loss at sinusoidal voltage
w_e	eddy current loss at sinusoidal voltage
v_{avg}	average rectified voltage
$v_{1,avg}$	average fundamental voltage
v_{rms}	rms supply voltage
$v_{1,rms}$	rms fundamental voltage
B_1	1st harmonics of magnetic field
B_5	5th harmonics of magnetic field
B_7	7th harmonics of magnetic field
ω_s	Mechanical angular speeds
ω_e	electrical angular frequency
P	pole pair number
K_{w1}	fundamental winding factor
S	sequence of conductors of one phase
n_l	number of layers
Q	slot numbers
$v_s(t)$	instantaneous secondary voltage
N_s	number of secondary turns
$B(t)$	instantaneous flux density
T	torque
λ_{pm}	magnet flux linkage
L_d	*d* axis inductances
L_q	*q* axis inductances
I_d	*d* axis current
I_q	*q* axis current
T_m	magnet torque
T_r	reluctance torque

λ_d	*d* axis flux linkage
λ_q	*q* axis flux linkage
ψ_{pm}	the pm flux
P_q	permeance coefficient
P_d	permeance coefficient
k_w	winding factor
N_{ph}	number of turns per phase
$V_{\mathrm{rms-phase}}$	rms phase voltage
l_s	stator stack length
d	air gap diameter
$\hat{B}$	peak fundamental flux density
J_e	specific electric loading
B_m	specific magnetic loading
S_a	apparent power
N_{ss}	synchronous speeds
N_{slot}	total number of turns per slot
AGC	Air gap circumference
W_T	tooth width
W_s	slot width
d_s	Slot depth
B_{rms}	Rms fundamental airgap flux density
I_{ph}	Rated rms phase current
Q_d	Reactive power at d axis position
Q_q	Reactive power at q axis position
α_1	Angle between rotor flux axis and reference
M^+	Forward rotating mmf wave
M^-	Backward rotating mmf
n_y	Electrical displacement factor
n_C	Number of coils
τ_{cc}	Coil span of c^{th} coil
τ_p	Pole pitch
$\hat{I}$	Peak value of phase current
θ_c	Current angle
γ	Peripheral distance

Chapter 1

Introduction

Performance of an electric machine depends on the physical design and component material properties. In general, when considering application in electric vehicle drive trains, machines should have desirable characteristics include [1-3] high power and high power density, high efficiency over wide speed and torque ranges, high torque at low speeds for starting and climbing, high fault tolerant capability, very wide speed range including constant-torque and constant-power regions and small physical space. Higher efficiency electrical drives are desirable to minimize battery size and energy use. These characteristics, together with development of high performance magnetic material have led to wide scale use of PMSM in automotive application. In a PMSM, rotor side flux is produced by the permanent magnet on the rotor instead of rotor winding or bar which results of higher flux density and lower rotor loss than other motors. In an IPMSM, the permanent magnets are inserted inside the rotor. Thus, there is low possibility of braking or demagnetizing the magnets during the high-speed operation of the machine. The IPMSM has also a saliency ratio which offers useful reluctance torque. The availability of reluctance torque enables flux-weakening control for wide speed range and constant power operation to be utilized in IPMSM. Moreover, the eddy current loss on the surface of the rotor of IPMSM can be greatly reduced. The fractional slot IPMSM has many degrees of freedom in the design of mechanical structure by changing slot and pole combinations. The magnetic geometry in the rotor could provide the feasibility of saliency ratio optimisation. However, IPMSM has some drawbacks such as high harmonic content in the air-gap MMF distribution [4], which results in higher eddy current losses in the high speed region. However, the accurate calculation and prediction of eddy current loss as well as core loss are difficult especially at high frequency

harmonic field. An IPMSM can be seen as a good option as an EV drivetrain component. However, one final critical requirement for EV components is consistent performance. The performance is dependent on material properties, which are influenced by manufacturing processes. For this reason it is important to understand how certain manufacturing processes impact magnetic performance and losses.

1.1 The Need for Core Loss Estimation

Though, modern electrical machines are capable of high efficiency, the core loss of a machine gives a significant amount of power loss. For example, the estimated annual magnetic core losses in the United States is still as high as 45 billion kWh costing about 3 billion dollars per year[5]. Variable speed drive is employed for motor speed control in industry application in order to improve process control and energy saving. However, employing of variable speed drive also increase the core loss and temperatures of the machine. Core loss of a machine depends on some electrical parameters, magnetic properties and physical properties such as frequency of the flux, flux waveform, flux densities, temperature, etc. These dependencies are nonlinear rather than straight forward, hence difficult to predict. However, the core loss calculation error might be the cause of serious faults. During the machine design stage, accurate quantification of core losses is a challenge to improve the machine efficiency and compute the actual machine efficiency. Even a small improvement in electrical steel quality reflects into significant economical and environmental benefits.

1.2 Why magnetic test is required for machine core materials

Design of a machine for this type of application requires simulation of a number of operating points. Typical simulations will provide precise results for the predicted performance of the machine at each operating condition. As with all electrical machines, the accurate prediction and optimization of permanent magnet motor characteristics

require accurate knowledge of core material properties [6-9].

The specification of the steel differs between steel manufacturer's data and the final steel in the manufactured motor. Magnetic properties of the core material depend on (among others) the chemical properties of the steel, grain size, texture, stress, etc. The majority of these factors are influenced by the various manufacturing stages prior to delivery. These stages include punching, welding, handling heat treatments and stress relief annealing [6, 8, 9].

Small variations in the input magnetic characteristics may result in significant variation in the final performance of the machine. The characteristics data of the lamination steel may vary between manufacturers due to metallurgical factors which depend on the manufacturers thermo-mechanical processing sequence [9].

1.3 Main contributions of the thesis

There are two main contributions in this thesis. The first one is the investigation of the influence of manufacturing process on electrical steels magnetic properties in order to predict IPMSM performance. Hence, several sets of steel characteristics are used to compare the performance. This includes manufacturer's provided data, other sets of data obtained from Epstein frame tests. The tested samples are JFE 35JN250 SRA, non-SRA, different heat treated Epstein steel samples, AK steel 29 gauge M-19 SRA and non-SRA samples. The concentrated winding IPMSM is studied using time-stepped FEA to obtain both input-output characteristics and core losses for different steel types.

The second contribution is to validate the physical core loss with the core loss obtained from FEA. In that section AK steel 29 gauge M-19 with SRA and non SRA are selected for building two machines that are nominally identical concentrated winding PMSMs except for the SRA process. A DSP motor controller is used to drive these IPMSMs at different speeds in order to validate the core loss at loaded and open circuit

conditions. This also identifies the better motor performance based on core loss and efficiency. The variation in motor losses between the two motors compared to the ratio of core losses from the Epstein tests.

Chapter 2

Core Loss

One of the most important parameters of electrical steel, used as a core material of the electrical machines, is Loss. Laminated steel sheets are used in construction of machine core to reduce the eddy current loss which is one of the main parts of core loss. Moreover, the quality of steel scaled in grades and thereby the prices strongly depend on loss incurred. Core losses of an electrical machine is higher for high speed machine, even at 50/60Hz machine operating frequency this loss takes a considerable fraction of the total losses ranging from 15% to 25% [10]. The choice of steel grade and lamination thickness can greatly increase the efficiency of the machine.

2.1 Magnetic properties of material effects on core loss

The core loss of the electrical steel varies with the different magnetic properties of the magnetic materials. Magnetic materials can be defined as the materials that can magnetize themselves and also can be attracted or repelled by a magnet. The local magnetization condition depends on many factors such as grain size, local stress, grain structure, presence of impurities, and the balance of local energy. However, the process of magnetization represented by the hysteresis loops and the magnetization curves is influenced significantly by the presence of magnetic domains and domains' walls.

Magnetic domains: Magnetic material is spontaneously divided into many small regions of the same direction of magnetization called domains. Domains ensure the minimum free energy at the magnetized state of the magnetic materials. Whereas, in demagnetized state, these domains are distributed in such way so that the net magnetization is zero. However, the domain structure can be very complex in real magnetic materials due to the influence of impurities, mechanical defects, grain boundaries, etc.

Domain walls (DWs): The wall which separates any domains of opposite direction of magnetization in a magnetic structure is called domain walls. The local magnetisation direction can be changed gradually over certain distance between two domains. The typical domain wall (normally thinner than 10 μm with small volume) in which the elementary magnetic dipoles can reverse their alignment.

Magnetic flux density B and Magnetic field intensity H are two basic magnetic parameters. Other parameters, such as permeability, magnetisation curve, polarization and magnetization are supported by those two values.

Magnetic flux density (B): Magnetic flux density, also called magnetic induction, is the amount of magnetic flux through a per unit area that is perpendicular to the direction of flux (Φ).

$$B = \frac{\emptyset}{A} \tag{1}$$

Magnetic field strength (H): Magnetic field strength, also called magnetic field intensity, is a measure of direction and intensity of a magnetic field. It can be expressed by the following equation

$$H = \oint_c Ni.dl \tag{2}$$

The relationship between *B* and *H* can be represented by a magnetisation curve. The magnetization curves of magnetic materials depend on various factors such as physical properties of the materials, the sequence of passage through various magnetic states, the external conditions of the materials, etc. The magnetization curve can be classified into several categories such as a) initial magnetization curve b) static hysteresis loops c) nominal magnetization or commutation curves. In initial magnetization curve, H increases monotonically from the fully demagnetized state of the materials. In static hysteresis loop, B which is the function of *H* is found after continual tracing with a

certain range of forward and reverse directions *H* values. The nominal magnetization curve represents the loci of the symmetric loop's tip with magnetic reversal. The nominal magnetization curve representation could be single line or loops, depending on the excitation frequency. An initial magnetization curve contains fundamental information of a magnetic material. This curve can be divided into several regions.

The closest domains to the direction of the applied field start to rise into other domain with the increase of magnetic field. This region is reversible because domains restore to its initial demagnetized state upon withdrawal of applied magnetic field. The next region is the part where permeability is the maximum. In this region, as the domain walls movement are irreversible, the hysteresis loop will appear if the magnetic field is reduced. In next region the domain wall movement disappears and magnetisation direction tends to the magnetic field direction. Next step of the magnetization curve is called saturation where there is no change of the polarization with the increase of *H* and the magnetization direction is same as field direction.

When an alternating magnetic field is applied in a magnetic material and completes a cycle, its magnetization will follow a loop called a hysteresis loop. It is frequently mentioned to as the B-H loop. However, the hysteresis is related to state of magnetic domains in the material. Once the magnetic domains are made a change in direction, the energy is transformed to heat and sound because of the magnetic hysteresis of the material. Figure 2.1 shows a typical hysteresis loop and its different characteristic points. The curve from center to point 'a' is called initial magnetization curve. Point 'a' in Figure 2.1 is the saturation point where almost all the magnetic domains are aligned in one direction. Point 'b' represents residual flux density when the magnetizing force is removed after attaining saturation. This residual flux density is called retentivity. However, retentivity and residual magnetism are not the same when the material has not been

magnetized to the saturation point. Point 'c' represents the required reverse magnetic field to make the magnetic flux return to zero. This required reverse magnetic field is called coercive force. Point 'd' represents the opposite saturation and 'e' and 'f' represent the opposite flux density of retentivity and opposite magnetizing force of coercive force respectively. A minor hysteresis loop may exist in main hysteresis loop because the flux reversal, which might be the cause for harmonic flux magnitude and phase. Any closed BH curve apart from the fully saturated one is called minor loop[11]. Symmetrical and asymmetrical minor loop could be originated inside the main hysteresis loop described in [12, 13].

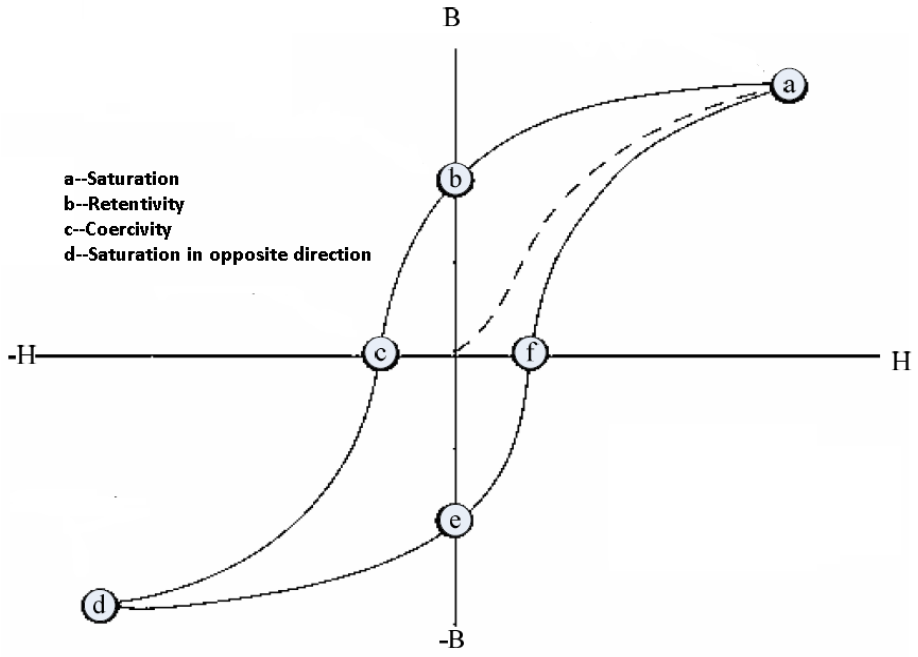

Figure 2.1 Typical hysteresis loop and its characteristic points

The area under BH loop differs depending on frequency, flux density and material properties. The overall energy per cycle and core loss per unit volume of the material can be calculated from the BH loop using the equations (3) and (4) respectively[14].

$$E_{loop} = \oint H \, dB \tag{3}$$

$$W = f \oint H \, dB \tag{4}$$

From the equations (3) and (4) it can be concluded that the core material having narrower hysteresis loop gives the lower core loss compared with core material with wider hysteresis loop. Dlala et al. [15] presented a core loss model for laminated magnetic core where the author considered magnetisation curve and the B-H loop shapes omitting numerical nonlinear equation while maintaining the core losses accuracy. However, the core losses of the same electrical machine are different based on the loaded and unloaded conditions. Moreover, when the machine rotates at the synchronous speed, the flux variation in the rotor is very little which directs the smaller core loss in the rotor than that of the stator. Thus, stator part core losses make a significant effect on the machine efficiency especially at high speed region.

2.2 Core loss Separation

The hysteresis loop energy loss represents the total core loss per cycle which include two components; eddy current loss and hysteresis loss. Moreover, total core loss can be presented by a core loss plot where core loss per cycle vs. frequency is being extrapolated. Ibrahim et al. [10] explained the core loss separation process considering the skin effect at high frequency region. At low frequency the skin effect is negligible and constant hysteresis energy loss per cycle can be assumed. At high frequency, the hysteresis loss is calculated based on the non-uniform flux distribution inside the lamination as the flux density is not same all over the cross section of lamination. The static hysteresis loss per cycle can be found estimating power loss at zero frequency. Total hysteresis loss is the multiple of static hysteresis loss per cycle and the operating frequency provided that the hysteresis loss per cycle is independent of frequency. Figure 2.2 shows the eddy current and hysteresis loss separation method. This loss separation

process is acceptable only when the frequency level is low and the magnetic field across the laminated core material is uniform. If the eddy current is produced inside the core due to the exposure of laminated core to a time-varying magnetic field, an induced secondary magnetic field opposes the applied field in agreement with the Lenz's law. The magnetic field due to eddy current is maximum and minimum at the centre and surface of the lamination respectively. The resultant magnetic field is the sum of applied field and the generated field due to eddy current. The maximum resultant field exists at the surface, whereas the minimum one exists at the center of lamination. This phenomenon is called skin effect which Influences on current distortion and increases the loss in machine [16]. Though the skin effect can be neglected at low frequency due to small eddy current, it is significant at high frequencies. Hence, the extrapolation method for separating the core loss is only valid at low frequency level where the hysteresis energy loss per cycle could be assumed constant. Other precise core loss separation methods considering skin effect [17-20] are required at high frequency region in order to separate the core loss components.

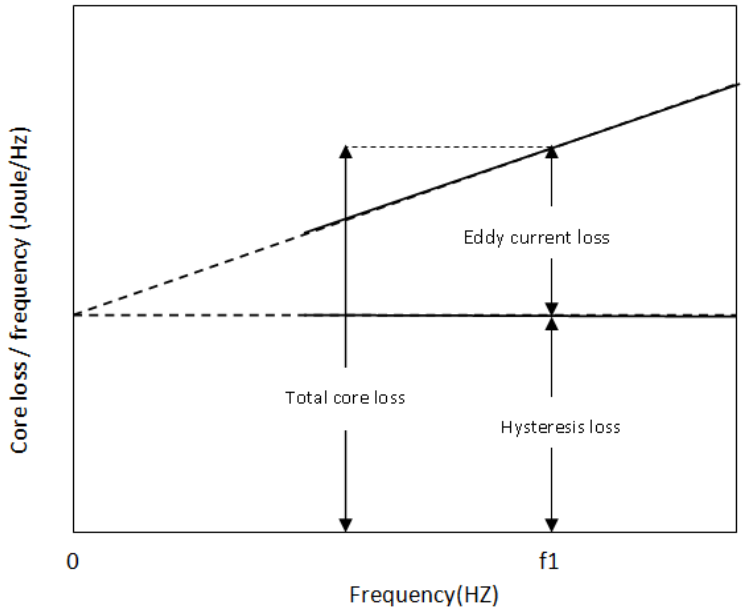

Figure 2.2 Separation of core loss by extrapolation method

2.3 Core loss calculation

2.3.1 Analytical Iron loss calculation

A number of analytical formulas exist in the literature for calculating the machine core loss. The iron losses are a summation of hysteresis, classical eddy-current and excess loss, which can be expressed as follows [21]:

$$W = K_h f B^{\alpha} + K_e f^2 B^2 + K_a f^{1.5} B^{1.5} \quad (5)$$

Equation (5) is called Bertotti's iron loss model. The first and second right-hand terms represent hysteresis loss and eddy-current loss components respectively. The last term represent the excess or anomalous loss component, which can be attributed to intricate phenomena, such as magnetic anisotropy, micro-structural interactions, non-homogeneous locally induced eddy current [21].

Moreover, two-term approach, which is another form of equation (5), can be used to calculate the total core loss as described in (6) [22].

$$W = K_h B^{\alpha} f^{\beta} + K_e B^{\gamma} f^{\delta} \quad (6)$$

All the coefficients in equation (6) are assumed to be constant and are determined from the measured data for a certain frequency using the least square method. Equation (5) or (6) is true only for sinusoidally varying flux density. Hysteresis loss equation, which is based on peak value of flux density, is true if there is no minor hysteresis loop. Moreover, the above expression with constant coefficients can lead to unpredictable and significant numerical errors, hence flux density and frequency dependent coefficients are needed. However, some modified analytical core loss methods can be used to get more accurate core losses.

Modified analytical calculation method: The modified iron loss can be expressed by the following equations where the coefficients vary with the flux density and frequency [6].

$$P_{Fe} = P_h + P_e \tag{7}$$

$$P_h = K_h(f, B) \cdot fB^2 \tag{8}$$

$$P_e = K_e(f, B) \cdot (fB)^2 \tag{9}$$

Eddy current loss co-efficient K_e decreases with the frequency and increases with the flux density. Whereas, hysteresis co-efficient K_h increases with the frequency and decreases with the flux density. But within a given frequency range**,** K_e and K_h depend only on flux density and then K_e and K_h can be represented by using polynomial functions as shown below

$$K_e(B) = K_{e3}B^3 + K_{e2}B^2 + K_{e1}B + K_{e0} \tag{10}$$

$$K_h(B) = K_{h3}B^3 + K_{h2}B^2 + K_{h1}B + K_{h0} \tag{11}$$

It is noted here, use of higher polynomial might be an effective solution to reduce the higher relative error in low flux density. To compute the polynomials coefficients of the hysteresis and eddy current losses, experimentally determined values are required where the following equations (12) and (13) are used. To measure the co-efficient, at least four readings should be taken using four different flux density levels.

$$K_h = \frac{\pi}{\rho v} \cdot \frac{H_{irr}}{\hat{B}} \tag{12}$$

$$K_e = \frac{1}{f^2\hat{B}^2}\left(P_{Fe} - f\hat{B}\frac{\pi H_{irr}}{\rho v}\right) \tag{13}$$

The advantages of this model are simplicity, minimum requirements in terms of experimental parameters**,** and relatively high estimation precision at low fundamental and switching frequencies. However, at high fundamental and switching frequencies the error is relatively high. Another drawback is that the experimental work has to be done to calculate the iron loss numerically. Nevertheless, this model is particularly useful when designing a preliminary electrical machine and analyzing the possible power.

Sinusoidal and non-sinusoidal supply voltages can be fed in the machine. The non-sinusoidal waveform of the supply voltage increases the losses in the core materials. Several core loss models have been developed considering different supply voltages which come from inverter or chopper described in various literatures [23-26]. These models include laborious mathematical models of the minor hysteresis loops [21]. The output voltage of the inverter is controlled by the static switch like thyristors or power transistors. Thus the output current of the inverter which is the input of the machine, contains high-frequency harmonics, which lead to the increase of the total losses in the machine. These increased losses are due to the additional hysteresis losses caused by the distorted waveforms of flux density, increase of eddy-currents induced into machine core, and the skin effect in the armature windings. The operating point of the motor affects these additional losses since these losses are influenced by the magnetic saturation of the core and the magnitude of the armature current. The eddy current loss in the rotor, which is the part of excess eddy current loss due to the inverter supply, is more significant than that in the stator. More so, the rotor supplemental loss is increased with the loading of the machine, whereas the stator supplemental loss remains constant with the loading of the machine [27]. IPMSM having the rare-earth magnets in the rotor may have relatively large harmonic eddy-current losses due to the carrier harmonics produced by the PWM inverter; because the conductivity of the magnet and the carrier frequency are large [28]. Therefore, it is a challenging task to estimate the core loss correctly under the above condition. Though some physical models [29-31] and engineering approaches [32-35] are proposed to estimate the core loss correctly, a decisive ending has not been reached yet. An effective approach for measuring the variation of core losses with known voltage characteristics was suggested in the works of Boglietti et al. [36, 37]. The peak value of flux density is proportional to the average of rectified supply voltage provided that the minor loops are ignored. As a result, the hysteresis-loss component varies with the

average value of the rectified supply voltage. However, the eddy current loss component is dependent upon variation of flux density. This eddy current corresponds to rms value of supply voltage. The following equations represent the iron losses with an arbitrary voltage waveform.

$$W = \eta^2 w_h + x^2 w_e \tag{14}$$

$$\eta = \frac{v_{avg}}{v_{1,avg}} \tag{15}$$

$$\chi = \frac{v_{rms}}{v_{1,rms}} \tag{16}$$

Iron loss can be calculated in the frequency domain or in the time domain. The loss separation process which is used among the hysteresis, eddy current and excess loss, is in the frequency domain. The initial phases of each individual deformed flux harmonic are not considered when the iron loss is calculated in the frequency domain. Though the initial phase is not significant for higher order harmonics, the initial phase is very meaningful due to the change of peak flux as well as hysteresis iron loss in case of lower order harmonics with relatively higher amplitude. In that sense, the iron loss should be calculated in the time domain. However, many experiments should be done in order to identify indispensable parameters to get the correct results of iron losses. No compensation of the aforementioned requirements leads to incorrect results of iron loss[7].

2.3.2 Finite Element Method for Iron loss calculation

Finite Element Method (FEM) is more reliable and cost effective compared with analytical method described above to calculate the core losses. There are four categories in FEM which are used to calculate the core losses[38]. These approaches are described below.

First FEA approach

Iron losses are calculated based on flux density waveform which is predicted at the end of FEA analysis, whereas eddy current is neglected during 2D FEA simulation. This traditional FEA approach is appropriate when the electrical machine is excited with a single frequency. However, this approach may give error estimation of iron loss when PWM supplies are used. Nonetheless, by the help of Crank-Nicholson approach and bulk field equation, the time stepped FEA values can be modified which incorporate the eddy current effect[38].

Second FEA approach

This approach uses 3D FEA model in which the eddy current is allowed to flow through the laminations in three dimensions. In this model, the 3-D nonlinear time-stepping eddy-current analysis is used to calculate the electric and magnetic fields in the electrical steel sheet. In this model to calculate the iron losses, the eddy-current and hysteresis losses are calculated by considering the skin effect; the excess loss is also included in the eddy current loss [39]. This method is especially suitable for the estimation of the higher-order harmonic iron losses. Though the time stepped 3D models are highly accurate, higher computational time is required.

Third FEA approach

The third FEA approach is a 2D FEA in which the eddy current effects are considered and are used to estimate the hysteresis loss of the steel lamination. One assumption in this iron loss estimation process is that the iron loss of the rotating field machine is the sum of the iron losses in radial and tangential directions under alternating conditions [7]. In hysteresis loss equation, minor hysteresis loop is not considered. However, the static hysteresis loss in this process for both axial and rotational magnetization can be estimated

by the help of static Jiles–Atherton model. The modified process offers some advantages such as, initial phases of harmonics and the static hysteresis loss estimation in case of rotational magnetization, are included in this process. Moreover, the influence of fundamental harmonic on the static hysteresis losses is also taken into consideration. The disadvantage of this process is the high error of core loss estimation.

Fourth FEA approach

This approach is 1D FEA coupled with 2D FEA to do the modeling of the eddy currents in 2-D analysis. Backward Euler and FEM are implemented in order to discretize the coupled problem and Newton-Raphson technique is used to deal with the nonlinearities of both 1-D and 2-D equations. The success of the coupling of the eddy-current modeling to the 2-D field analysis depends on some factors such as power balance of the method, magnitude of the magnetic field strength at the boundaries of the sheets. Among all the factors, the main indicator of success of the coupling is power balance. However, computational time is also a great interest in this method [40].

The core loss estimation accuracy is greatly improved when the conventional approach is combined with the higher order 1-D elements. With the second and third-order elements, the error in the power balance is below 1% [40]. The computational time of this approach is higher than 2D FEA but lower than 3D FEA approach. This approach has higher accuracy compared with traditional 2D FEA but it has lower accuracy compared with 3D FEA.

The iron loss due to the fundamental harmonics of the total flux linkage in the laminations can be represented by core loss resistor in the IPMSM equivalent model. Lar et al. [41] represented a core loss resistor in an IPMSM model as a function of *d*-*q*-axes currents at fixed values of rotor speed and load torque. Huang et al. [18] discussed the difficulty to predict the core loss of a PM machine regarding diverse structure, flux

distribution, and rotational variation of flux. The authors presented a core loss model for PM motor which is based on flux variation locus and FEM. The experimental core loss result is somewhat close to the predicted core loss getting from the prescribed model, without use any correction factor. Zhang et al. [42] proposed dynamic hysteresis core loss model which can calculate the core loss at different frequency and different thickness of the materials without a huge experimental database of core losses. The author claimed that the model can predict the core losses distinctively using one set of experimental data at one single low frequency in a thin lamination. Rasilo et al. [43] investigated the effect of thickness of laminated core material used in the rotor on the total core losses of the synchronous machine. The authors found that the thinner laminated core machine gives the significant higher core losses above the rated voltage under no load condition while the thicker laminated machines gives the significant higher core losses on load condition.

2.4 Harmonic core losses of rotor and stator

Electric motor magnetic loading is changed with loading conditions which is referred to field weakening current in constant power region. The specific magnetic loading depicts whether the magnet circuit part is saturated during the machine operation. The air gap flux density is distorted due to armature reaction. The armature reaction established under loaded condition affects the core loss. The core loss could be reduced by reducing the permanent magnet flux, at the high speed region. In IPMSM, the air-gap is small and the armature reaction can cause undesirable saturation. The ‘saturation effect’ might increase the core losses.

It is important to investigate the harmonics of the MMF distribution to get the knowledge about the core losses. Each coil of a fractional winding machine produces harmonics, whose amplitude varies considering the coil throw. The star of slots can be used to represent the harmonics of the armature MMF distribution [4]. Each coil can be

matched to the symbolic phasor when one harmonic order is considered at a time. Thus, the total harmonic contents of the MMF distribution can be calculated by doing the geometric sum of the phasors.

The motor core losses could be divided into two parts: stator core loss and rotor core loss. Core loss increases at high speed region mainly due to harmonics in the air-gap flux density [39, 44]. However, significant harmonic core losses are not same for rotor and stator. The space harmonics which is produced due to the coil discrete position within the slot, is liable to produce the harmonic components of core losses.

The main mmf harmonics order called fundamental harmonics depends on the pole pair and it is equal to the number of pole pair which is synchronous with respect to the rotor. However, MMF harmonics which are asynchronous with rotor causing current in the rotor, hence induce eddy current loss in the rotor. Higher order and lower order harmonics than the main harmonics which is called sub harmonics exist in the fractional slot machine. The sub-harmonics mmf lines go into the rotor deeply than the main harmonics due to higher sub-harmonics wavelength[45]. In order to produce continuous torque, only the fundamental harmonics interact with the magnetic field of the rotor. The other noticeable mmf harmonics may be the cause of vibration, noise, eddy current loss in magnet and saturation of motor core[46].

Chapter 3

Concentrated winding IPM

Ac machine winding are classified as distributed and concentrated. The value of slot/pole/phase is (q) > 1 in case of distributed winding and q≤1 in case of concentrated winding. Distributed winding can be classifies short pitched or full pitched winding. A short pitch distributed winding reduces the harmonics contain in emf, torque ripple and cogging torque by selecting proper slot pole combination compared with full-pitched distributed winding. However, the distributed winding arrangement has the higher end winding, results higher joule loss compared with concentrated winding. The winding factor of distributed winding is higher than concentrated winding. There are two types of possible concentrated winding arrangements: fractional slot and integral slot. Scientific comparative studies between these two arrangements of concentrated winding are presented in [47]. In concentrated winding, if the value of q is less than one called a fractional slot winding and q=n with n an integer is called an integer slot winding. However, the overlapping winding pattern is used in distributed and integer slot concentrated winding machine[48]. In FSCW the winding pattern is non-overlapping. Non-overlapping coil offer some advantages over overlapping windings such as, shorter end winding, simplified winding insulation, reduced number of coils.

There are different nomenclature used for non-overlapping concentrated windings[49]. The most commonly used terminologies are concentrated windings; concentrated fractional pitch windings; coil space factor, fractional slot wound; fractional slot. There are two types of non overlapping winding layout used frequently in concentrated winding: Non-overlapping single layer; Non-overlapping double layer. Figure 3.1 shows the schematic view of non-overlapping single and double layer windings.

Non-overlapping single layer winding: The winding coil wound around every second tooth of the stator core. Hence, pattern the number of coil is half of the slot number. There is a flexibility to vary the coil pitch in order to improve the machine performance. For the reduction of cogging torque variable slot pitch can be used instead of skewing of the rotor.

Non-overlapping double layer winding: The winding coil wound around each teeth of the stator core. Hence, the number of coil is equal to the number of slots. As the coil pitch is fixed, skewing of the rotor is needed in order to reduce the cogging torque. Moreover, double-layer concentrated winding has poorer thermal performance compared to the single-layer concentrated winding due to additional insulation layer placed in the slot between the phases [50]. There are two types of non-overlapping double layer concentrated winding commonly used in motor design. One of them is vertical winding and the second one is horizontal winding shown in Figure 3.2 Double-layer concentrated-windings (a) Vertical (b) Horizontal. However, the fault current vary depending on shorted turns due to their variable leakage inductances in case of horizontal windings[51]. Vertical winding is better in term of variability of fault current level.

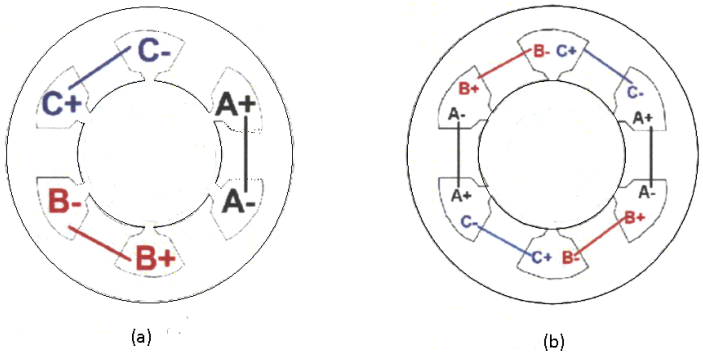

Figure 3.1 Fractional slot concentrated stator windings: (a) single-layer and (b) double-layer

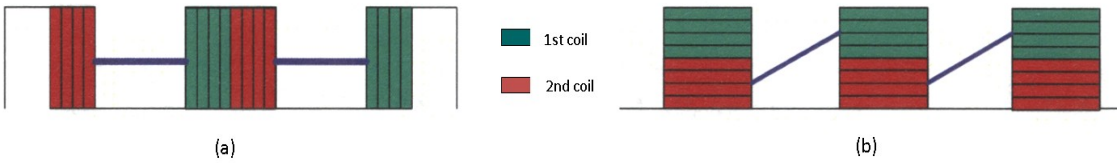

Figure 3.2 Double-layer concentrated-windings (a) Vertical (b) Horizontal

The total loss decreases and the efficiency is improved by using fractional slot concentrated winding; but the efficiency of concentrated winding IPMSM might become worse in high speed regions, in which the core loss is more predominant than the copper loss [52]. Though fractional-slot winding with non-overlapped coils is an interesting solution for fault-tolerant applications due to its high leakage inductance and low mutual coupling among the phases, the fractional-slot configurations exhibit a high harmonic content in the air-gap MMF distribution [53]. The resulting harmonics of in the magnetic flux distribution may result in excessive iron losses during high speed operation, whilst parasitic effects such as vibration and audible noise may also be concerns.

Though the no-load losses are same for both fractional slot and integer slot concentrated machine, higher stator and wedge losses take place in integer slot and higher rotor and PM losses take place in fractional slot machine. The increased loss in fractional winding concentrated machine is mainly due to the induced losses which are generated by harmonic located in the rotor and magnets. The harmonics of the MMF distribution affect the core losses. The star of slots can be used to represent the harmonics of the armature MMF distribution[53]. Each coil of a fractional winding machine which produces harmonics can be matched to the symbolic phasor when one harmonic order is considered at a time. Thus, the total harmonic contents of the MMF distribution can be calculated by doing the geometric sum of the phasors.

Up to 21st century, concentrated winding in permanent magnet machine documented as increased EMF harmonics, limited to lower number of phases, lower power application, lower torque density and narrower constant power speed range [54, 55]. During the first decade of 21st century, development of multi phase of concentrated winding is described in [51, 56-60]. Chong et al. [61] and El-Refaie et al. [62-64] achieved a wide constant power speed range of an concentrated winding PMSM. Many papers [65-68] show that fractional slot concentrated winding machines can offer some significant advantages compared to distributed winding machines.

One of the main features of concentrated winding is low copper loss due to the shorter end winding length which is the result of non-overlapping coil in concentrated winding. Moreover, shorter end winding leads to reduce the axial length of the machine. The manufacturing process of concentrated winding is easier than the distributed winding because of its independent winding structure and wrapped around the separated teeth core. It offers an increased slot fill factor, as the stator winding process is easier which allow the pre- wound stator windings. Moreover, non-overlapping concentrated winding demonstrates higher tolerance to phase to phase fault due to effective phase separation. Murakami et al.[69] and Rahman et al. [70] taken up the advantages of concentrated winding non-overlapping coils in wide speed machines with increased efficiency. A higher slot fill factor reflects less copper loss. Jack et al. [71] investigated on permanent magnet machines with segmented stator structure and pre-pressed concentrated windings. He achieved 78% fill factors and increase torque density. And hence; the efficiency is increased of the machine. However, a high value of fill factor is an obstruction for keeping sufficient mounting clearance inside the stator slot. De Donato et al. [72] presented a design where 77% fill factor was achieved and stated that the stator core wound coils is the suitable solution to overcome the clearance obstruction of getting

higher fill factor. Constructing individual stator teeth and assembling the stator core after winding the coil around the teeth can also improve the fill factor. But mechanical problems might be an issue when assembling all the teeth together with the stator yoke.

Increasing the number of winding layers can effectively reduce the mmf harmonics [73]. Alberti et al. [74] presented an effective theory and design work for fractional slot multi layer and multi phase winding. Different q values affect the performance characteristics of the machine such as cogging torque, torque ripple, iron loss and copper losses [75]. When the least common multiple between slot numbers and pole numbers is large, the cogging torque will be reduced due to increase of the cogging torque frequency[65]. The pole numbers are an important factor to reduce the size of the rotor, which reduce the volume of the machine with a given power[76]. Moreover, the higher number of poles reduce the required stator yoke, thus the power density is increased. However, proper selection of q gives the higher winding factor which causes a lower current for the same torque due to high effective number of turns[64]. The fractional winding design follow the rule mentioned below [66]:

a) q value can be represented by the term b and c, $q=b/c$ where b and c are integer number.

b) b indicate the total number of 1s , whereas $(b-c)=r$ represents the total number of zeros

c) "1" and "0" are distributed such a way that "1" being allocated in the sequence as at evenly-spaced intervals as possible.

d) The sequence is repeated $3p/c=Qs/b$ where Qs represents total slot number and p represents pole number.

e) In the sequence "1" represents one layer of the concentrated winding and the other layer can be found by filling the return conductor of the adjacent tooth coil.

f) The usual phase sequence AC'BA'CB' or AB'CA'BC' can be used to represent the sequence, where A' is the return conductor of A, B' is the return conductor of B and so on.

Winding factor

Winding factor is defined as the ratio of the flux accepted by each turn and the flux produced by the excitation MMF [66]. Its value is less or equal to unity. The maximum winding factor can be achieved when the value of SPP is unity, which is possible for the case of distributed winding or integer slot concentrated winding. The winding factor is proportional to the torque, so, the machine having lower winding factor requires either higher number of turns or higher current to compensate the lower torque[76]. Moreover, lower winding factor leads to an increase in the resistive losses. A winding factor can be calculated on the basis of the winding layout as in [65, 77] or without any knowledge of the winding layout [78]. However, the fundamental winding factor based on winding layout can be calculated using the following formula [77].

$$K_{w1} = \frac{\sum_{i=1}^{2Q/3} E_i}{\frac{n_l Q}{3}} \tag{17}$$

and Emf phasor

$$\overline{E_\iota} = Sign(S_i) e^{j\frac{\pi P |S(i)|}{Q}} \tag{18}$$

Inductances of the windings plays an important role for establishing the machine performance such as flux-weakening capability, the reluctance torque, the eventual fault current and the current ripple. El-Refaie et al. [79] investigated the various component of the inductances in different slot pole combination of machines in which all the teeth are wound and those in which only alternate teeth are wound. The affect of key design parameter such as slot opening geometry, the magnet remanence, the effective air gap length and the winding disposition on the inductances of the machine are investigated in

that paper. The alternate wound teeth have a higher slot leakage inductance compared with all wound teeth machine. Moreover, the higher the slot/pole number ratio for a given back emf gives the lower winding inductance as the number of turns per phase is lower to maintain the back emf. However, the inductances can be represented in term of *d* and *q* axis inductance values. Flux weakening capability depends on two main characteristics which are saliency ratio and characteristics current. Saliency ratio depends on the ratio of L_d and L_q where as characteristics current depends on the magnet flux linkage and the L_d values. Though, the surface mountain permanent magnet machine gives the same L_d and L_q inductances, the interior permanent magnet machines do not offer same L_d and L_q inductances. Chong et al. [80] and Soon et al. [81] compared the L_d and L_q inductances for concentrated and distributed windings IPM machine. The author conclude from the simulation result that the concentrated winding gives the higer L_d and L_q values compared to distributed winding but the saliency ratio becomes low due to the lower increase rate on L_q inductance in case of the concentrated winding. This leads to reduce the reluctance torque. Magnetic torque is also decreased due to the low winding factor. Results; lower torque per amp is achieved. So, in constant torque region, higher current is required for concentrated winding machine than distributed winding machine. But in constant torque region, increased d axis inductance and lower back emf lead to decrease the required current in concentrated winding machine. However, concentrated winding gives the higher value of self inductance and lower value of mutual inductances which has a great impact in fault tolerance.

Noise and vibration is higher in concentrated winding than a distributed winding machine. Though the source of the vibration of the permanent magnet machines are torque ripple, cogging torque and radial magnetic stress, radial magnetic stress are considered as the main causes of vibration [82]. Radial stress of a concentrated winding

is as large as it might deform the stator core. Asano et al. [83] described the noise improvement technique for concentrated winding PMSM. When the distribution of the magnetic force on the stator is not symmetrical, a resultant force takes place which produce a noise. If the radial forces on the stator compensate each other the vibration and noise will be eliminated. This can be done by choosing proper slot and pole combination explained in [77]. The stator and rotor slot should not be very close in order to reduce the torque ripple , whereas stator and rotor slot should not be too far in order to reduce the core losses [84]. Hence there is a trade-off between torque ripple and core losses depending on selection of stator slot and rotor pole. When the radial force of a concentrated winding machine is large in the air gap, the enlarged air gap could make a smooth radial stress in the airgap which reduces the vibration of the motor. Moreover, the radial force can be reduced by making some hole inside the rotor; Result reduce the vibration without decreasing efficiency [52].

Concentrated winding has high reliability applications due to its fault tolerance capability. In concentrated winding configuration, the phase windings are separated physically, result; it gives higher self inductances and smaller mutual inductances between phases compared with distributed windings. The higher phase inductance limits the short circuit current and lower mutual inductance between phases prevent healthy phases prolong the fault. . Bianchi et al. [53] investigated fractional slot concentrated winding fault tolerance capability where they showed that single-layer windings were more fault tolerant and appropriate for larger air-gap machines. Shah et al. [51] analyzed turn-to-turn fault by means of double layer vertical concentrated winding and double layer horizontal concentrated winding and concluded that a double layer winding performance was same as a single layer winding in terms of fault avoidance. Arumugam et al. [85] also presented horizontally and vertically placed conductors in the stator slot

for fault-tolerant of permanent magnet machines. The vertical winding configuration give a better short circuit fault tolerance compared with horizontal winding concentrated winding as the current variation with the faulty turn position is small in vertical winding. Abolhassani and Toliyal [86] introduced fault tolerant five-phase concentrated winding IPM motor drive for electric vehicles and showed that the performance decrease a little under single phase and switch faults.

Many researchers were interested in the application of concentrated winding to machines used for field weakening applications since use of concentrated winding increases inductance values which facilitates in gaining optimal filed-weakening conditions. El-Refaie and Jahns [87] presented a detailed comparison between IPM and SPM machines with different winding configuration. SPM machines with fractional-slot concentrated winding minimize machine volume and mass since their short winding end turns and techniques for achieving high slot fill factors via stator pole segmentation. Later they extended their work [88] and exploit the field-weakening potential of concentrated winding and carried out details study in this area of application. Deak et al. [89] presented an extended field weakening and overloading test for two high-torque density PM motors: one with double layer concentrated winding containing semi-closed slots and the second one having single layer concentrated winding with open slots and unequal tooth-widths. Their result confirmed that the field weakening can be extended up to 5 times the rated speed with constant output power of 45 kW. Soong et al. [90] described the machine design parameter plane using the characteristics current and the peak back-emf to narrow down the design region. They used parameter plane to study freedom car traction motor drive requirements and the characteristics of five fractional slot concentrated winding SPM machine designs as a practical application. Munoz et al. [91] compared a SPM and IPM machine for both concentrated and distributed windings

provided the same stator outer diameter, equal air-gap length, stack length, magnet volume and peak current. The author concluded that though the concentrated winding machine gives a shorter end-winding which leads to increase the effective stack length and hence compensated the lower winding factor and torque per amp, the machine weight is increased due to the increased stack length which limits the relative advantages of using concentrated windings. They also concluded that the field weakening ability is limited since concentrated winding reduces the saliency ratio.

Though the concentrated winding optimal field-weakening capability, concentrated winding introduces additional harmonics which increases core and magnet losses especially higher frequencies. To reduce these additional losses extensive research has been done. Mellor et al. [92] presented a computationally efficient iron loss model for brushless AC machines which can cater for both rated flux and field weakened operation. Nuschele et al. [93] described a two-dimensional analytical calculation method for losses in the rotors of PM and concluded that the use of a solid rotor yoke compared to a laminated one strongly reduces the losses in the magnets. However the successful reduction of losses depends on rotor speed, yoke conductivity and segmentation of magnet. Meier and Soulard [94] described the challenges of computing losses in tooth-tips and yoke due to non-uniform flux distribution during estimation of iron loss from measured magnetic flux densities of an SPM machines with concentrated winding. They found major part of the stator core losses under field weakening operation occur in the stator tooth tip.

As stated earlier, increased harmonic content produced by concentrated winding also increase vibrations and acoustic noise. Wang et al. [95] analyzed the air-gap radial force density distribution in three-phase modular permanent magnet brushless machines and showed that the armature reaction field in modular machines produces a rich set of space

harmonics in the air-gap flux density distribution. Araki et al. [96] attempted to reduce the effect of vibrations by the inclusion of the rotor surface with slit in a concentrated winding PM machines. Some configurations of concentrated winding resulted in unbalanced radial forces acting on the rotor due to asymmetrical structure. This was pointed out by Xu et al. [97] where they reported the unbalanced forces for two different 9-slots motor with concentrated winding and observed that the unbalanced radial pull force was largely influenced by the choice of slot-pole combinations. Lee et al. [98] studied acoustic noise reduction according to the change of the pole angle in IPM with concentrated winding. They showed that by choosing optimal opening width, barrier, and pole angle resulted in reduction of normal forces and consequently acoustic noises could be narrowed.

Optimizing the performance of concentrated winding with various types and structure were also investigated by the researchers. Han et al. [99] investigated the rotor core eddy-current losses in IPM machines and showed a trade-off between the rotor and stator losses in the distributed winding and concentrated winding machines. They figured out that in order to reduce the rotor eddy current such specifics such as a narrower slot pitch, lower fundamental ampere turns and wider rotor yoke channel pitch are required. Reduction technique of cogging torque in concentrated winding IPM was proposed or by simple variations of the rotor and stator core geometry [100], by rotor flux barrier shaping [101], or by varying the rotor flux barrier angle [102]. Studies by Lee et al. [103, 104] showed that C-shaped motors were more appropriate for getting better torque density and reducing torque ripple. Lindh et al. [105] addressed the torque production and losses of concentrated winding permanent magnet motors having either semi-closed slots or open slot were studied and they concluded that semi-closed slots give smaller losses than rotor surface magnet motors with open slots. Similar comparison was performed by Salminen

et al. [106] where they noticed that embedded magnet solutions usually have lower copper losses than the surface magnet motors since the prior require less winding turns. Demagnetization characteristics of three types of rotors with concentrated winding IPMSM are studied by Kim et al. [107] where they indicted that double layer model had the most reliable characteristics on the demagnetization among single layer, V- shape and double layer magnet arrangement in the rotor of IPMSM. El-Refaie et al. [108] investigated the eddy current losses in different rotor clamping rings made by metallic, non-metallic, and metallic with shielding laminations and he found that clamping ring of rotor in conjunction with different phase numbers and winding layers, influence the rotor losses. Polinder et al. [109] investigated the eddy current in the solid back-iron PM machines. Though the distributed full pitch winding gives negligible eddy current loss in back iron, the fractional pitch winding gives considerable eddy current loss which affected by number of teeth and pole number. However, if the coil number is half of the total teeth number in fractional pitch machine, the back iron losses are excessive. Nakano et al. [110] studied Eddy current losses of SPM for different slot pole combination and concluded that the huge eddy current in the rotor arises if the armature MMF spatial harmonics are not synchronously rotating with rotor speed. For achieving low eddy current losses in the rotor appropriate slot-pole combination should be selected in consideration the spatial harmonics. Bottauscio et al. [111] applied finite-element method to loss analysis of SPM with concentrated winding. They considered solid and laminated rotors and losses were computed under no-load and loaded conditions. They found PM losses remained constant but huge differences in rotor core losses. Yamazaki et al. [112] showed comparison of rotor magnet losses of IPM, inset and SPM where they reported that lowest magnet loss was achieved by IMP . SPM produced the largest amount of losses which could be reduced by raising the number of magnet segment. Concentrated

winding compared with distributed winding in terms of magnet losses, it was found that the concentrated winding induce higher magnet losses.

Some researchers attempted to derive more computationally efficient and accurate mathematical representation of the concentrated winding model since 3D FE modeling requires large amounts of time and computational resources. Jingai et al. [113] showed three approaches of calculating torque of PM motors such as 1) dq calculation method, 2) The Maxwell Stress formula, and 3) energy method. He also presented mathematical models of concentrated winding brushless PM machines under various operating conditions. The author concluded that the energy method is suitable for concentrated winding machine. Abdemadher et al. [114] derived the inductance of PM motors for both distributed winding and concentrated winding specially to determine the leakage inductance considering the slot, tooth, end winding, and the m.m.f harmonics, etc. The authors found that the direct inductance of the concentrated winding machine is twice greater than the one of the distributed winding machine. The higher direct inductance of concentrated winding machine leads to make wider the flux weakening range. Qu and Lipo [115] described general closed-form analytical expression of air-gap inductance for PM motors with double and single layer concentrated winding. The expressions include all the harmonics and can be easily solved using computer programs. Lumped parameter circuit model for IPM motor with fractional slot concentrated winding was presented by Tangudu et al. [116] where they also described a method to split the terms of reluctance and magnet torque. Duan et al. [117] proposed a fast and efficient design system different from FEA to compare PM machines with distributed winding and concentrated winding where they have used multi-objective functions in the particle swarm optimization method to optimize the design. Meier and Soulard [118] applied d-q theory to a PM

machine with concentrated winding and concluded that the d-q model is reliable for torque and voltage computation of the loaded machine.

At this time, sensorless control of PM AC machines with concentrated winding are gaining more research interests. Elenberger et al. [119] discussed the short circuit properties and the sensorless control capability of an outer rotor PMSM with twelve magnetic pole pairs and two different concentrated winding configurations: single-layer and double-layer winding. They compared the differential inductance in direct and quadrature axis over current load. They concluded that the single-layer stator configuration has an approximate sensorless performance than the other configuration. Imai et al. [120] evaluated the influence of rotor configuration on the robustness of sensorless control for IPMSM with concentrated winding. They showed that the rotor which has salient poles on the side of PM was insensitive to the offset value of the observer. Kojima et al. [121] implemented sensorless control strategies for concentrated winding IPMSM using reduced-order extended-flux observer.

Reigosa et al. [122] evaluated self-sensing performance of either a concentrated winding or distributed winding design of three PMSM. Merits and demerits are evaluated by differential inductance, amplitude of the negative-sequence component, spatial phase (position) error in the negative-sequence component, and the magnitude of secondary saliencies on a loaded machine. It has been concluded that concentrated winding designs produce more saliency, which could improve the self-sensing performance.

Concentrated winding PM machines are well accepted for industrial application. Ionel et al. [123] mentioned the popular use of concentrated winding motors in house-hold appliances in the US. The authors also reported the significant performance improvements of PM machine compared with the conventional line-supplied induction motor technology. Wang et al. [124] focused on the design criteria of high power factor,

high power density IPM with concentrated winding for undersea vehicle propulsions. In this study they showed the trade-off between constant power speed ratio (CPSR) and power factor. Cistelecan and Popescu [125] evaluated the main performance of the low speed, multi-pole PM generator with CW. They found that the fractional slots/pole windings exhibit an important space mmf harmonics content and thus torque ripple and additional core losses are present. Alberti et al. [126] designed an integrated starter-alternator drive which supports a high overload and an adequate flux- weakening operating region. Germishuizen and kamper [49] designed a 150kW railway traction machine in which they described different design aspects of the IPM machines. Kazim et al. [127] designed in-wheel traction motor and concluded that the most suitable machine for this particular application is concentrated winding SPM among various investigated winding configurations and machine geometries. El-Refaie [48] analyzed fractional-slot concentrated winding PM in terms of opportunity and challenges which includes design of the PM, achieving high-power density, flux weakening capability, comparison of single versus double layer windings, fault tolerant rotor losses, comparison of IPM versus SPM. He also provided summary of commercial applications of concentrated winding PM.

Space harmonics in the airgap mmf distribution is the concerns for producing core loss harmonics in concentrated winding fractional slot machine. Figure 3.3 shows the mmf waveform of 10 poles 12 slots double layer IPMSM which is included in this research project. It is necessary to split the mmf waveform into its harmonics components in order to bring into focus the impact of stator mmf harmonics on core losses. A Fourier series can be used to expand the mmf harmonics. Thus the total core loss can be calculated by superimposing the core losses corresponding to the mmf harmonics.

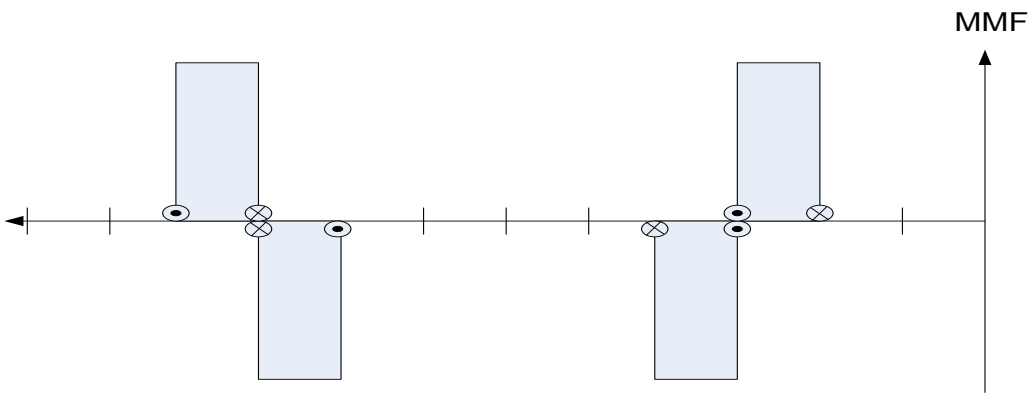

Figure 3.3 mmf waveform of 10 poles 12 slots double layer IPMSM

The three phase mmf of a symmetrical winding can be represented by the equations (19-21)[65] where equation (20) and equation (21) represent the forward and backward rotating mmf harmonics. Figure 3.4 shows the mmf harmonics component for 10 poles 12 slots double layer machine. Odd harmonics (HO=1,5,7, 11, 13,17,19.....), are present in the harmonic profile. It can be shown from equation (20) and equation (19) that the forward rotating mmf space harmonics are for n = 5,11,17 and so on, and backward rotating harmonics for n = 1, 7, 13,19 and so on, both rotating mmf harmonics are depicted also in Figure 3.4

$$M_{3\,ph(n)} = \sum_{n=\frac{1}{p}}^{\infty} \sum_{c=1}^{n_c} \frac{2N}{np\pi} \sin\left(\frac{n\pi}{2} \cdot \frac{\tau_{cc}}{\tau_p}\right) (M^+ + M^-) \tag{19}$$

$$M^+ = \hat{I} \cos(\omega t - n(\gamma - \theta_c)) \left[\frac{1}{2} + \cos\left(\frac{2\pi}{3}(n-1) + 2\pi.n.n_y\right)\right] \tag{20}$$

$$M^- = \hat{I} \cos(\omega t + n(\gamma - \theta_c)) \left[\frac{1}{2} + \cos\left(\frac{2\pi}{3}(n+1) + 2\pi.n.n_y\right)\right] \tag{21}$$

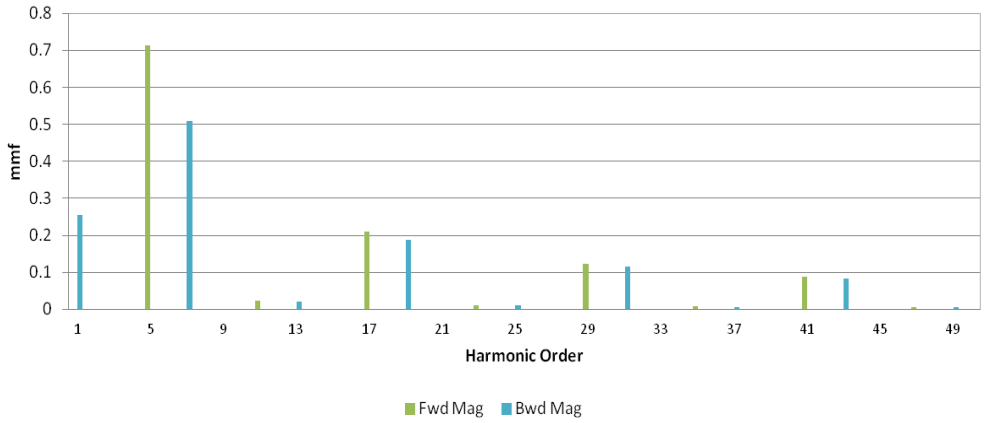

Figure 3.4 MMF harmonic contents of 12 slots 10 poles double layer winding IPMSM

It is found from Figure 3.4 that, as expected the significant harmonics for mmf are 1st 5th and 7th order harmonics, thus the air gap flux densities of those mmf order can be represented by the equation, which take part significantly to affect the core losses of the machine. However, the significant harmonic core losses are not same for the rotor and stator. The significant airgap harmonics can be found from the following magnetic flux equations.

$$B_1 = \widehat{B_1}\,\mathrm{Cos}(\theta + \omega_e t) \tag{22}$$

$$B_5 = \widehat{B_5}\,\mathrm{Cos}(5\theta - \omega_e t) \tag{23}$$

$$B_7 = \widehat{B_7}\,\mathrm{Cos}(7\theta + \omega_e t) \tag{24}$$

The electrical angular frequency and the rotor reference frame can be represented by the following equations

$$\omega_e = \omega_s * P \tag{25}$$

$$\theta = \omega_s t + \alpha_1 \tag{26}$$

Now re-arranging equation (22-24) for specific pole pair, example 5 pole pair machine

$$B_1 = \widehat{B_1}\,\mathrm{Cos}(1.2 * \omega_e t + \alpha_1) \tag{27}$$

$$B_5 = \widehat{B_5} \cos \alpha_1 \tag{28}$$

$$B_7 = \widehat{B_7} \operatorname{Cos}(2.4 * \omega_e t + \alpha_1) \tag{29}$$

From equation (27-29) it is evident that fundamental flux density produce 1.2th order and its multiple core losses harmonics. Whereas 7th harmonics flux density produces 2.4th order and its multiple core loss harmonics. However, there is no time varying harmonics effect on rotor core losses for 5th harmonic magnetic field. Hence the above existing harmonics and its multiple harmonics take place in rotor core losses. On the other hand, the fundamental, 3rd, 5th and 7th harmonics core losses control the stator core loss.

Chapter 4

Measurement of magnetic properties

The magnitude and direction of flux are varied in the cores with the speed of electric machines. Depending on the application, the core loss should be measured considering rotational flux and alternating flux/pulsating flux. A rotational magnetic flux, which is quite different to alternating flux, varies with time in the magnetic core materials of a rotating electrical machine. The rotational magnetic flux is observed at the back of the slot and at the root of the teeth of an electric machine[128]. Li et al. [129] investigated the core loss under three dimensional rotational fluxes and found that the rotational core losses are nearly double of the alternating core losses provided the flux density is the same. Guo et al. [130] extensively reviewed the rotational core loss measurement of electric machines. The author found that there is no standard model for rotational core loss measurement as it follows complicated mechanism. On the other hand, commonly used some experimental apparatus and techniques such as Epstein frame, toroid tester and single sheet tester are used to measure the pulsating core loss of electrical steel sheets, which are standardized by the American Society of Testing and Materials (ASTM).

4.1 Epstein Frame

Epstein frame is the device which is used for measuring the magnetic properties of the machine core materials. About 100 years ago the first Epstein frame dimension was 50 cm which had a butt joint. That frame would give a poorer result due to the increase of magnetic reluctance which was the cause of having butt joint. There are different types of Epstein frame with lap joint used for magnetic properties test of core materials [35, 131] such as 28cm × 28cm 700turns, 25cm × 25cm 700 turns, 25cm × 25cm 352 turns, 25cm × 25cm 280 turns Epstein frame. However, a standard Epstein strips 30.48cm × 3 cm is used in 25cm × 25cm 700 turns Epstein frame where primary and secondary

windings turns are the same. Multiple of four strips are used based on different frequencies for magnetic properties. The Epstein strips are cut into two directions; across the rolling direction and along the rolling direction. Same type strips are loaded in opposite limbs of Epstein frame and other type strips loaded in other two opposite limbs of Epstein frame in order to decrease the consequence of anisotropy on measurement of magnetic properties of the core materials. Despite the magnetic path of the Epstein frame varies with excitation frequency, peak flux density, permeability as well as anisotropy of the material under test, the magnetic path is assumed to be 94cm for 25cm × 25cm 700 turns Epstein frame[132]. One of the limitations of this Epstein frame is that the distributed flux density on the strips is not uniform as leakage flux take place around the joints of the frame [133]. The Epstein frame core loss tests can be represented as an open circuit secondary transformer. The secondary voltage of the Epstein frame test can be calculated based on Faraday's laws of induction given by the equation shown below.

$$v_s(t) = N_s A \frac{dB(t)}{dt} \tag{30}$$

It is seen from the equation that higher secondary voltage is required to get the higher flux density. Hence, optimizing the cross section area by reducing number of strips and using moderate turn number Epstein frame is the solution to reduce the secondary voltage level. The drawback of using Epstein frame is time consuming for loading the strips inside the Epstein frame. Figure 4.1 shows a 700 turn commercial Epstein frame where the total turns spread over 175 turns per limb of the square, Epstein strips and the electromagnetic circuit of core loss measurement using Epstein frame.

(a) (b)

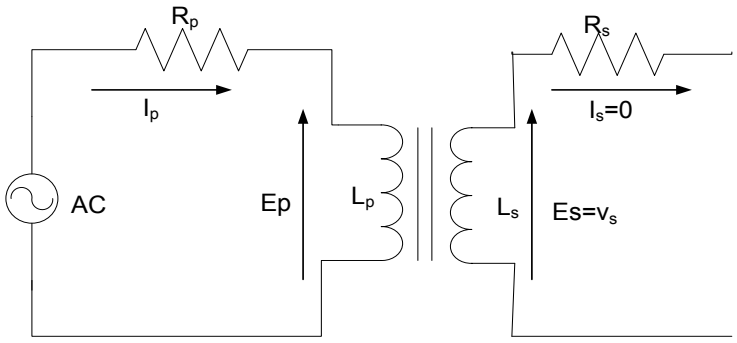

(c)

Figure 4.1 (a) Epstein frame (b)Epstein strips and (c) electromagnetic circuit of core loss measurement

4.2 *Toroids Tester*

Basic mechanism of toroid test and Epstein frame test are the same. However, the core material used in toroid is wound shape unlike Epstein frame strips. Thus the toroid test avoids the corner effect of Epstein frame which is liable for flux leakage. The toroid has a variable number of turns in primary and secondary windings. Like Epstein frame test, the excitation voltage is applied to the primary winding and the induced open circuit voltage measured on the secondary winding. The secondary voltage and electromagnetic circuit can be represented like Epstein frame. As the core material is fixed in toroid test at all flux density level, choosing the proper number of primary and secondary turn ratio limits the secondary voltage especially at high flux density level. For small radial motors, the toroid test is comparatively accurate than the Epstein frame test as the core geometry

of toroid is similar to that of radial flux machines. However, using smaller toroid the test result may be less accurate in case of cutting stress of the sample disseminate to the center of the samples. Stress relieving of the sample might be the solution to avoid this difficulty. The longer preparation time for making the core properly wound make it less attractive. Figure 4.2 shows toroid core geometry with and without primary and secondary coil.

(a) (b)

Figure 4.2 Toroid core geometry (a) with coil (b) without coil

4.3 Single sheet tester (SST)

This device use single sheet sample. It has a wide range of magnetic circuit based on flux closure yokes and without flux closure yoke. The advantages of using flux closure yoke over without flux closure yoke is that it is easy to achieve a uniform magnetization region. Flux closure yoke could be two types: single sided yoke, double sided yoke. Eddy current pool which falsely increase the measured losses, might be the cause of using single sided yoke. This false increase loss can be avoided using double sided yoke as the double sided yoke cancel the eddy current effect largely. Hence, double sided yoke are suggested by international standard. Using of low length/width ratio square sample restricts the travel path of flux and hence active path length of the flux can be an issue

[134]. The drawback of using double yoke SST is costly, heavy and large. Hence, to avoid the damaging effect on the sheet due to heavier yoke, pneumatic suspension might be used with yoke. The smaller size SST severely affected by the sample cutting edge. The flux path length of SST is determined calibrating with toroid tester or Epstein frame tester. Figure 4.3 shows the commercial tester and double sided yoke of SST.

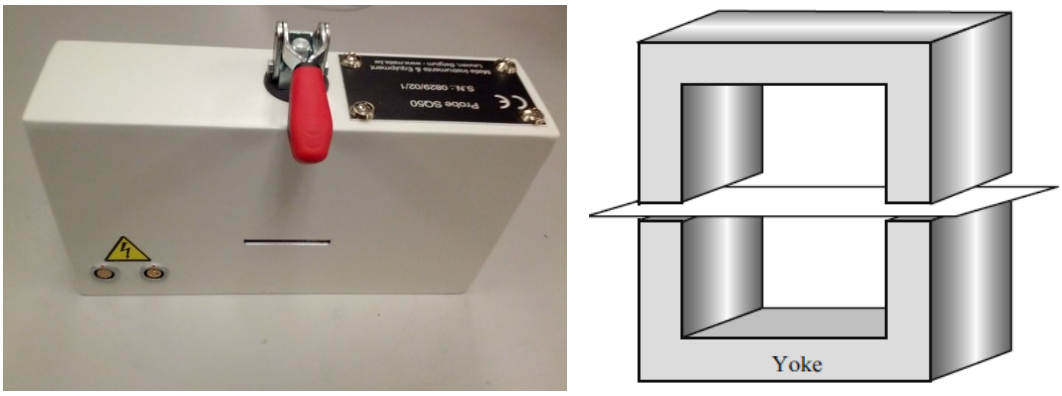

(a) (b)

Figure 4.3 SST (a) Commercial tester (b) Double sided yoke with sheet

The Epstein frame and toroid tester are self dependent in term of flux path length. Though among the three testers the SST is comparatively easy in terms of preparation the tester and setup the test the Epstein frame widely used to test the magnetic properties of the core materials. A total of around 1200 effective tests have been done to analyze the magnetic properties of the sample materials for the project. These tests include 16 DC Epstein test, 512 AC Epstein test, 65 DC toroid test and 654 AC toroid tests. Though lots of tests have been done, only seven set of Epstein data are selected to evaluate the core loss in physical model and simulation model.

4.4 Test Bench Description

Epstein frame test and toroid test were carried on for the same core material in this project. The test setup for Epstein frame tester and toroid tester are same except the tester. Though both tests have been done on the same materials Epstein frame test results are

used to analyze the motor model. An Epstein frame integrated with a computerised measurement system established using LAB-VIEW, is used in order to obtain the magnetic properties of different samples of lamination steels. In experimental setup, a 700 turn 25cm Epstein frame is used. The excitation signals are generated by means of a LABVIEW program in real time simulation. A 100V, 20A linear amplifier with frequency range from 0Hz to 20 kHz is used to excite the Epstein frame. Primary excitation current and secondary voltages are measured using current and voltage probes connected to a digital storage oscilloscope. Prior to each test, samples are demagnetized by applying a primary voltage 10% higher voltage than the magnetizing voltage required during testing so that the magnetic domains of the sample reverts to the initial position. During testing integration of the secondary voltage to obtain the flux density waveform is carried out digitally after the measurements are completed. All calculations are carried out in the manner described in ASTM A348M, 343M, and A773. Figure 4.4 shows the setup bench of an Epstein frame test and

Figure 4.5 shows the Schematic diagram of the Epstein frame test.

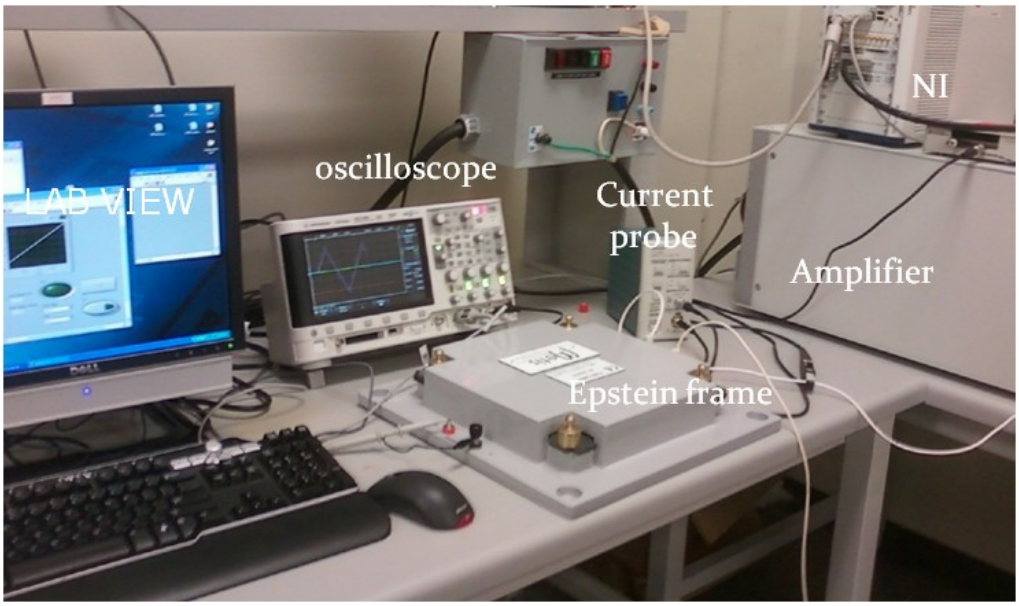

Figure 4.4 Epstein frame test setup bench

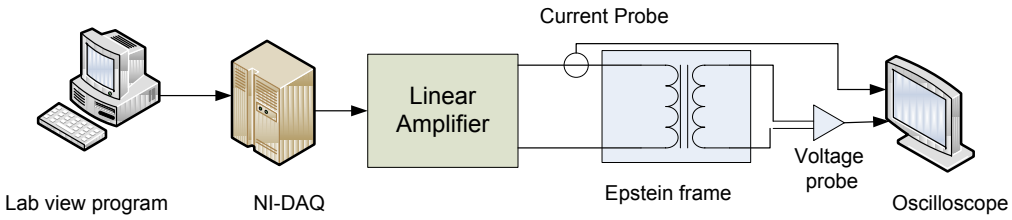

Figure 4.5 Schematic diagram of the Epstein frame test

4.5 Magnetic properties evaluation

Different characteristics such as dc relative permeability, ac peak permeability, dc and ac magnetizing curves, core resistor, specific core loss are obtained by post processing current and voltage data together with measured length and mass of the samples. As is well known, low-loss and high-permeability steel is an excellent candidate for developing energy-efficient electromagnetic machines [135]. DC tests were carried out by slowly increasing the primary applied field intensity over a period of 20 seconds. The calculated flux density is obtained by integrating the secondary voltage. Magnetise properties are plot separately based on different categories of steel such as Stress relief annealing(SRA)/ Non-SRA, heat treatment/ No-heat treatment in order to itemise easily in later section.

Stress Relief Annealing (SRA)

Materials are inclined to include stress due to work hardening or thermal cycling. SRA is a process in order to reduce the stress of the material. This process is done by means of heating the materials up to 600-650°C, holding the material at that environment for an extended time (one or more hours) and finally cooling in quiet air.

Heat treatment

Heat treatment is a process where controlled heating and cooling is applied to the metal in order to change the mechanical and physical properties of the metal without affecting the product shape. There are different types of heat treatment used on the metal such as T6, T61, T5, and T51. However, T61 heat treatment process includes solution

heat treatment (temperature 538°C), then quench followed by artificially age. By increasing the maximum tensile, this heat treatment increases the material strength with adequate elongation of material. On the contrary, T5 heat treatment is done at a lower temperature compared with T61 heat treatment. It includes artificially aged at 225°C only. By stabilizing the castings dimensionally, T5 heat treatment improves machinability and relives stress.

4.5.1 Magnetic properties of SRA materials

Figure 4.6 shows the different magnetic properties of SRA and Non-SRA materials. The DC relative permeability calculated according to ASTM A773/A773M is presented in Figure 4.6(a). Initial magnetization curves are shown in Figure 4.6(b). From Figure 4.6(a), it is seen that after SRA the relative permeability of the steel is significantly higher at range of flux density level 0.6T to 1.2T and moderately higher at lower flux density levels. At 1.5T, the relative permeabilities of each sample are very similar as the core material tends to saturation. AC testing of the samples is carried out at 50Hz, 60Hz, 100Hz, 200Hz, 300Hz, 400Hz, 1 kHz and 2 kHz. Test data is used to calculate properties such as peak permeability and core loss density as per ASTM 343M, A348M standards. The peak relative permeability for the AC tests is calculated at a range of flux density values. Due to voltage limitations, the peak flux density at the higher frequencies is reduced. Data measured at 1.5T for frequencies from 50 Hz to 400 Hz are shown in Figure 4.6(c); at 1000Hz and 2000Hz the flux density is reduced to 0.75T. It can be seen that the SRA lamination steel has a higher measured peak permeability at a given flux density and frequency when compared with non-SRA steel. This hysteresis behavior of the SRA and non-SRA steel at 50Hz, 1.5T is plotted in Figure 4.6(d). The area of BH the loop differs depending on frequency, flux density and material properties. The wider hysteresis loop reveals higher coercivity, higher residual magnetism, higher reluctance,

higher retentivity, lower permeability. It also reflects the higher overall energy per cycle and higher core loss per unit volume.

Measured loss curves as functions of flux density at each frequency are plotted in Figure 4.6(e) for the SRA sample and Figure 4.6(f) for the non-SRA sample. Both plots exhibit the expected increase of losses with flux density and frequency. Comparing the two sets of measurements, the sample that has been treated with SRA has lower measured losses than the non-SRA sample.

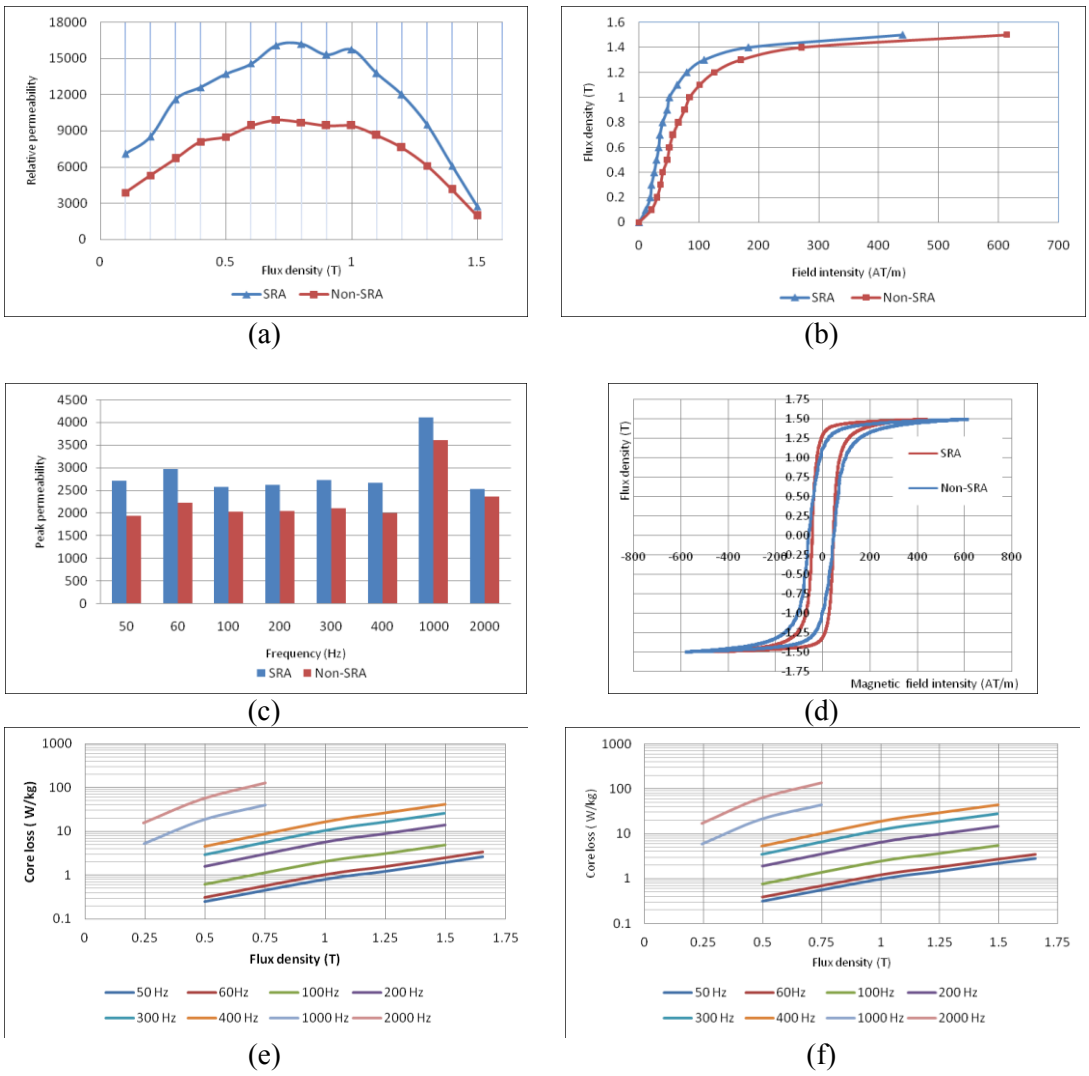

Figure 4.6 Magnetic properties of SRA and Non-SRA material (a) DC relative permeability (b) Initial DC magnetization curve (c) AC peak permeability (d) BH curve at 50Hz and 1.5T (e) Core loss curves of SRA core material (f) Core loss curves of Non-SRA core material

4.5.2 Magnetic properties of Heat treated materials

Figure 4.7 shows the magnetic properties of different heat treated materials. Figure 4.7(a) plots the relative permeability of different heat treated materials. The T61 sample has a higher relative permeability below 0.6T but saturates at a lower flux density that the T5 sample and the sample without heat treatment. As a result, the relative permeability for the T61 sample is significantly lower than the other two samples in the range from 0.7T to 1.5T. Figure 4.7(b) plots the measured B-H characteristic for the sample with T61 heat treated, T5 heat treated and the sample that has not been heat treated. It can be seen that the T5 heat treatment results in a magnetization curve that is very similar to that obtained from the sample that has not been heat treated. However, the T61, heat treatment results in a significant change to the magnetization.

Figure 4.7(c) presents the data on the peak ac permeability at a range of frequencies. Ac peak permeability at 1.5T for the 50Hz – 400Hz tests and at 0.75 for 1000Hz-2000Hz are included in the plot. It can be seen that frequency has a much smaller impact at 1.5T, when the samples are saturated. The result observed in the dc results that T61 negatively impacts the permeability - are again clear in these results. In addition, at 1.5T, the sample subjected to T5 heat treatment has slightly lower AC peak permeability than the sample that has not been heat treated.

The area of an AC hysteresis loop characterizes the energy loss per cycle. AC hysteresis BH loops for the samples are shown in Figure 4.7(d), where the loop frequency is 50 Hz and maximum flux density level is 1.5T. It is found from the post processed of Epstein test results that, as expected, the BH loop areas are higher with the increase of either frequency or/and flux density level for each sample. It is clearly seen from Figure 4.7(d), the curve for T5 heat treated sample and the sample that has not been heat treated shows the flux density,B increases rapidly with an increase in flux intensity,H. The rate

of increase of B with H is lower for the T61 heat treated sample, before magnetic saturation. In addition, the BH loop for T61 sample has the highest loop area which depicts the highest core loss. The BH loop area of the sample that has not been heat treated has the lowest area, which is similar to the area of the BH loop of the T5 heat treated sample. Therefore, the sample that has not been subjected to heat treatment has the lowest core losses whereas the T61 heat treated sample gives the highest core losses at 1.5T.

The specific losses of the 3 samples in W/kg are plotted in Figure 4.7(e-g). It is seen from these Figures that the core losses increase with the increase of frequency for all the samples at any specific flux density level. The core losses of T61 sample are in the range of 18-22% higher than the sample that has not been heat treated at 1.5T (50-400Hz) and 0.75T (1000-2000Hz). Similar analysis of the T5 data indicates an increase of 2.8-9.3% over the sample that has not been heat treated. The percent of increase of the core losses are lower at lower flux density level. The T61 heat treated sample gives the highest specific core losses and the sample without heat treatment gives the lowest specific core losses at any particular frequency and flux density level.

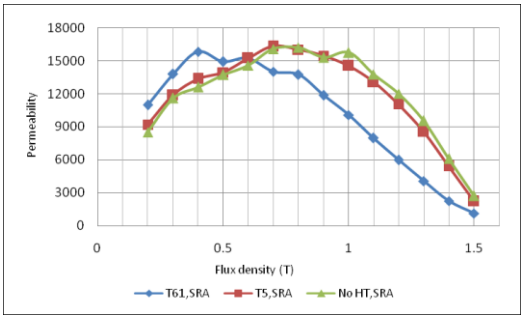

(a)

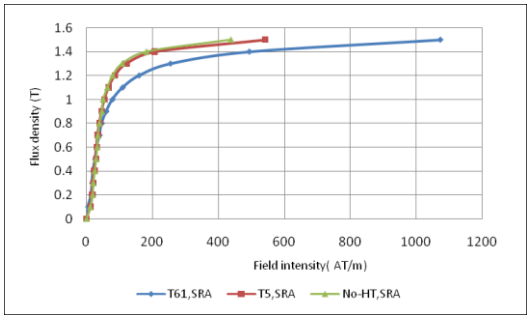

(b)

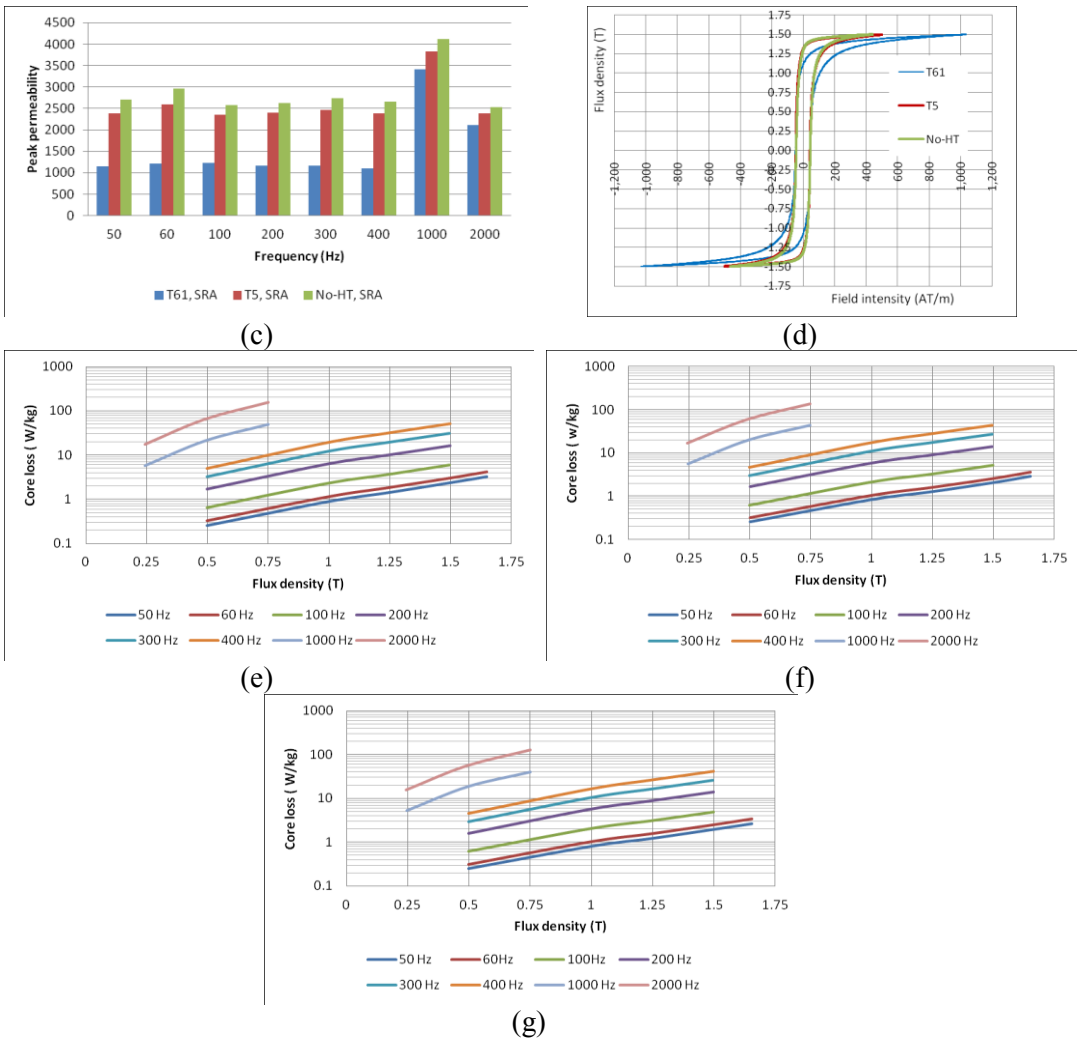

Figure 4.7 Magnetic properties of different heat treated materials (a) DC relative permeability (b) Initial DC magnetization curve (c) AC peak permeability (d) BH curve at 50Hz and 1.5T (e) Core loss curves of T61 heat treated core material (f) Core loss curves of T61 heat treated core material (g) Core losses of sample has not been heat treated

It is concluded from the above figure that the magnetic properties of T5 heat treated material and the core material that has not been heat treated are very close to each other in terms of relative permeability, DC BH curve and AC BH loop. The T61 heat treated core material gets saturated faster than the T5 heat treated core materials and the core material that has not been heat treated. However, the core material that has not been heat treated gives the lowest specific core loss.

4.5.3 Magnetic properties of SRA and No-SRA material used in physical test motors

Two motors were built to validate the loss calculation. Those two motors used the M-19 (AK steel) SRA and No-SRA core material. These core materials are tested using Epsten frame and figure out the following magnetic properties shown in Figure 4.8. However, an updated controlling for Epstein frame test is used to do these magnetic properties tests. The Epstein frame system is capable of controlling the harmonic content of the flux waveform up to the 17th harmonic. Testing is conducted over a wide range of fundamental frequencies and harmonic content. It is found from the figure that the DC permeability of the SRA is significantly higher before saturation compared with No-SRA core materials. The initial magnetisation curve is sharper in case of SRA and same at saturation region. However, extended initial dc magnetisation curve data is used in FEA to investigate the motor model. The ac peak permeability of SRA is higher at 1.5T for frequency level 50Hz- 400Hz and at 0.75T for frequency level 1000Hz-2000Hz. The tread is same as JFE SRA and No-SRA steel. It can be shown that the area of ac BH curve at 50 HZ, 1.5T is higher in case of SRA compared with No-SRA. The core loss at 50Hz, 1.5T can be calculated from the ac hysteresis loop. However, SRA and No-SRA core loss curves reflect that the SRA material gives the lower specific core loss at all frequencies and flux density level.

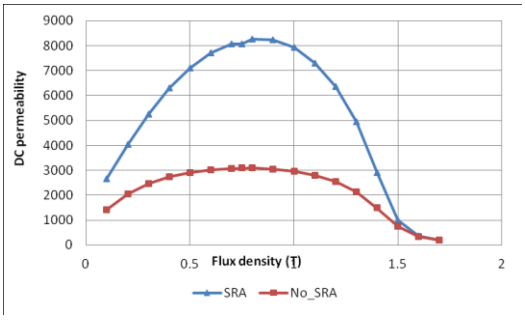

(a)

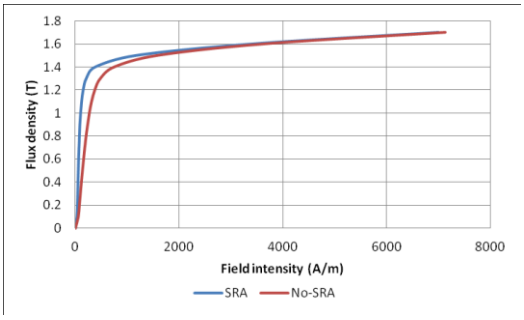

(b)

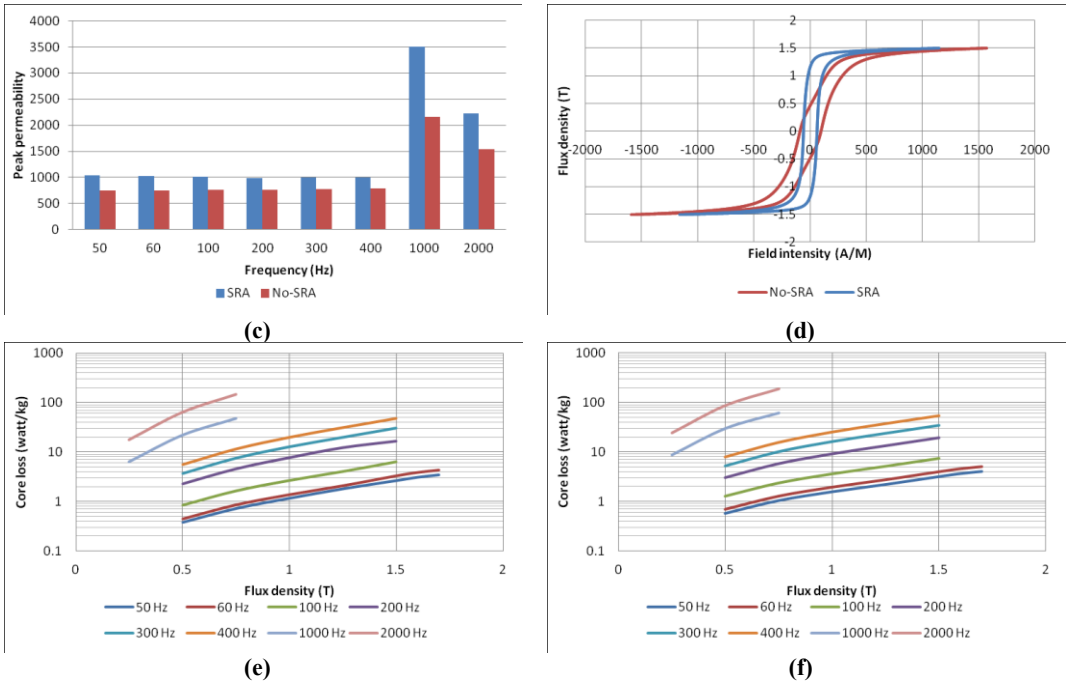

Figure 4.8 Magnetic properties of SRA and Non-SRA material used in physical built motor(a) DC relative permeability (b) Initial DC magnetization curve (c) AC peak permeability (d) BH curve at 50Hz and 1.5T (e) Core loss curves of SRA core material (f) Core loss curves of Non-SRA core material

All the above curve obtained from the epstein frame test data are used to predict the core loss of the motor used the corresponding core materials. Moreover, the results obtained from the Epstein frame test data are used to create tables of losses vs frequency for use in the FE simulations. However for finite element analysis, a DC magnetisation curve should describe the B-H relationship up to any value of flux density that may occur in the simulation. The Epstein test frame is not capable of operation at very high flux densities; moreover, commercial data for high field DC magnetisation curve is rare. Therefore, a numerical approach is utilized to expanding the DC magnetisation curve to very high flux densities, ensuring numerical stability of the FE model [136]. The following equations are used to extend the DC magnetizing curve.

$$v = \frac{H}{B} = v_{diff} + \frac{C}{B} \tag{31}$$

$$v_{diff} = v_0 - (v_0 - v_{df})e^{-\lambda(B-B_f)} \tag{32}$$

$$-0.05v_0 = -\left(v_0 - v_{df}\right)e^{-\lambda} \tag{33}$$

$$v = v_0 + \frac{\left(v_0 - v_{df}\right)}{\lambda B} e^{-\lambda(B-B_f)} + \frac{c}{B} \tag{34}$$

$$c = B_f \left(v_f - v_0 - \frac{\left(v_0 - v_{df}\right)}{\lambda B_f} \right) \tag{35}$$

The extended BH characteristics obtained from the above equation is maintaining reluctivity values close to the expected reluctivity at flux density levels. This extended BH curve without considering the advance magnetisation test facilities, can be used in Initial machine design to get the informed decision.

Chapter 5

Machine Design

The base design is a 1kW, 10 poles, 12 slot machines capable of operation over a wide speed range of 1000 to 6100 rpm. Output power depends on the output torque, so the efficiency can be improved by increasing the ratio of torque per current ampere which leads to the decrease of copper losses. The torque equation is

$$T = \frac{3}{2}\frac{P}{2}\lambda_{pm} i_q + \frac{3}{2}\frac{P}{2}\left(L_d - L_q\right) i_d i_q = T_m + T_r \qquad (36)$$

The *d* and *q* axis flux linkage written as

$$\lambda_d = \lambda_{pm} + L_d i_d = \left(k_w N_{ph}\right)\psi_{pm} i_q + (k_w N_{ph})^2 P_d i_d \qquad (37)$$

$$\lambda_q = L_q i_q = (k_w)^2 P_q i_q \qquad (38)$$

From equation (36), (37) and (38) the torque equation can be written as

$$T = \frac{3P}{4} k_w N_{ph} \psi_{pm} i_q + \frac{3P}{4} {k_w}^2 {N_{ph}}^2 (P_d - P_q) i_d i_q \qquad (39)$$

From eq. (36) it can be seen the torque of the IPMSM can be increased either by increasing magnetic flux linkage or by increasing the difference between L_d and L_q. The inductances' values depend both on the flux and the current, which are also related to the rated voltage. However, the difference of the inductances' values can be obtained by optimal rotor design [137]. The IPMSM has saliency that means different L_d and L_q inductances. As the *d* axis flux has to pass through the magnet, which has low permeability whereas the *q* axis flux passes through the higher permeability core materials, thus the *d* axis inductance is lower compared with the *q* axis inductance. The *q* axis inductance is affected more by magnetic saturation due to a low reluctance path of *q* axis flux. On the contrary, the *d* axis inductance is affected less due to high reluctance of

d axis flux path [132]. The saliency ratio of IPMSM also leads to the achievement of higher power factor and constant power speed range [138].

If the winding has negligible resistance and all the harmonic winding factors are zero except for the fundamental, then at no load condition the magnetic flux induces a back emf in the winding which is approximately equal to the applied voltage. So, using Faraday's Law the rms phase voltage can be written as

$$V_{\text{rms-phase}} = \frac{l_s \omega_e d k_{w1} N_{ph} (\frac{\hat{B}}{\sqrt{2}})}{\frac{p}{2}} \tag{40}$$

However, at loaded condition the maximum torque is limited by voltage and current limits of the driving power inverter of the machine [139]. Therefore the machine should be operated satisfying these current and voltage constraints. The voltage and current constraint are expressed below. (DQ voltage calculation from the machine parameter shown in Appendix B)

$$I_s = \sqrt{I_d^2 + I_q^2} \leq I_{s\,max} \tag{41}$$

$$V_s = \sqrt{V_d^2 + V_q^2} \leq V_{s\,max} \tag{42}$$

5.1 Machine Specifications

Double layer winding configuration is also used to design the winding layout which also gives some better properties compared with single layer winding such as more sinusoidal back emf, shorter end winding and reduction of MMF harmonics. Specific electric loading is important for machine specification which is related to the rated current, and which defines the maximum allowable current density within the machine so that the machine can operate safely without overheating. The specific electrical loading of the designed machine is 30000 A/mm^2. The specific electric loading can be expressed as follows

$$J_e = \frac{3N_{ph}K_{w1}}{\frac{\pi d}{2}} I_{ph} \tag{43}$$

The specific magnetic loading is the maximum allowable flux density level of the magnetic circuit, which depicts whether the magnet circuit part is unsaturated or saturated during the machine operation. It is optimum when the machine is operated around the knee point of the magnetic characteristics. But if the machine is operated in the saturation region, the required current to magnetize the machine becomes higher which leads to access I^2R losses and might produce unwanted harmonics into the stator winding. Specific magnetic loading is 0.6 T. The air-gap flux density of the machine can be predicted from specific magnetic loading. However the average air-gap flux density over one pole pitch is equal magnetic loading expressed as

$$B_m = \frac{2\sqrt{2}}{\pi} B_{rms} \tag{44}$$

5.1.1 Rotor and Stator dimensions

Analytical formulas are usually used to calculate the dimensions of an electrical machine. Nominal power of the motor related to deciding the diameter size of rotor. The higher rotor diameter increase the torque and thus power as the rotor having higher diameter can offer higher magnetic loading by inserting the higher volume of magnets inside the rotor[140]. However, a thicker back iron is recommended to avoid the magnetic saturation when lower pole number is used in rotor[141].

However, the increased rotor diameter limits the stator effective area. Hence the specific magnetic loading is decreased due to decreased current injection area when current density is constant. So a moderate rotor diameter size is preferred to maximize the torque. Equation (45) and (46) are used to calculate the rotor size of the machine.

$$Air\ gap\ volume = \frac{60S_a}{\sqrt{2}\pi^2 B_m J_e N_{ss}} \tag{45}$$

$$Air\ gap\ diameter, d = 2 * \sqrt{\frac{Air\ gap\ volume}{\pi l_s}} \tag{46}$$

The stator diameter is calculated taking into account the air-gap diameter, slot depth and stator yoke. The tooth width, slot width and slot depth shown in Figure 5.1 and can be calculated by the following equations.

$$AGC = \pi d \tag{47}$$

$$W_T + W_s = \frac{AGC}{Slot} \tag{48}$$

$$\frac{W_T}{W_T + W_s} \tag{49}$$

$$d_s = \frac{Slot\ ares}{W_s} \tag{50}$$

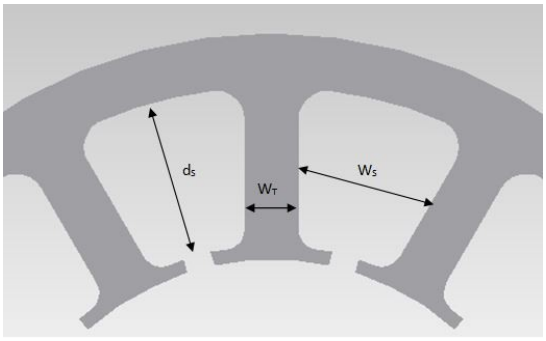

Figure 5.1 Tooth width, slot width and slot depth of the stator

5.1.2 Selection of slot pole combination

Different slot pole combination value effect the machine characteristic. The slot pole combination should be chosen so that the lowest common multiple (LCM) of slots and poles number is high as possible in order to reduce the cogging torque magnitude and increase the cogging torque frequency. In order to reduce the net radial force of the motor the slot and pole combination should be selected such a way that the greatest common divisor (GCD) is even number. However the winding factor depends on the slot-pole combination. Based on those criteria the slot per pole per phase (SPP) values 2/5 or 2/7 is

revealed the best candidate. However, to eliminate the rotor core loss due 5th harmonic air gap flux density, 2/5 SPP is selected. As the machine is 3 phase, 12 slots and 10 pole is the best choose for this machine model.

5.1.3 Winding design

This machine winding is non-overlapping concentrated winding which reveal the winding type is fractional slot concentrated winding[142]. However, "concentrated windings can be characterized by slot per pole per phase. The higher winding factor, which reflects higher torque, depends on the combination of pole and slot. Results, for the same rated toque, the motor having higher winding factor required lower turn number. The numbers of turn of the winding can be calculated using the equation (51) and (52). The winding layout also depends on slot-pole combination. Figure 5.2 show the winding layout of the 10 pole 12 slot double layer concentrated winding machine.

$$N_{ph} = \frac{V_{\text{rms-phase}} * (\frac{P}{2})}{\left(\frac{\hat{B}}{\sqrt{2}}\right) * l_s * d * \omega_e * K_{w1}} \tag{51}$$

$$N_{slot} = \frac{N_{ph} * 2 * phases}{Slot * N_l} \tag{52}$$

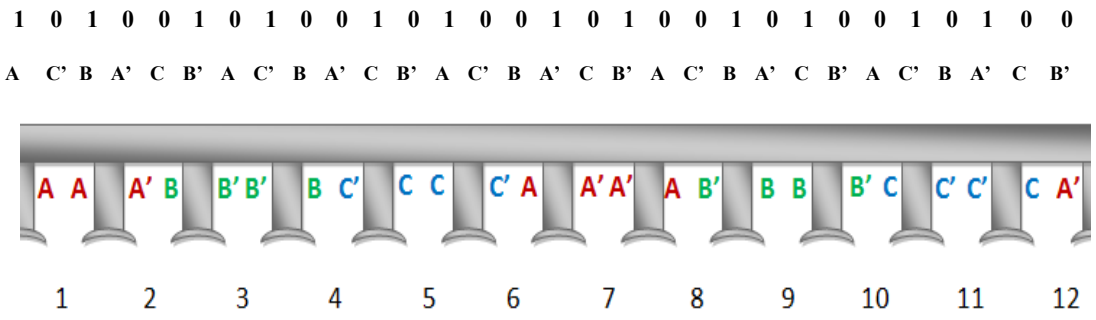

Figure 5.2 Winding layout of a 10-pole, 12-slot IPMSM

The vector S, which is used to calculate the winding factor, represents the numbers of slot corresponding to phase A.

S = [1 1 -2 6 -7 -7 8 -12]

The vector for the phase voltage resultant phasor can be expressed as follows and the slot voltage can be represented by spoke method. Then the resultant phase voltage can be easily drawn considering voltage phasor and the slot voltage. Figure 5.3 shows the slot voltage, phase **A** voltage. Other two phase voltages can be figured out following the same manner.

Phase A = [1 6 -7 -12]

Phase B = [2 -3 -8 9]

Phase C = [-4 5 10 -11]

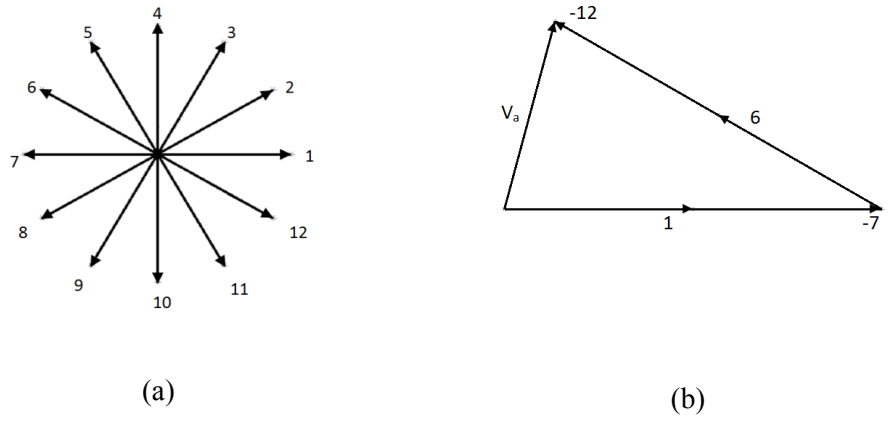

(a) (b)

Figure 5.3 10 pole 12 slot IPMSM (a) slot voltage (b) phase A voltage

5.1.4 Magnet Bar

Rare earth magnets are popular for having the higher energy product compared to other magnets. Neodymium (Nd) and Samarium(Sm) alloy are commonly used to form rare earth magnet. The most available commercial rare earth verities are Neodymium-Iron-Boron ($Nd_2F_{14}B$) and Samarium Cobalt ($SmCo_5$, Sm_2Co_{17}). However, Neodymium-Iron-Boron gives higher remanent flux density, higher energy product and higher coercive force. The magnet has reversible magnet properties reflect that the operating point moving along the BH curve without demagnetization even if the operating point moved beyond the knee point on a nonlinear BH curve during any operating condition.

There are two types rare earth magnet available. One of them are sintered and other is bonded. The energy product of sintered magnets is much higher compared with bonded magnet. However, the maximum energy product of the same magnet material can be expressed by the grade of the magnet. So, a sintered reversible rare earth permanent magnet ($Nd_2F_{14}B$) is used as the pole in the rotor. A rectangular permanent magnet bar is selected to reduce the cost instead of an arc type magnet. The rotor bars are placed under the same pole in such a way that the angle between the two bar magnets is 36 degrees. The magnetisation direction of the magnet bar is chosen parallel to the age of width of magnet so that the flux passes through the tooth core for linking with the stator coil. This magnet needs to be selected satisfying magnet orientation as well as the magnet dimensions to get the optimum current control. However, finite element analysis is needed to select the magnet orientation and choosing the magnet strength.

Using analytical method different dimensions of the machine are listed on Table 5.1 and rotor and stator schematic are shown in Figure 5.4

TABLE 5. 1 DIMENSIONS OF THE MACHINES

Specification	Dimensions
Stator outer diameter	145 mm
Machine Air gap diameter	79 mm
Tooth width	7.82 mm
Sloth depth	23.2 mm
Stator stack length	60 mm
Number of turns per phase	46
Winding factor	0.933
Magnet type	NEOMAX 32H

Magnet width	2.5 mm
Magnet Length	10 mm

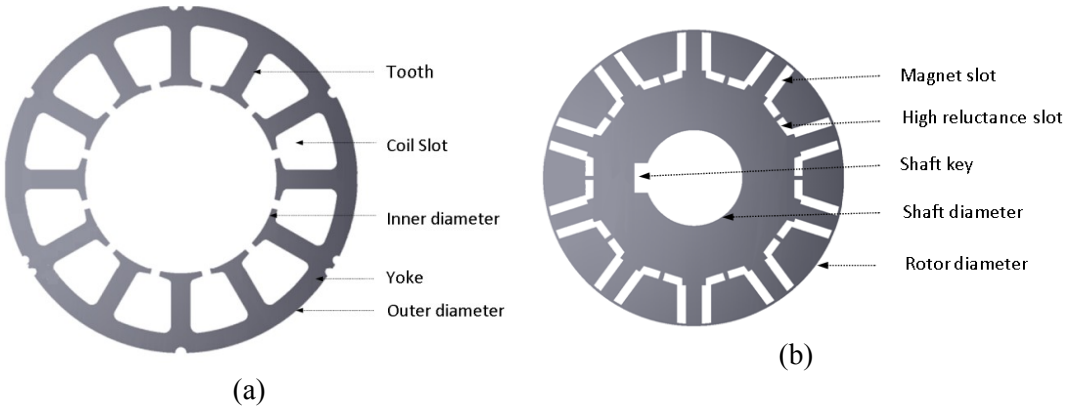

Figure 5.4 Schematic of designed motor (a) Stator and (b) Rotor

5.2 FEA Analysis

This part presents analysis of the influence of design choices on the performance of an interior permanent magnet synchronous machine with concentrated winding designed to operate at constant power over a wide (six to one) speed range. As a Finite element analysis (FEA) is more accurate than analytic method[99], the main goal of this research project is to design a machine using JMAG (FEA software) to estimate the core losses accurately and identify major harmonic sources, which are liable to increase the core losses at higher speeds. So, FE analysis was performed to find the best geometrical solution and to find the appropriate magnet strength bar used in the machine.

The influence that winding design and magnet field strength have on the balance between copper and iron losses in the field weakening region is investigated. Three different cases based on magnet orientation making different angles between magnet bars in the same pole and one different PM strength in the rotor of PMSM have been investigated for core losses in a wide speed range under loaded and no-loaded condition. Voltage, torque, and power have been made effective for all the cases under loaded

condition. Finally, effect on efficiency due to different core loss components and joule losses, which are the result of design variation, are depicted.

Since the supply voltage of the machine has to be optimized, the L_d and L_q are also calculated. It is necessary to predefine the exact value of *dq* inductances before the final design of IPMSM, since L_d and L_q are related to torque and speed characteristics specifically when the machine is controlled by field weakening [143]. It is very difficult to calculate the *d* and *q* axis inductances analytically due to magnetic saturation on the core [144]. Moreover, L_d and L_q inductance values are varied with the flux weakening current. So, some interpolation is needed to get the inductance value at flux weakening current so that the voltage is optimized considering the flux weakening current and corresponding inductance values.

The calculation of the iron losses is performed by FE simulations and improved using loss separation principle which considers the skin effect of the eddy currents in the steel sheet.

5.2.1 Influence of magnet orientation

Three different designs capable of operation over a wide speed range starting at 1000rpm and ending at 6100rpm have been investigated for core losses. In the first case, the angle between two magnet bars of rotor under the same pole is 36 degree. For the 2nd and 3rd case, the magnet orientation has been changed without changing anything else so that the angles between two magnet bars are 67.4 degree and 106.88 degree respectively. i.e. the volume of magnetic material and the directions of magnetization of the magnet bar remain the same for all cases. These three cases are shown in Figure 5.5.

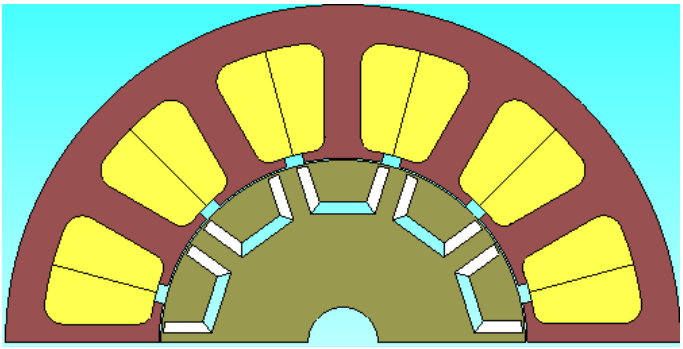

(a) Case 1

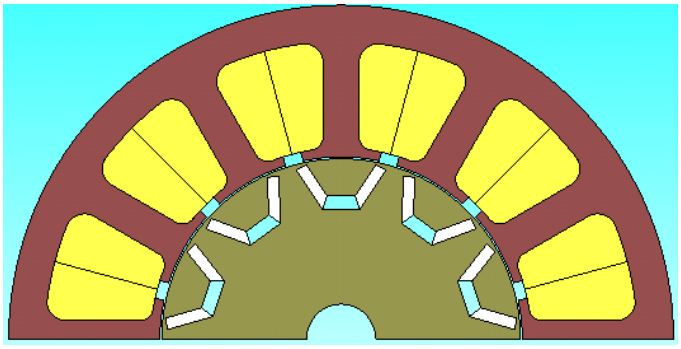

(b) Case 2

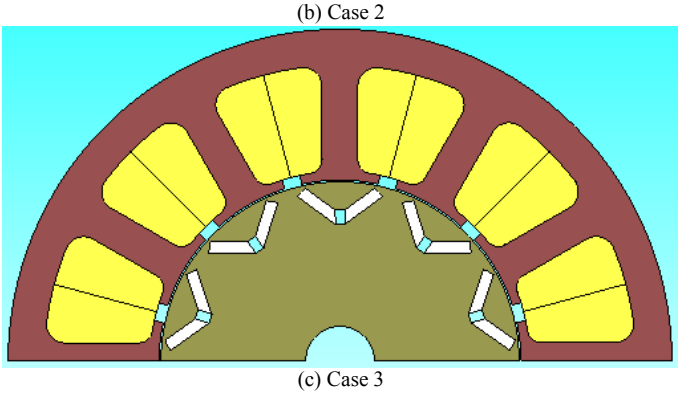

(c) Case 3

Figure 5.5 Schematic of three different cases

Though the three cases have different load current as well as different open circuit voltage due to different flux linkage with the winding, the torque and power in wide speed ranges are same shown in Figure 5.6. In general the torque per amp is higher at base speed and decreases with the increase of speed for all the three cases. The flux control current i_d is designed non zero from the beginning of the control scheme to use the reluctance torque and to optimize the efficiency by controlling the air gap flux [145]. The negative d-axis current is increased to provide more flux weakening so that the speed

is increased. On the contrary the required q-axis current is decreased with an increase in speeds as the required torque is decreased with an increase in speeds.

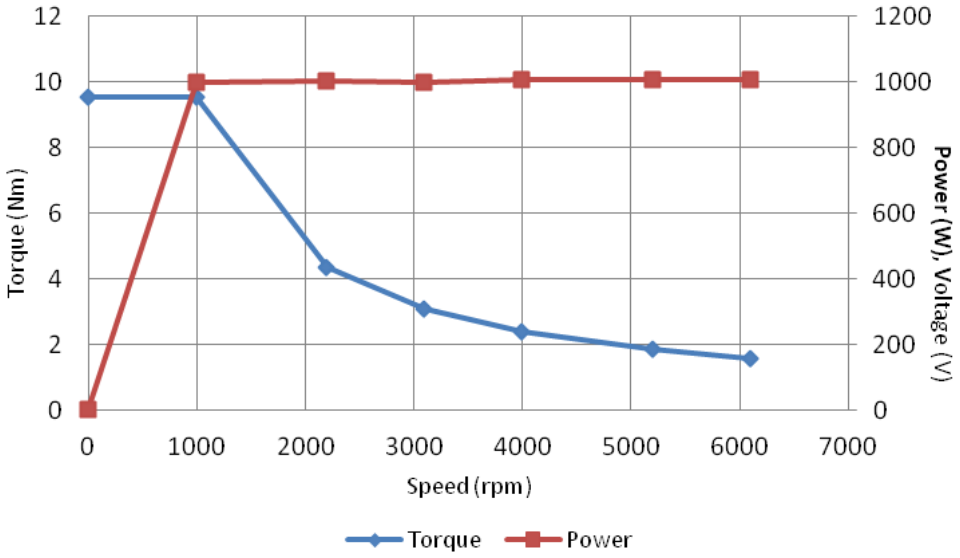

Figure 5.6 Output power and torque in wide speed ranges for three cases

The torque is constant before the base speed and its value is 9.55 N-m. Output torque is changed to get the constant output power at the flux weakening region under loaded condition and it varies from 9.55 N-m to 1.57 Nm. The power is 1000 watts in the flux weakening region and this power is proportionally increased with the speed before base speed. It is seen from the Figure 5.6, as the torque is constant before the base speed, that the machine maintained constant volt/hertz up to the base speed. The saliency ratio of IPMSM leads to the achievement of higher power factor and constant power speed range. Though the magnet volume is the same of that of the magnet NEOMAX 32H and the winding turn numbers are the same, the flux linkage of the coil is different and the inductance values also different for different cases shown in Table 5. 2. In case-1 the flux linkage is 143 mWb whereas for case-2 and case-3 the flux linkages are 142.5 mWb and 143.1 mWb respectively. In these models, the inductances and flux weakening current maintain dq voltage so that the supply voltages are almost same and its value is the rated voltage which is 140 V for all the cases.

TABLE 5. 2 DQ INDUCTANCES AT DIFFERENT SPEEDS

Speed (rpm)	Case1		Case2		Case3	
	L_d(mH)	L_q (mH)	L_d (mH)	L_q (mH)	L_d (mH)	L_q (mH)
1000	7.70	13.79	7.93	13.98	7.53	13.67
2200	10.86	17.01	11.06	17.72	11.83	18.05
3100	12.13	17.25	11.94	17.81	12.57	18.24
4000	12.13	16.95	11.65	17.32	11.97	17.75
5200	11.62	16.47	10.91	16.60	10.78	16.86
6100	11.30	16.19	10.39	16.15	10.04	16.25

5.2.1.1 Core loss

Core loss is simulated under loaded and no-loaded conditions. When calculating the core loss with FFT for harmonic components, the FFT calculates flux density harmonics and losses for number of harmonics set by the number of steps per cycle. Noise in the FFT calculation affects in a large number of low-magnitude flux density, high frequency and a prediction of excessive total loss. To ensure that spurious harmonics are not included in the calculation, a plot of the loss FFT is reviewed and harmonics at the noise level are eliminated. This threshold is different from simulation to simulation, depending on speed. (FEA physical rotation step size is a function of speed).

Analyzing the MMF and its harmonics is of interest since it can cause iron losses. The MMF is calculated analytically with the method fully described in chapter-3. The harmonics are calculated by taking into account the periodicity of the MMF waveform that is the number of symmetries in the winding.

5.2.1.1.1 Core losses at no load condition

Stator and rotor total core losses have been normalized using FEA core loss data for three cases and represented the percent of involvement of different harmonics for the rotor and stator core losses shown in Figure 5.7. From Figure 5.7 it is shown that the

percent of harmonics contribution for rotor and stator are not same. However the percent of harmonics for corresponding core losses are not same for all the cases but the trends are same. It is evident from Figure 5.7 that fundamental, 3rd, 5th and 7th harmonics are liable significantly to increase or decrease the stator core losses and 2.4th, 4.8th, 7.2th and 9.6th are the dominating harmonic rotor core loss at no load condition. However, at higher speed the corresponding harmonics do not maintain exactly same percent but very close. For example, the case1 at 1000 rpm fundamental stator harmonic contributes 90% of the total stator core loss and 3rd and 5th harmonics contribute 3.6% and 3% of stator core loss respectively. Whereas, the case1 at 4000 rpm fundamental stator harmonic contributes 88% of the total stator core loss and 3rd and 5th harmonics contribute 4% and 3.5% of stator core loss respectively. This scenario should be different in loaded condition, as the speed increases and fundamental flux is weakened, the percent of contribution of fundamental core losses decreases and higher harmonic core losses become more significant at loaded condition.

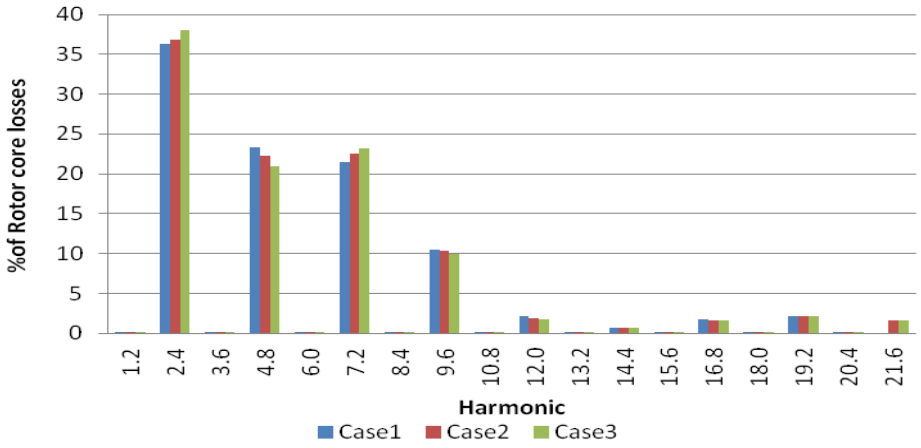

(a)

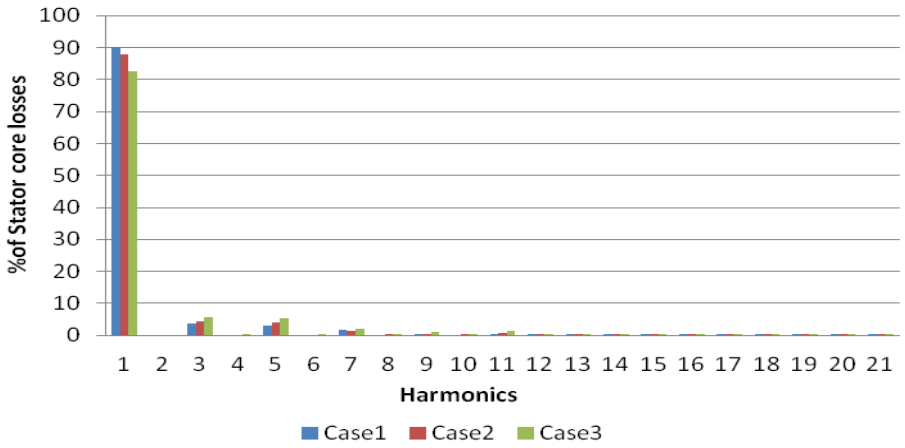

(b)

Figure 5.7 Harmonics contribution of (a) Rotor (b) Stator No load core losses at 1000 rpm

Total core losses increase with the increase of speeds and increment trends are same for all cases at no load condition. For example, case 1 has lowest core losses and case 3 has highest core losses in all speed ranges shown in Figure 5.8. In the loss profile data it can be shown that the contribution of eddy current loss are less compared with hysteresis loss on total core loss at low speed region (low frequency region), but at high speed region the eddy current contributes more than the hysteresis loss mainly due to high frequency effect. It can be seen from simulation results that for different cases the core losses of rotor are relatively small in wide speed range but in case of stator, the core losses as well as eddy current losses change significantly. The core loss of the machine can be elaborately depicted by the analysis of rotor and stator core loss harmonics components separately. Figure 5.9 shows the harmonics components of the rotor and stator core loss at no load condition. Though fundamental as well as 7th stator harmonics core losses are almost same for all the cases at a particular speed, the 3rd and 5th stator harmonics core loses are different and follow the same trend of total core losses for all cases. It is seen that the 3rd and the 5th stator harmonic core losses in case of case 1 is lowest and case 3 is highest among all these three cases at any speeds. On the other hand, 2.4th and 7.2th order rotor core loss harmonics follow the same trend of total core losses

in wide speed ranges whether the 4.8th and 9.6th order rotor harmonics are same at any particular speed for all the cases. From these analysis it is found that the 3rd, 5th stator core loss harmonics and 2.4th, 7.2th rotor core loss harmonics make discrepancy in total core losses for the three cases.

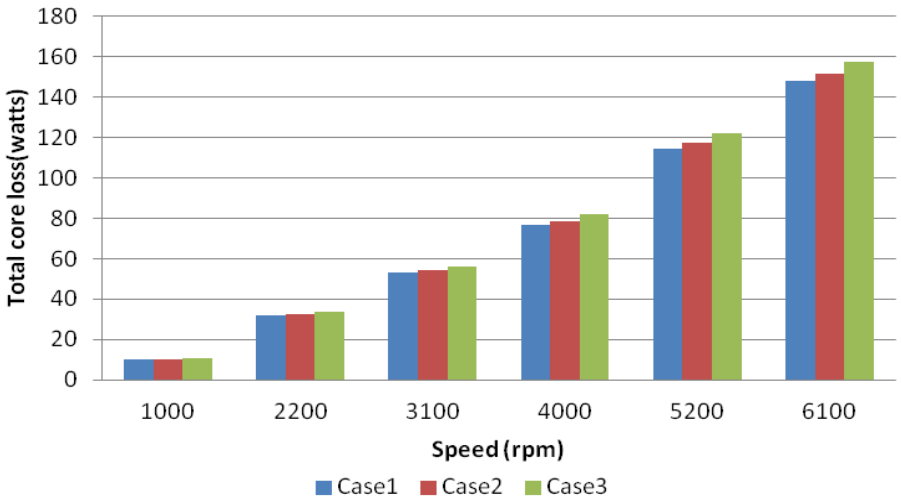

Figure 5.8 Total open circuit core losses over wide speed range

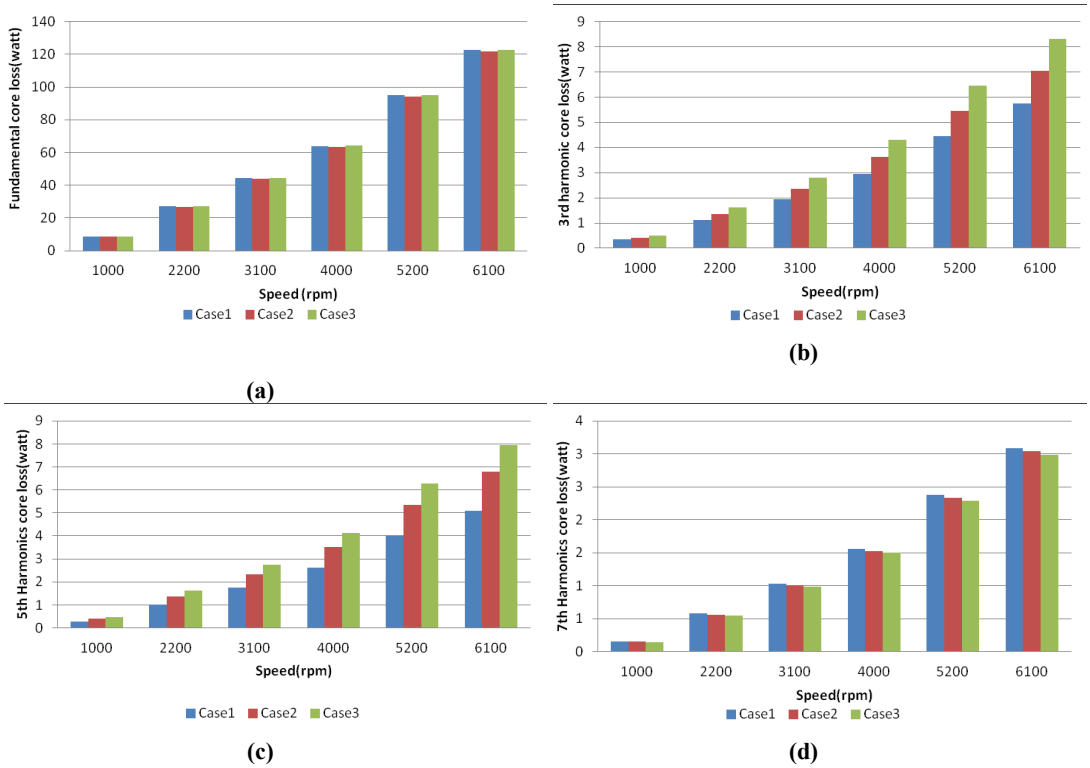

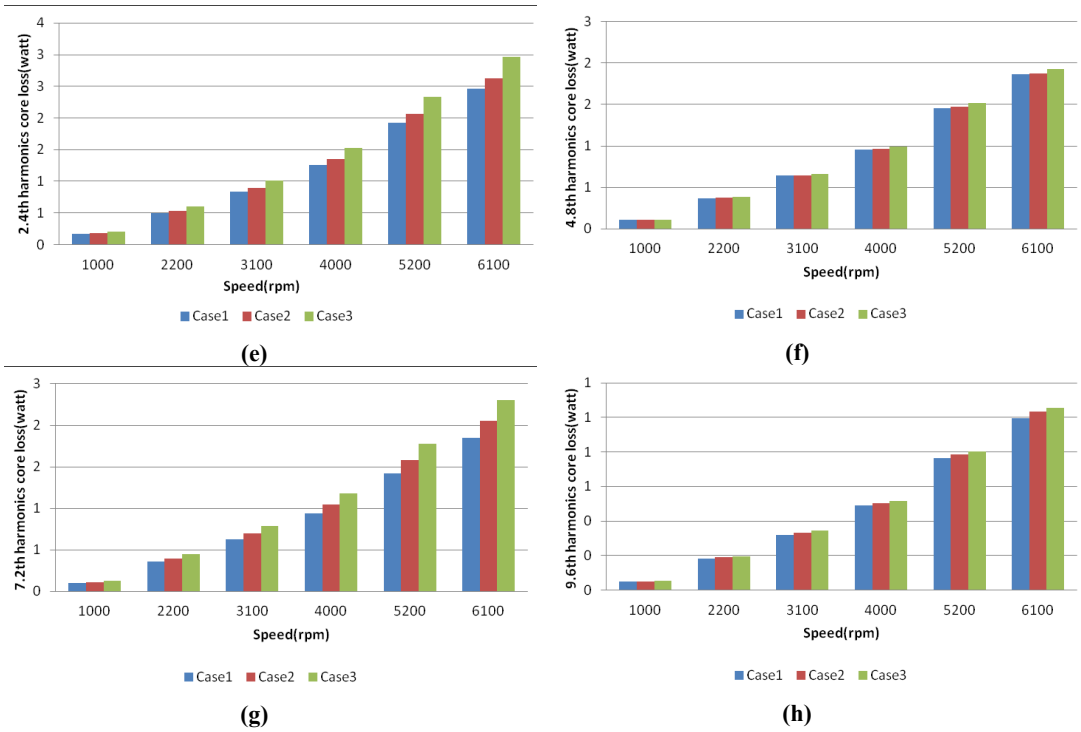

Figure 5.9 Harmonics core loss component of (a-d) Stator and (e-h) Rotor at no load condition

Some factors which influence the core losses are material thickness, cross-sectional area, conductivity, the difference between the alternating core loss and the rotating core loss, flux distortion, flux waveform shape, etc. The three cases have the same material, cross section area conductivity, etc except the magnet bar orientation. So the flux distortion and flux wave shape are factors to increase and decrease the core losses. Another factor to change the air gap flux shape is leakage flux around the end of the magnet. In these three models as the magnet bars alignment has been changed, the leakage flux is changed at the top and bottom of the magnet bar. In Figure 5.10 the magnetic leakage flux for different magnet positions is shown. It can be seen that the leakage changes with magnet bar orientation.

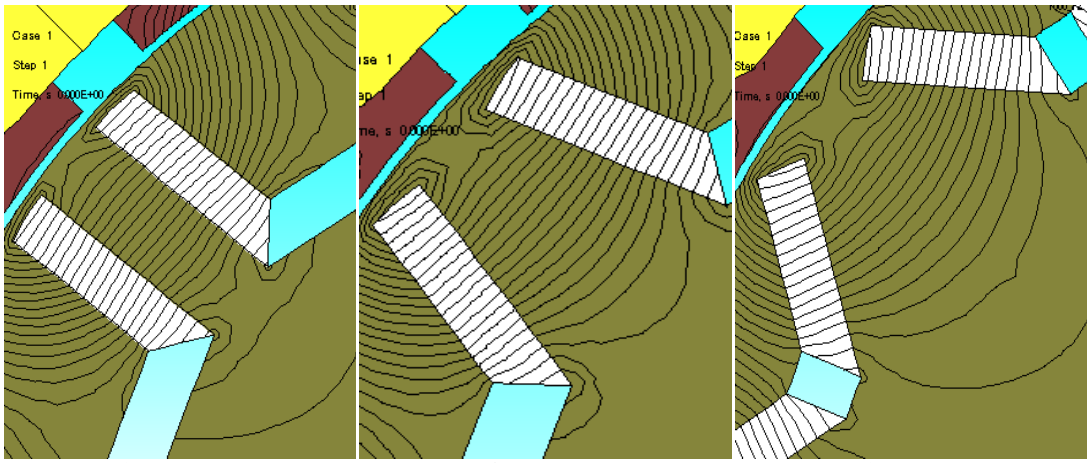

(a) Case 1 (b) Case 2 (C) Case 3

Figure 5.10 Magnetic leakage flux plots

5.2.1.1.2 Core losses at loaded condition

At no load and load condition, total core loss follows the same trends with speed. Figure 5.11 shows the total core loss profile with the speed rated power conditions at loaded condition. The rotor core loss are higher significantly at loaded condition than the no load condition. Total core loss is lower at any specific speed level in flux weakening region at loaded condition than no load condition. It is logical since the flux is weakened in flux weakening region at loaded condition and hence decrease the air gap flux magnitude. However this is not straight forward as the air gap flux shape is changed and introduced harmonics which increase the harmonics loss during field weakening operation. The harmonics core loss of rotor and stator are shown in Figure 5.12 (Harmonics core losses at loaded and open circuit condition of individual machine are shown in Appendix B). The hysteresis loss is more significant at base speed and less significant at high speed region. From Figure 5.12, it is seen that the influence of harmonic core losses increases with speed. This is reasonable since higher frequency losses will be limited significantly by skin depth in the laminations. In general for IPMSM the efficiency is reduced at higher speeds due to the core losses and the

efficiency is affected much by copper losses at the base speed. However from the total core loss profile it is seen that the case-1 has the lowest core losses among all cases.

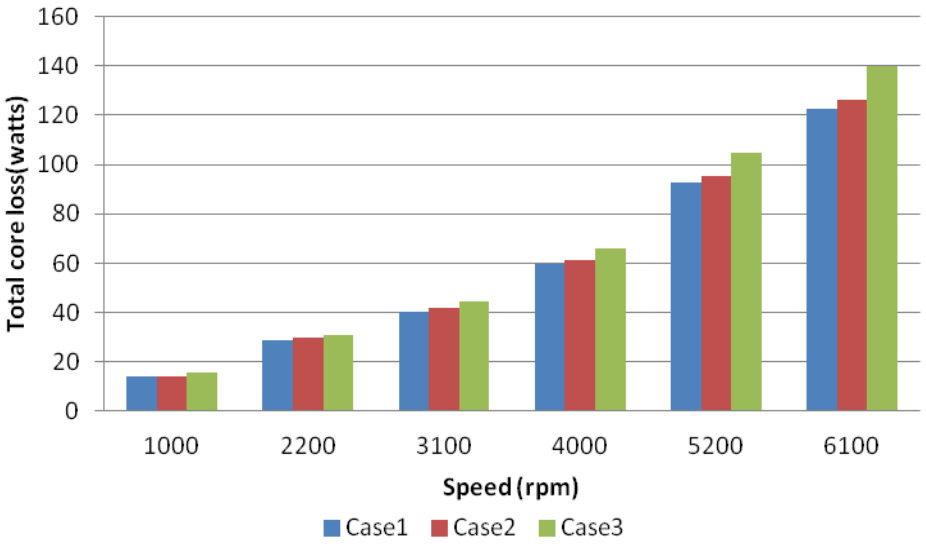

Figure 5.11 Total core losses at loaded condition

The stator core loss is higher compared to rotor core loss for all the cases. Considering fundamental and 3rd harmonic stator core loss at high speed region, case-1 exhibits the lowest core losses and case-3 exhibits the highest core loses. Though the 5th and the 7th harmonic core losses in case of case-2 is lowest among all these three cases particularly at high speed region, the core loss differences for these harmonics numerically vary little and results of case-2 exhibit higher total core losses than case-1. More detailed information about core losses may be acquired by splitting the core losses into two components: hysteresis and eddy current losses. It can be seen that the hysteresis losses are similar for all cases – it is the eddy current loss component that dominates the difference between harmonic losses for the three designs. On the other hand, the rotor harmonics core loss difference for different cases are not significant to make a difference in total core loss as all the cases have nearly equal core loss due to 2.4th harmonics and different rotor core losses at other notable harmonics, which is not a significant value compared with stator core loss differences.

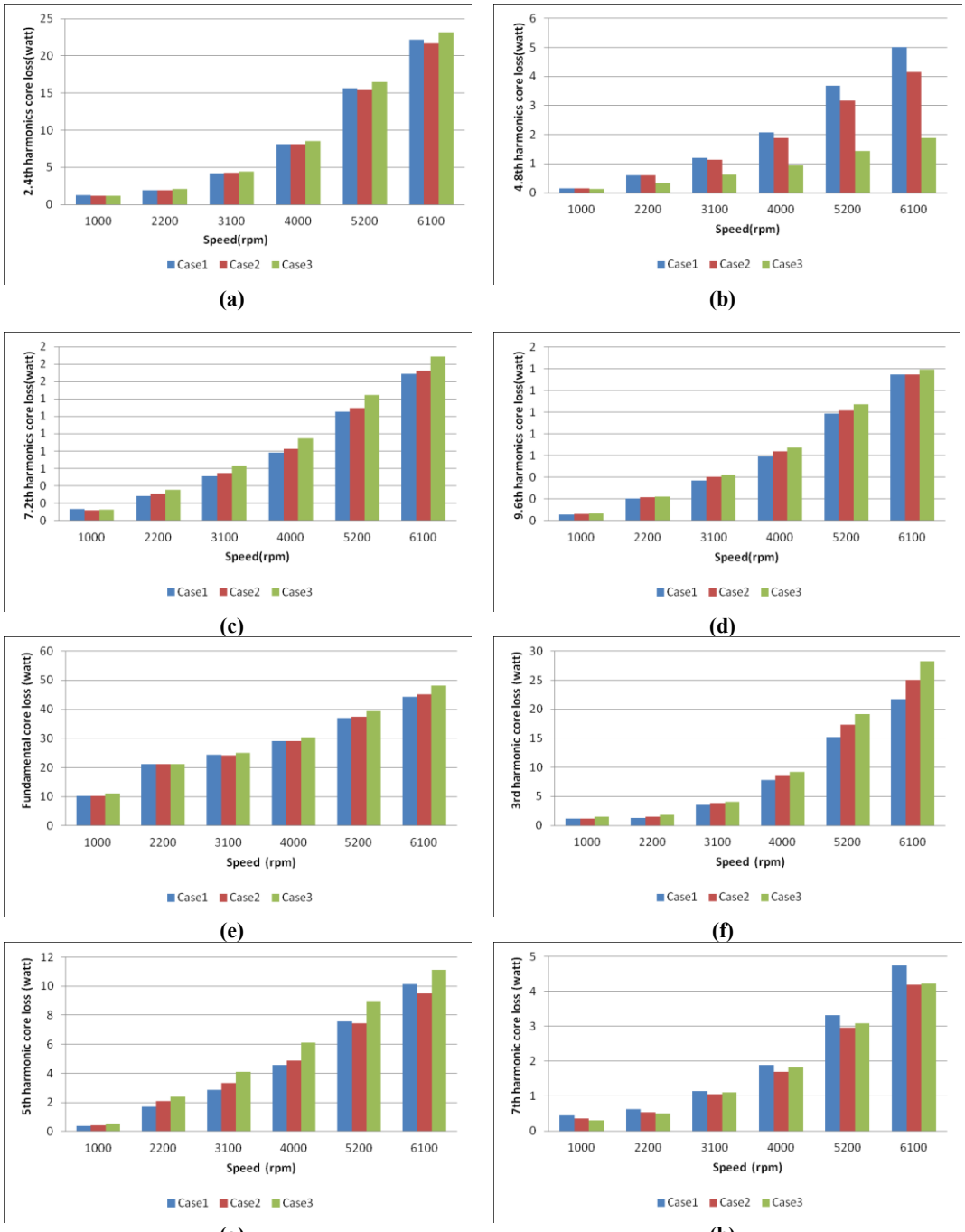

Figure 5.12 Harmonics core loss component of (a-d) Rotor and (e-h) Stator at load condition

Efficiency of the machine depends on different losses such as core losses, copper losses and stray losses. The core loss is calculated by FEM and copper losses are calculated analytically. Based on these two loss components, without considering any other losses, the efficiencies of the three cases have been shown in Figure 5.13. The

efficiency is increased with an increase of speed from base speed to 2200 rpm then decreased with an increase of speeds for all the cases. From analytical calculation of copper loss and FEA of core losses, it is seen that the copper losses are dominating losses in the low speed region and core losses are dominating losses in the high speed region. Howeve, lower efficieny is expected than calculated in real situation for all the cases when the friction and windage losses will be considered.

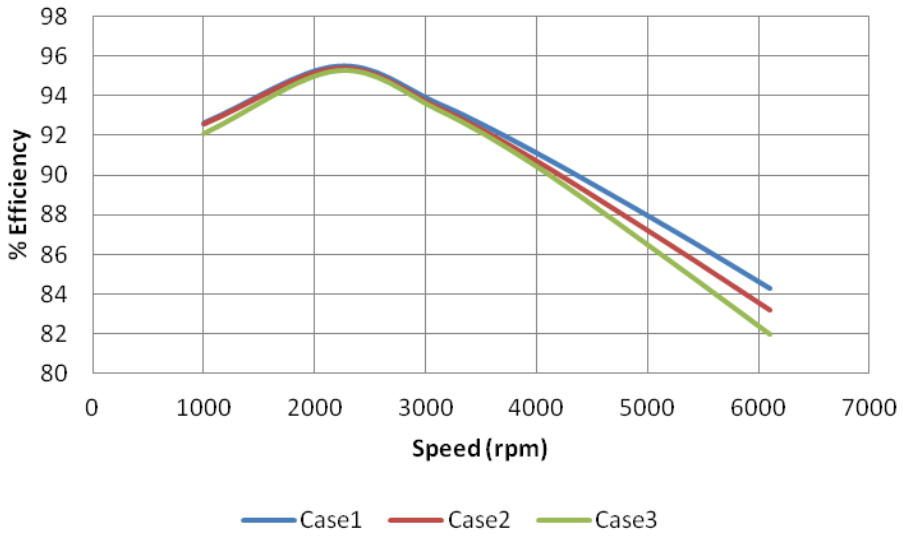

Figure 5.13 Efficiency of all three cases

From the above analysis it is evident that the case1 has the most suitable magnet orientation than all other cases. So, case 1 will be compared with the other machine model having the higher rotor bar magnet with same motor dimension as case1. This analysis is presented in the next section.

5.2.2 Influence of magnet strength

Influence of magnetic strength of magnet bar in the rotor is investigated in this section. For this reason the magnet bar is changed in the rotor of case-1. NEOMAX 42AH magnet is used to increase the magnet strength in the rotor. The main reason of using this magnet is to select an integer number of turns which gives the same flux

linkage as case-1, allowing fair evaluation between cases. 43 turns are used in higher magnet strength IPMSM to get the same flux. As the number of turns is lower, the resistance of winding is lower compared to case-1, which is 0.47 ohm. The open circuit voltage is the same as case-1. Though the magnet strength is increased, the required rms current is the same at base speed to get the rated torque. For the design with stronger magnet, the number of turns is reduced to maintain λpm at a similar value. (Note that λpm values are not identical due to requirement for an integer number of turns.) As a result, *Ld* and *Lq* are reduced. At the base speed, the balance between reluctance and excitation torque is different for the two cases, even though both cases have similar torque per amp. At high speeds when field weakening is required due to terminal voltage limit, additional field weakening current is needed due to reduction in *Ld*. Table 5. 3 gives the comparative required currents of case-1 using NEOMAX 32H and NEOMAX 42AH magnet bar for 1kW output. Note that at all speeds, maximum efficiency occurs with some field weakening current due to addition of the reluctance torque component. Figure 5.14, shows that the I^2R losses for both magnets machines. It is seen from Figure 5.14, that the I^2R losses are almost same in the low speed region but at high speed region the stronger magnet IPMSM gives the higher I^2R losses.

It is seen from the simulation results that at base speed, the q-axis current dominates Joule losses while torque is highest, and the Joule losses are almost equal for both designs. However, at high speed region the torque is lower so the i_q is lower; but higher i_d current is required for field weakening, which is the main component for Joule losses at higher speeds. As the required i_d current is less for weaker magnet, the weaker magnet design offers lowest Joule losses.

TABLE 5. 3 CURRENTS REQUIRED FOR 1KW OUTPUT

Speed (rpm)	Torque (Nm)	NEOMAX 32H (case1)		NEOMAX 42 AH (case1)	
		I_d (A)	I_q (A)	I_d (A)	I_q (A)
1000	9.55	-2.52	8.99	-1.53	9.20
2200	4.34	-3.59	3.46	-4.11	3.48
3100	3.08	-5.61	2.28	-6.80	2.30
4000	2.39	-6.96	1.74	-8.39	1.75
5200	1.84	-8.36	1.31	-10.10	1.32
6100	1.57	-9.21	1.10	-11.19	1.11

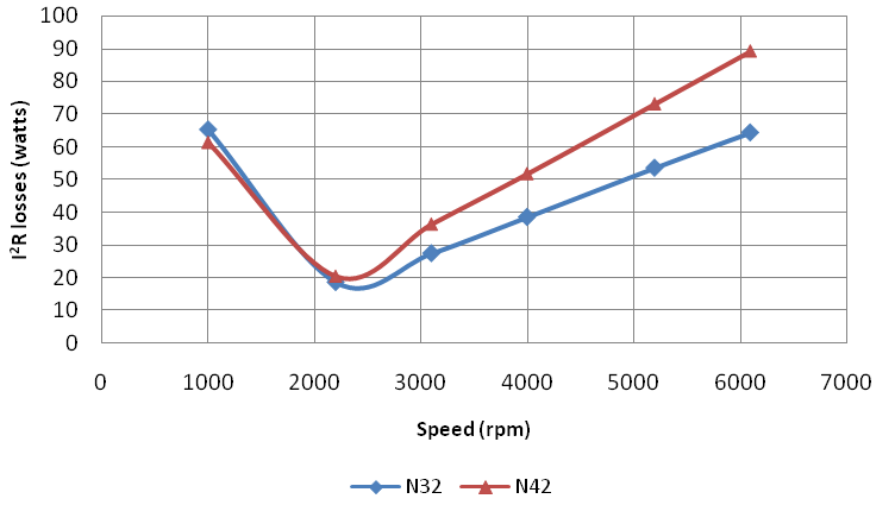

Figure 5.14 Contribution of d-axis and q-axis currents to Joule losses under rated power operation over full speed range for different magnet strengths.

A higher phase inductance will limit the short circuit current of an IPMSM. DQ inductance values for the two magnet cases are shown in Figure 5.15. It is seen from Figure 5.15, that the d axis inductance and q axis inductance of stronger magnet machine are significantly smaller than those of the weaker magnet machine. Moreover, the difference between L_d and L_q is smaller in case of stronger magnet than weaker magnet,

which leads to a lower reluctance torque per amp; which in turn in more I^2R losses. The lower phase inductance of stronger magnet machine exhibits lower capacity to limit the short circuit current than the weaker magnet machine.

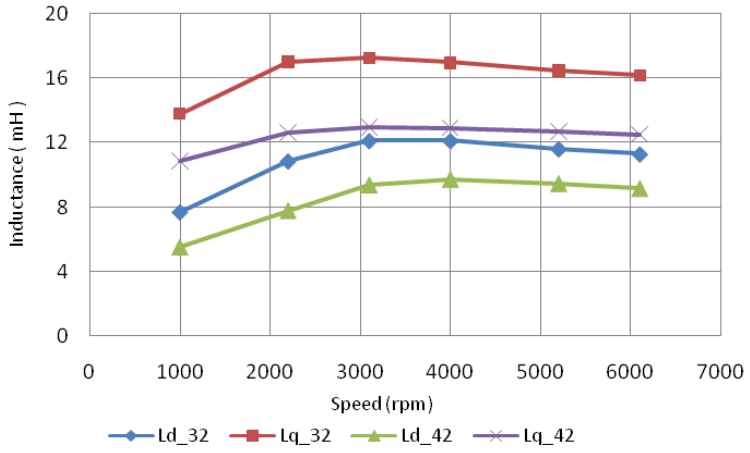

Figure 5.15 DQ inductances of lower and higher magnetic strength models

The different component of core losses for weaker magnet (N32H) motor and stronger magnet (N42AH) at loaded condition are shown in Figure 5.16. It can be seen from the figure that the rotor and stator core loss components for weaker magnet motor are lower compared with corresponding harmonics of the stronger magnet machine. However, the increase rate of fundamental stator core losses is lower at base speed and higher at high speed region in case of higher magnet machine. For example, at 1000rpm 6.7% higher and at 6100rpm 18% higher the fundamental stator core loss of stronger magnet machine. Stronger magnet machine gives significant amount higher core losses and higher I^2R losses at high speed region. So, it is evident the efficiency level of stronger magnet machine is lower at high speed region shown in Figure 5.17.

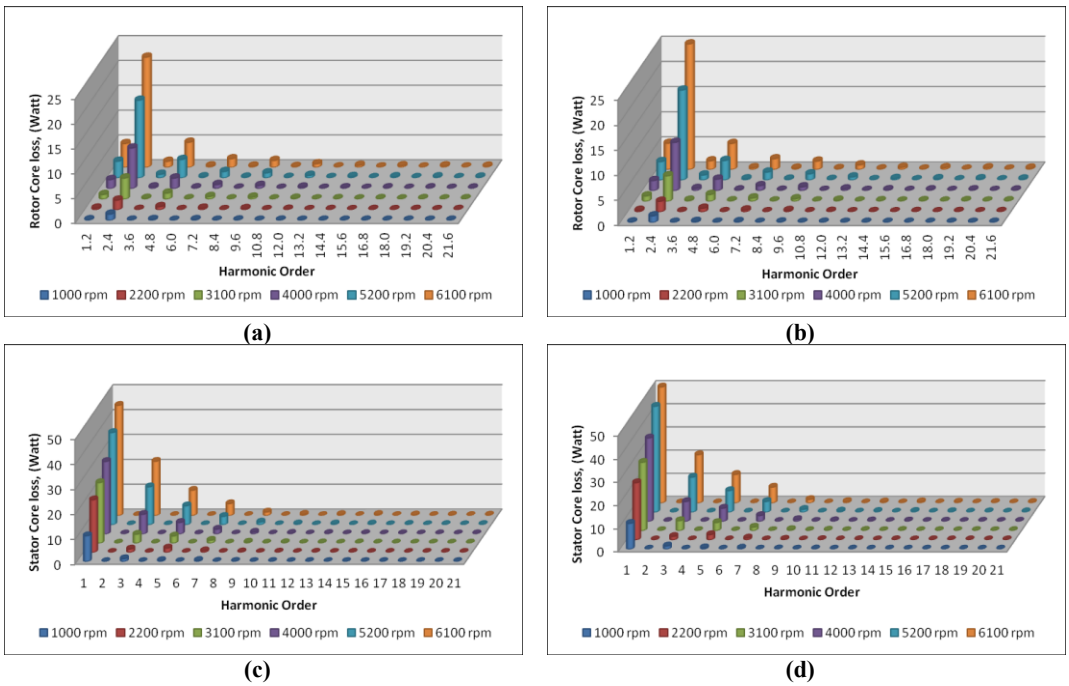

Figure 5.16 Core loss harmonic component for (a) weaker magnet machine rotor (b) stronger magnet machine rotor (c) weaker magnet machine stator(d) Stronger magnet machine stator

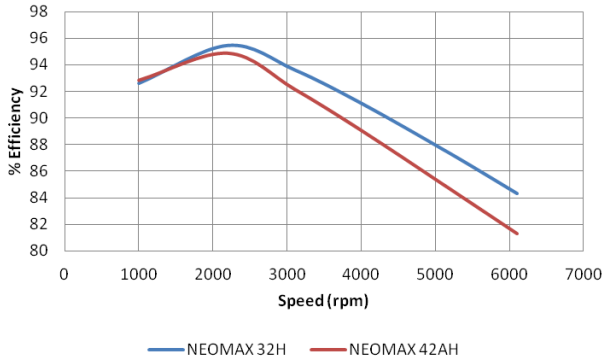

Figure 5.17 Efficiency of higher and lower strength rotor magnet IPMSM

The increased core losses by the flux weakening current are mainly due to the eddy current loss in the core. It has been shown that Case-1 is much more effective than other cases for reducing the harmonic core losses in the stator under flux weakening operating conditions. For wide speed range operation, magnet strength may be chosen based on the balance required between low speed and high speed efficiency. If low-speed high torque is the controlling factor, then obviously higher strength magnets offers an advantage for winding losses and resulting heat and cooling requirements. If high speed efficiency is more important, then the design may be modified to reduce the magnet requirements.

5.3 Stress Analysis

The stress and the displacement of the rotor increase with the increase of speed due to centrifugal force. Strong centrifugal force developed at high speed operation is not uniform throughout the entire volume of the rotor because centrifugal force is concentrated normally in thinner area of the rotor core and centrifugal force also acts on the magnet. Some thinner area may be better in design viewpoint for electromagnetic performance. Moreover, the magnet has a weaker intensity than the core materials. This force can cause of deviation and dislocation of the magnet from its original position. So, mechanical displacement and stress evaluation are required at motor highest operating speed in the design stage before the motor is built. The contour plot of stress and the displacement of the rotor at the maximum speed (6100rpm) are shown in Figure 5.18. The figure shows that the maximum stress on the rotor is 5.9434 MPa at the bottom of the air pocket. However the maximum displacement happens at the surface of the rotor which is 0.000495 mm. As the air gap of the machine is 0.5 mm and the displacement is of the rotor is allowable due to very small rotor deformed at maximum speed, the machine is expected to work properly without permanent damage at all motor speeds.

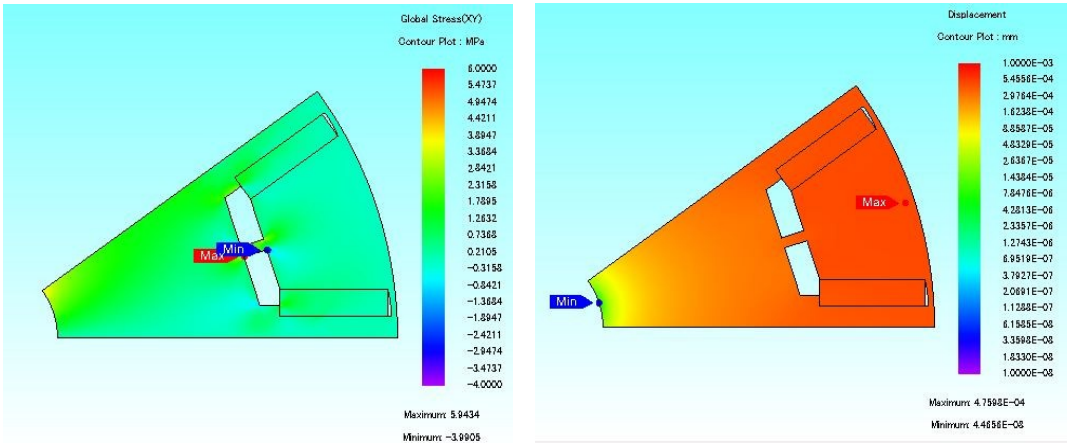

(a) **(b)**

Figure 5.18 Contour plot of (a) stress on the rotor (b) displacement of the rotor

It is found from the entire above finite element analysis that the case-1 with higher magnet angle orientation and lower magnet strength gives the best performance among all the cases. However, from the design viewpoint some rotor geometry modification is needed in order to increase the strength structurally. Some bridge is placed in the air pocket to make the rotor mechanically strong. The stress on the rotor and displacement of the rotor structure is satisfactory in terms of motor operation without displacing the magnet and rotor core permanently at all desired speed level.

Chapter 6

Influence of Steel BH Characteristics on IPMSM Performance

The core loss of the IPMSM is affected by the magnetic properties of the core materials. The magnetic properties of the core materials such as BH curve, permeability, DC magnetization curve depend upon using the different core materials. However, the magnetic properties could vary even for using same core material differently treated such as stress relief annealing (SRA), heat treated, punching, welding. SRA is done in order to reduce residual stresses which are the result of thermal cycling. Internal stress of a metal exists in welding parts, cold-formed parts. Heat treatment of metal is not only done to increase the strength of material, but also to modify certain manufacturability goals such as getting better formability, improved machining, restored ductility after a cold working operation. These processes adjust the mechanical behavior of the core material in an advantageous manner to maximize service life. However, the properties of the core material are also changed during these treatment processing[6]. However, it is common to apply a stress relief anneal (SRA) after motor assembly to help minimize some of the unwanted effects of the manufacturing process. In this chapter two categories JFE steel having different BH characteristics and core loss data used in FE machine model have been presented. These JFE steel categories are 1) JFE SRA, Non-SRA, Manufacturer steel data 2) JFE Heat treated and non-Heat treated steel.

6.1 Effect of SRA on motor performance

In this section, the influence of manufacturing process on electrical steels magnetic properties is investigated in order to predict IPMSM performance. Hence, three sets of JFE steel characteristics are used to compare the performance: the steel manufacturer's data (basic data) (Shown in Appendix A)and two sets of data obtained from Epstein frame tests. These two sets are for SRA and non-SRA Epstein steel samples. The study

results using manufacturer's material (MM) properties are compared to results obtained by using material data obtained by experimental test after manufacturing process as described in chapter 4 (case1). The simulations of the IPMSM with different tested lamination data are conducted with all the parameters and dimensions of the machine held constant, except the magnetic properties of the lamination materials.

Under open circuit conditions, the magnetic flux linking (λ_{pm}) each phase of the machine used manufacturer steel data is predicted by the FEM to be 143 mWb -turns. A plot of the magnetic flux density variation at the base speed in the core is presented Figure 6.1, for MM machine. It can be seen from Figure 6.1 that the flux density in the teeth is typically below 1.5T while the back iron flux density is less than 1.0T. The majority of the cross section of the machine is operating under saturation region. However, the main flux paths are saturated.

Plots of magnetic flux density for operating conditions identical to those for Figure 6.1, are presented in Figure 6.2 for the case with the measured properties of the SRA laminations and Figure 6.3 for the measured properties of the non-SRA laminations. All three plots use the same contour scale. At first glance, the flux density plots for all three cases are similar. However, on closer inspection it can be seen that the peak flux density Figure 6.2 and Figure 6.3 are slightly lower than that in Figure 6.1 for the manufacturer steel data. In addition, localized variations of flux density can be observed: in both cases using measured characteristics the flux density in the most saturated teeth is lower than the manufacturer steel data case while the flux density in the least saturated teeth is higher manufacturer steel data case.

Considering the open circuit permanent magnet flux linking the coils, the peak phase flux linkages obtained when simulating using the tested lamination data are slightly different, which are λ_{pm} =142 mWb-turns for SRA and λ_{pm} =141 mWb-turns for

non_SRA. This compares to the value of λ_{pm} =143 mWb-turns obtained with the lamination manufacturers data. Hence the open circuit voltages of the SRA and non-SRA and manufacturer data simulations are almost same.

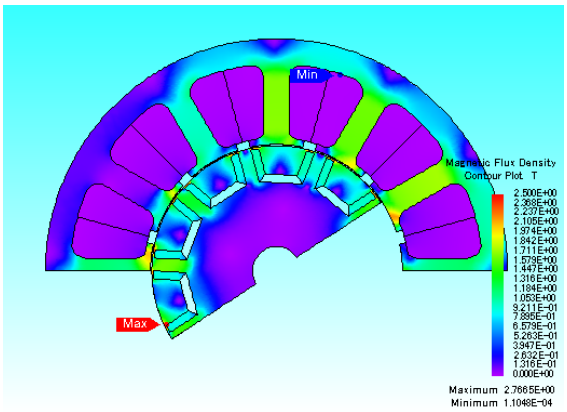

Figure 6.1 Contour plot of magnetic flux density of the investigated model

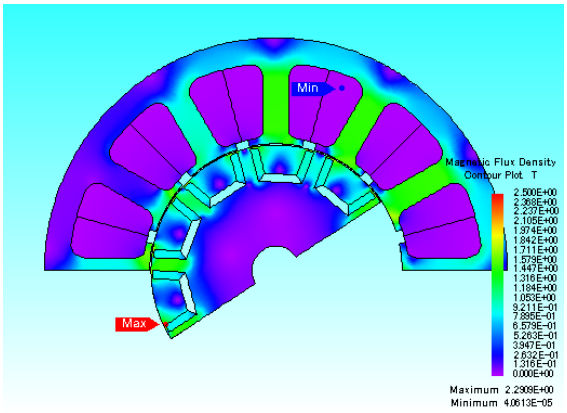

Figure 6.2 Contour plot of Magnetic flux density of the SRA model

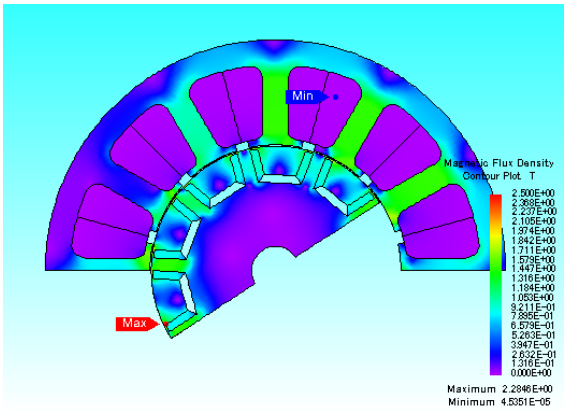

Figure 6.3 Contour plot of magnetic flux density of the non-SRA model

In general, the IPMSM exploits saliency due to different L_d and L_q inductances. Both *dq* current and flux related to the rated voltage effect on the *dq* inductances' values. However, this *dq* current is set to produce maximum torque per amp of a machine in the field weakening region at a certain speed. The *d* and *q* inductances of the investigated model are shown in Figure 6.4 and Figure 6.5, respectively. The study using the tested material properties predict that the L_q are significantly lower than the predictions using manufacturers lamination data. Whereas the L_d inductances are almost equal until mid speed level and lower at high speed level.The difference between inductances is reduced, indicating a reduction in available reluctance torque. In addition, the d-axis inductance is seen to be highly saturation dependent as the q-axis current is reduced and negative d-axis current increased with increasing speed.

Eventually, it can be seen from the L_d and L_q map of investigated SRA and non-SRA model that L_d and L_q are almost identical at any specicific current and its specific angle. The maps also shows that the model using manufacturer data exhibits different L_d and L_q than the other two investigated models at any specicific current and its specific angle. However, the different controlling current based on any particular operating speeds affect on the *dq* inductance values; the inductance values of SRA and non-SRA are lower compared with manufacturer data. The L_d and L_q inductances varies from 7.7mH to 11.2 mH and 13.7 mH to 16.19 mH respectively for manufacturer material; While for SRA corresponding inductance varies from 7.0mH to 10.6 mH and 12.7 mH to 14.2 mH and for non-SRA corresponding inductance varies from 6.6mH to 10.5 mH and 12.49 mH to 14.03 mH. It is figured out from all the *dq* inductances values that the manufacturer's data give the higher saliency ratio.

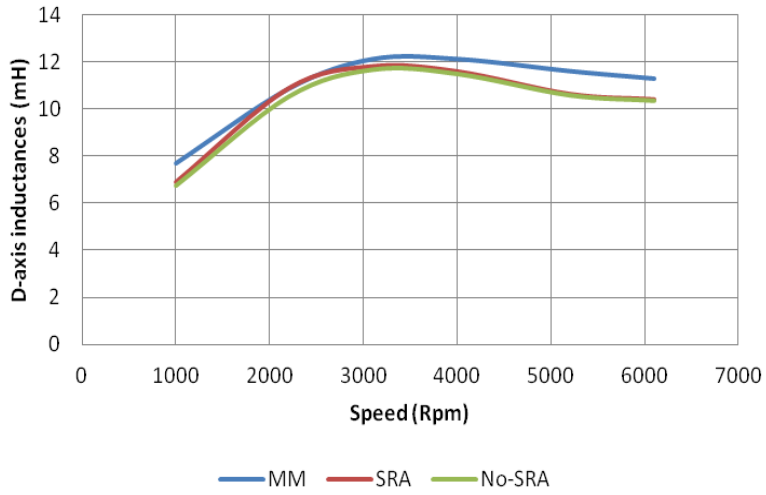

Figure 6.4 d-axis inductance of IPMSM at different speeds using the three magnetization characteristics

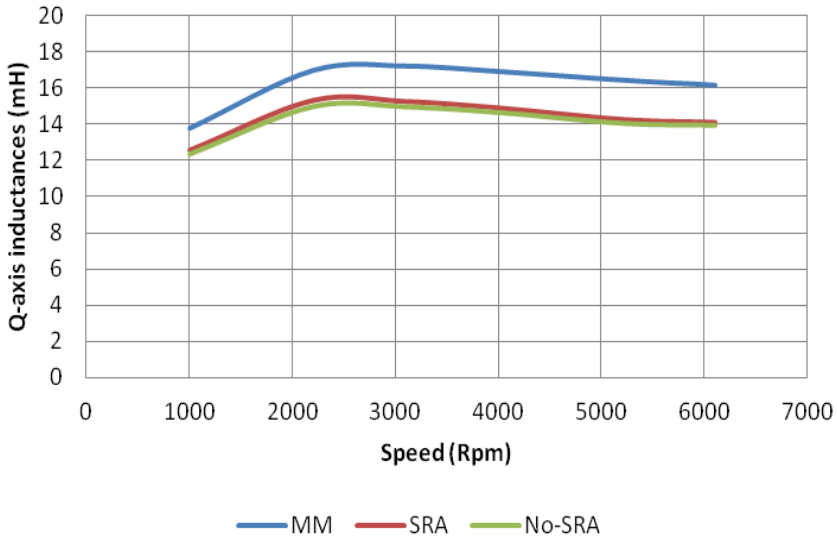

Figure 6.5 q-axis inductance of IPMSM at different speeds using the three magnetization characteristics

The preceding analysis indicates that the SRA and non-SRA test data result in predictions of inductance that are lower than predicted using the lamination manufacturer's data. The reluctance torque is established due to the rotor anisotropy [146]. The saliency ratio reduced in case of SRA and non-SRA models which are 6-36% less than the manufacturer data. As a result, there is an expectation that the controlling current will be higher to meet the same rated torque and constant power. The controlling

currents for the different models are shown in Table 6. 1 These different controlling currents make result in different predicted copper losses for each. Figure 6.6 plots the copper loss prediction, together with simulations using the measured steel characteristics. The copper loss is almost the same in all speeds except for high speed region for all the cases and this is mainly due to the different flux weakening currents. Using SRA data, copper loss is increased 14% at 6100 rpm, whereas for non-SRA machine copper loss is increased 11% at 6100 rpm. These increased copper losses obviously affect the efficiency of the machines.

TABLE 6. 1 CONTROLLING CURRENTS

Speed (rpm)	Manufacturer data		SRA		non-SRA	
	I_d (Amp)	I_q (Amp)	I_d (Amp)	I_q (Amp)	I_d (Amp)	I_q (Amp)
1000	-2.52	8.99	-2.52	9.20	-2.52	9.27
2200	-3.60	3.46	-3.80	3.51	-3.72	3.54
3100	-5.61	2.28	-5.58	2.39	-5.53	2.42
4000	-6.96	1.74	-7.18	1.84	-7.11	1.86
5200	-8.36	1.31	-8.99	1.39	-8.91	1.40
6100	-9.21	1.10	-9.86	1.17	-9.74	1.19

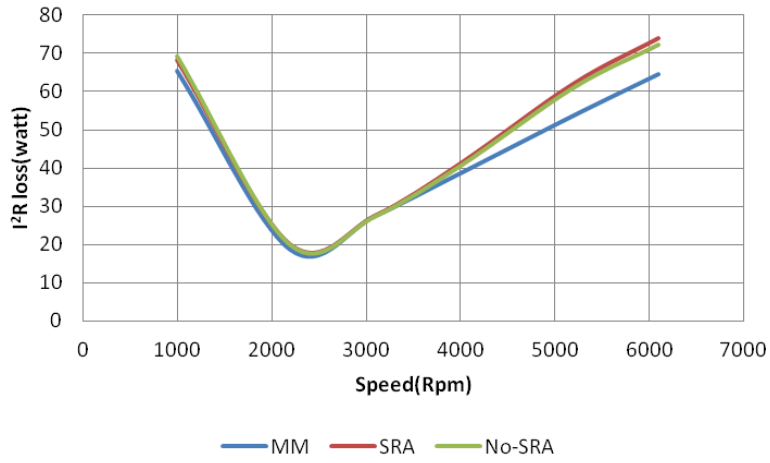

Figure 6.6 Copper loss curve of the investigated study cases in field weakening

6.1.1 Core loss

The harmonics core loss component of rotor for using manufacturer data, SRA and non-SRA are shown in Figure 6.7, Figure 6.8 and Figure 6.9. It is seen that the 2.4th order harmonics standing to represent the highest rotor core loss component at any specific speed. However, the Non-SRA rotor core loss is more closer to the core loss using manufacture data and the lowest core loss occur in SRA motor model.

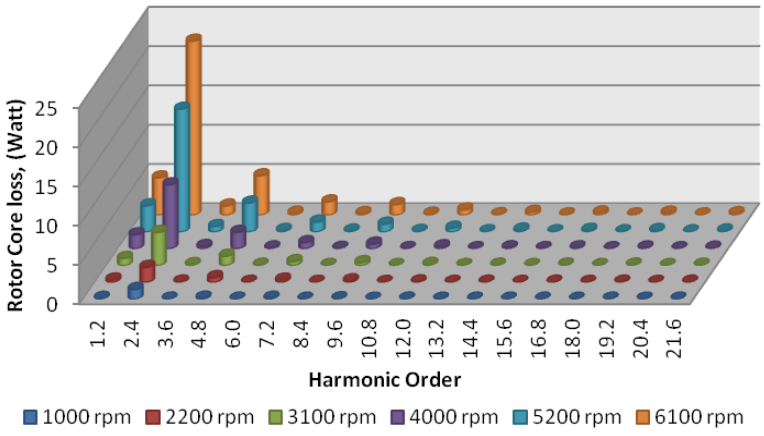

Figure 6.7 Core loss component of the rotor using manufacturer data

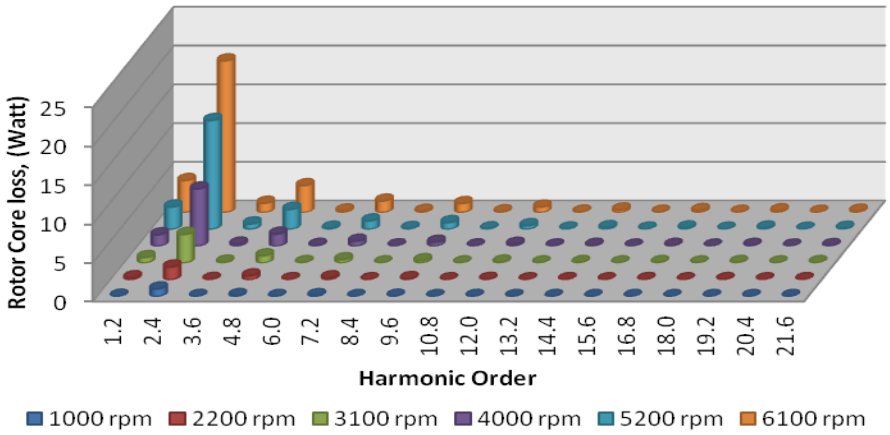

Figure 6.8 Core loss component of the rotor using SRA core materials

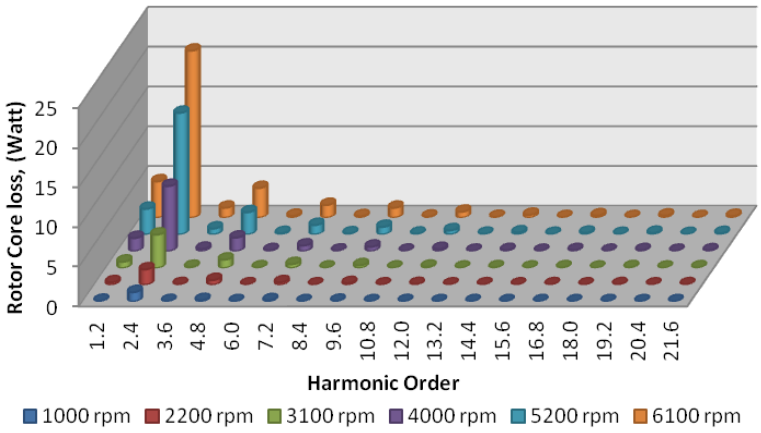

Figure 6.9 Core loss component of the rotor using non- SRA core materials

It is found from core loss data that 1st 3rd, 5th and 7th harmonics core losses are dominating in stator core loss. The stator core loss components using manufacturer data, SRA and Non-SRA are shown in Figure 6.10, Figure 6.11, and Figure 6.12. The stator core loss of Non-SRA core materials is very close to core loss of the stator using manufacturer data. However, 1st, 3rd, 5th and 7th harmonic core loss increase at the high speed region.

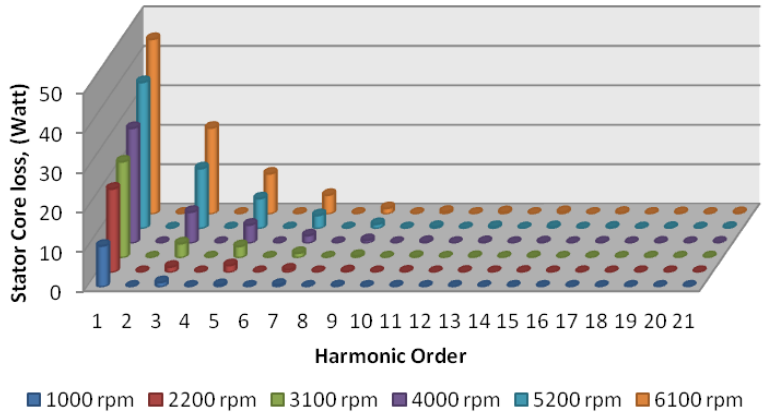

Figure 6.10 Core loss component of the stator using manufacturer data

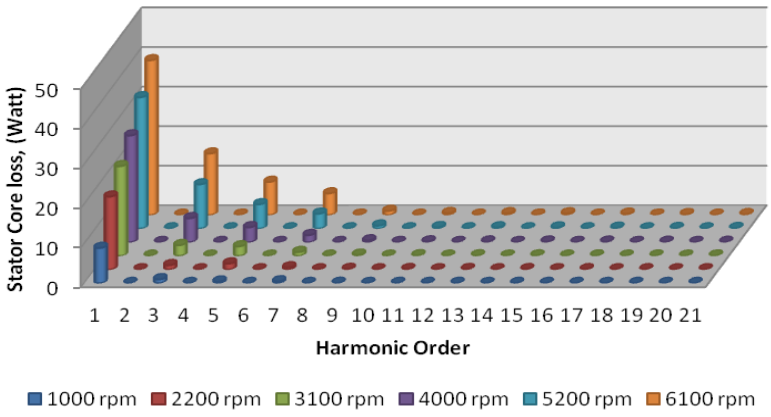

Figure 6.11 Core loss component of the stator using SRA core materials

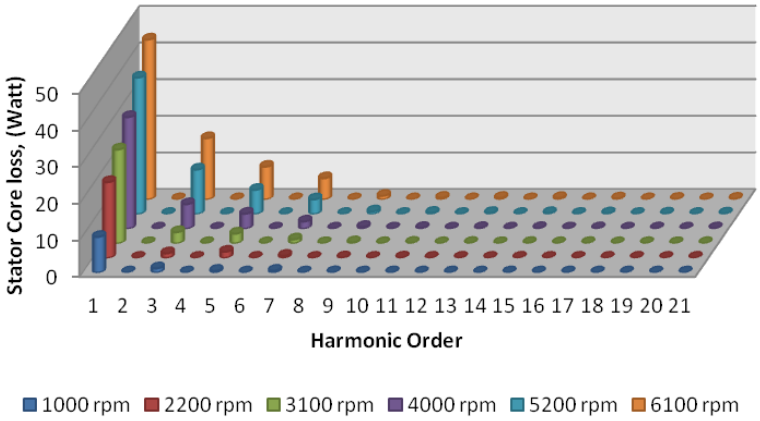

Figure 6.12 Core loss component of the stator using non-SRA core materials

It can be seen from the simulation results that in the same core materials, at no-loaded condition the hysteresis loss component, eddy current loss component and hence the total core loss harmonic components excepts the fundamental are lower compared with corresponding component under loaded condition.

The comparison of the impact of material characteristics is the consideration of predicted total core losses. Figure 6.13 shows total predicted core loss in wide speed range under loaded condition for using manufacturer data, SRA and non-SRA core materials. It is seen that predicted losses are lower for both SRA and Non-SRA cases than the model using manufacturer data. In addition, the SRA test data indicates a reduction in total core losses when compared to the non-SRA case. At high speed region, where the core loss is dominating compared with copper loss, the SRA gives 15% less core loss and Non-SRA gives 7.72% less core loss than the motor model using manufacturer's data. Though the SRA and non-SRA core materials have the lower core losses especially at high speed region compared with the model which used manufacturer data, the trend of copper loss is opposite. Results, efficiency improvements are compromised.

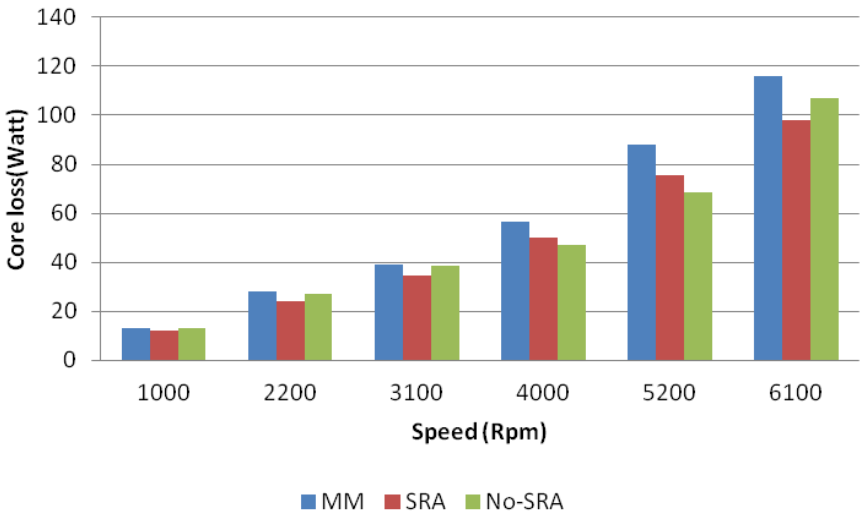

Figure 6.13 Total core losses of the investigated IPMSM models

6.1.2 Efficiency Maps

Efficiency maps of the entire investigated model have been derived in order to predict the energy consumption. In the efficiency map, the optimum current phase angle and amplitude are used to maximize the efficiency at every operation point [146]. The efficiency maps for the investigated model using manufacturer data, test data of SRA and Non-SRA core materials are shown in Figure 6.14, Figure 6.15 and Figure 6.16 respectively. The torque profile is common for all the cases and it is 9.55 Nm at base speed and changed with increase of speed to maintain the constant output power. However, upper profile of the maps exists due to the overload current. From the efficiency maps it is evident that the efficiency decreases at the high speed region mainly due to the harmonics core losses. The difference in efficiency level at any particular speed and torque can be easily predicted by plotting an efficiency discrepancy contour map shown in Figure 6.17- Figure 6.19. The investigated model using test data of Non-SRA core material has the higher efficiency level compared with manufacture data at all torques and speeds above the base speed. On the other hand the SRA core material has the higher efficiency level compared with the model using manufacturer data at all speed level and torque level except at very low speed and high torque level. The contour map of Figure 6.19 gives evidence that the model using test data of SRA core material provides higher efficiency compared with test data of Non-SRA core materials. However, the efficiency discrepancy level among all the cases is within ±6.8%.

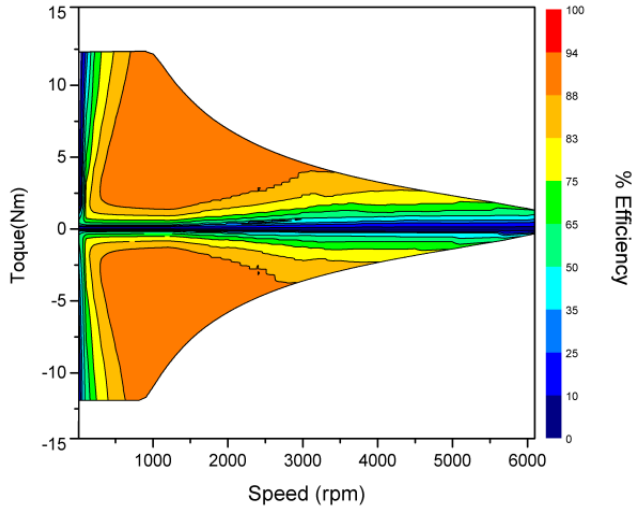

Figure 6.14 Efficiency map of the investigated model using manufacturer data

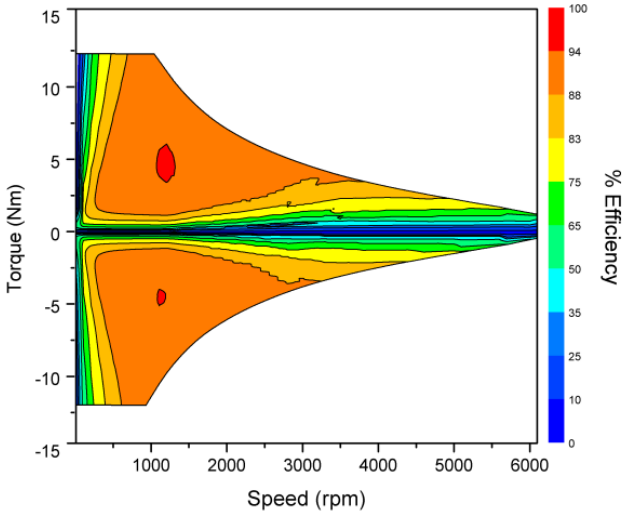

Figure 6.15 Efficiency map of the investigated model using test data of SRA core materials

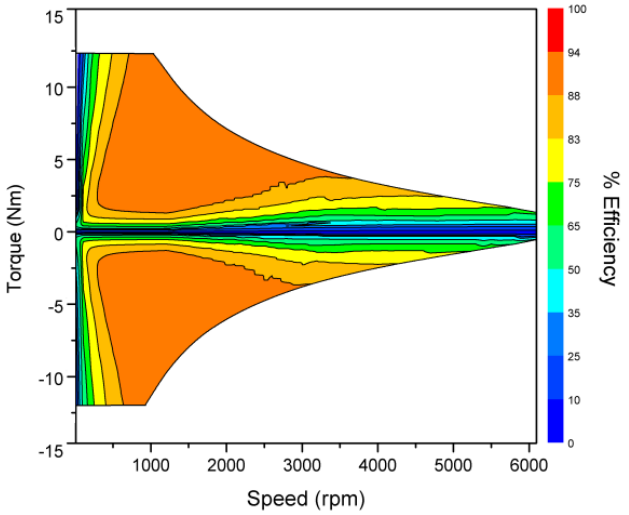

Figure 6.16 Efficiency map of the investigated model using test data of Non-SRA core materials

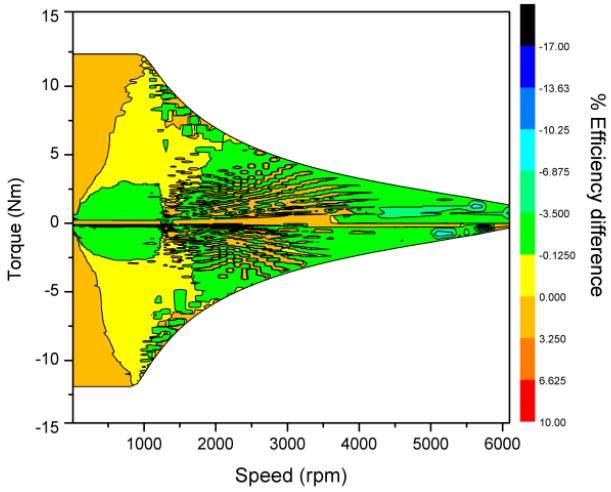

Figure 6.17 Comparative efficiency map-negative efficiency level indicating the higher efficiency level of the investigated model using test data of non-SRA core materials than manufacturer data

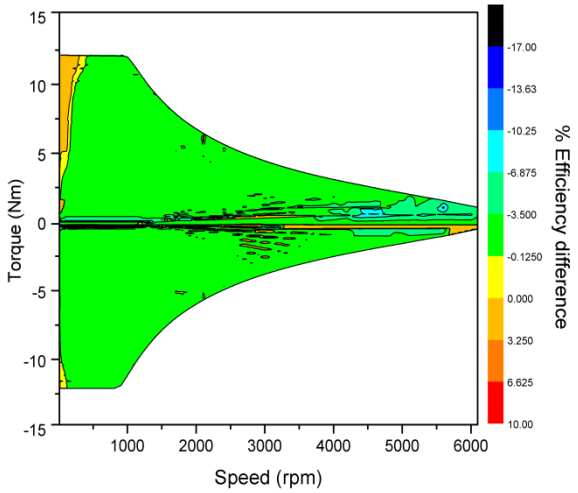

Figure 6.18 comparative efficiency -negative efficiency level indicating the higher efficiency level of the investigated model using test data of SRA core materials than manufacturer data

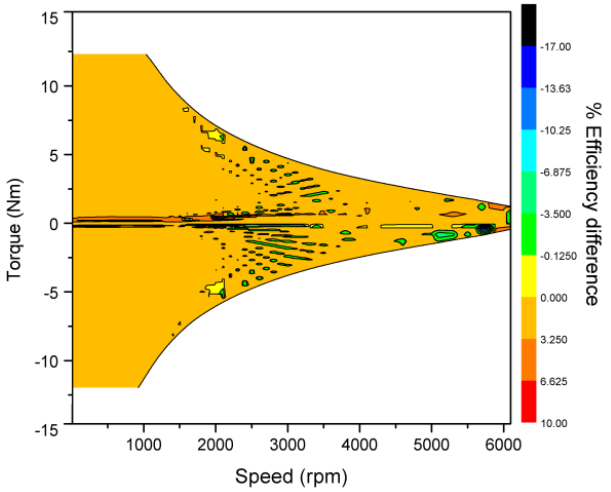

Figure 6.19 comparative efficiency map-positive efficiency level indicating the higher efficiency level of the investigated model using test data of SRA than non-SRA core materials

Corresponding Epstein test data demonstrate on chapter-4 indicates that the SRA process will improve permeability and reduce core loss. However, when the data is transferred to a finite element model of a concentrated winding IPMSM, there is little difference between the SRA and non-SRA results. In both cases, the permanent magnet flux linkage is slightly lower than the prediction using manufacturer's data and the saliency ratio is also lower than when using the manufacturer's data. The influence of SRA is most clearly seen when considering core loss. The measured core loss density from the Epstein tests is lower after SRA, resulting in lower iron loss predictions in the machine model. In this Chapter, the variation in performance due to changes in lamination properties under same rated power output was presented. As the saliency ratio is lower in case of SRA and Non-SRA, an increased field weakening currents are used in order to meet the output torque, resulting in an increase in winding copper losses and limit the efficiency. The model using test data of SRA core material provides highest efficiency among all the investigated models. However the predicted efficiency discrepancy level among all the cases is within ±6.8%.

6.2 Impact of Heat Treatment on motor performance

In this section, the effect of different heat treated core materials on performance of the IPMSM model is investigated. Three different heat treatment cores are selected for the investigation. All three material samples are nominally the same grade of steel and have been stress relief annealed (SRA). One of the samples has no heat treatment, one is subjected to T61 heat treatment and one is subjected to T5 heat treatment is investigated that the heat treatment core of a machine reduced the core losses. A finite element model for a three phase fractional slot IPMSM capable of operating in wide speed is developed and simulations are carried out using three different sets of material properties that have been obtained using standardized Epstein tests.

The required controlling currents for optimization are the same at any particular speed for the IPMSM model used for different heat treated core materials. As the controlling currents are the similar for all sample core materials, the torque per amp figures are similar at any particular speeds and torque per ampere becomes lower with the increase of speeds. Moreover, the magnetic fluxes of the FEM coil for using different heat treated materials are almost same and the value are135.1mwb, 135.5 mwb and 135.6 mwb for T61, T5 and without heat treated materials, respectively. Hence, the open circuit voltages of the IPMSM model are almost same at any particular speed, which are directly proportional to the speeds and the voltage variation of different samples within 0.7%. Whereas the error of the output power are within 0.9%, used same controlling currents. The insignificant error of open circuit voltage and output power depicts that the different heat treated materials do not affect the voltage, power as well as torque variation. Table 6. **2** shows the open circuit voltage, output power in wide speed range of the IPMSM model using different heat treated core materials.

TABLE 6. 2 OUTPUT POWER AND OPEN CIRCUIT VOLTAGE OF IPMSM FOR DIFFERENT HEAT TREATED CORE MATERIALS

Speed, rpm	T61, SRA samples		T5, SRA samples		No-HT, SRA samples	
	Power, watts	Open circuit voltage, V	Power, watts	Open circuit voltage, V	Power, watts	Open circuit voltage, V
1000	999	50.89	1002	51.16	1003	51.27
2200	997	111.96	1003	112.56	1004	112.79
3100	995	157.76	999	158.61	999	158.94
4000	995	203.56	996	204.66	997	205.07
5200	1004	264.63	1009	266.05	1005	266.60
6100	1007	310.43	1007	312.11	1007	312.75

Table 6. **3** shows the controlling current; joule loss and torque per amp at different speeds of IPMSM using different heat treated core material. As the IPMSM model uses the same number of winding turns with different heat treated core materials and the controlling current are same at any specific speed; the copper losses are the same at any specific speed for all the different heat treated core materials. It can be seen that at low speed, when torque is highest, the high q-axis current dominates joule losses. However this scenario is the same for different heat treated materials. To effectively use the reluctance torque along the magnet torque, flux weakening current is used at the base speed. Moreover, the reluctance torque can be increased by increasing the saliency ratio. However, the controlling current used for optimization, gives the significant saliency ratio for the entire investigated model using different heat treated core materials. Wide speed operation of IPMSM is limited by the high back emf and low d-axis inductance. It is found from inductance data of simulated model that *d* axis inductance for T5 heat treated and the core material that has not been heat treated are exactly same. However, the T61 model gives a higher d-axis inductance at lowest speed but not significant different values from other two core materials. It can be also seen that the q-axis inductances are same for all the samples. Hence, the saliency ratios are not affected due to use different heat treated core material in an IPMSM. However, the model gives the highest saliency ratio at the base speed and lowest at the middle speed region.

TABLE 6. 3 I^2R LOSS, CONTROLLING CURRENT AND TORQUE PER AMPERE

Speed (rpm)	$\mathbf{I_d}$ (Amps)	I_q (Amps)	I_{rms} (Amps)	I^2R loss (watt)	Tor/Amp
1000	-3.15	9.30	6.94	72.29	0.97
2200	-3.65	3.72	3.69	20.38	0.83
3100	-5.45	2.54	4.25	27.13	0.51
4000	-7.08	1.96	5.19	40.46	0.32

5200	-9.01	1.51	6.46	62.63	0.20
6100	-9.96	1.29	7.10	75.66	0.16

6.2.1 Core losses

From the simulation result, the most of the core loss takes place due to the core loss in the stator. The rate of increase of eddy current loss with the increase of speed is higher than hysteresis loss. The eddy current losses are higher at all speed except base speed compare with hysteresis loss for different heat treated core materials. However, at the high speed region the eddy current loss and hence, the core loss are lower for the core materials that has not been heat treated compare with heat treated core materials. Figure 6.20 shows the core loss of IPMSM model for different heat treated core material. From the figure it is evident that the core material which has not been heat treated gives the lowest core losses at all speed. However, it is found from the core losses harmonics component extracted from simulation that IPMSM having the core material that has not been heat treated gives the lower core loss components compared with the corresponding core loss components of heat treated core materials. As the copper loss is equal for all investigates core materials and the core material that has not been heat treated gives the lowest core losses compared with other heat treated core materials, core material that has not been heat treated corresponds to highest efficiency especially at high speed region.

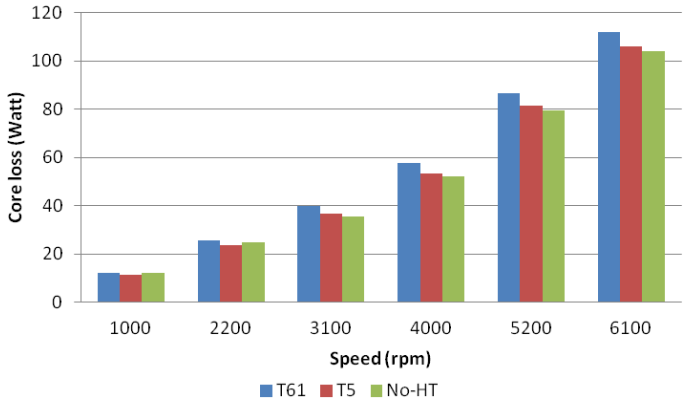

Figure 6.20 Core loss of IPMSM model for different heat treated core material

Though different heat treated core materials do not have any effect on the flux linkage of the core, open circuit voltage of the motor, back emf of the motor, torque per amp as well as the controlling current for the machine, saliency ratio of the IPMSM, the eddy current loss and corresponding harmonic eddy current loss are lower in the case of the IPMSM with the core material that has not been heat treated, which leads to slightly higher efficiency of the IPMSM. Thus, there is no general statement that heat treatment lowers the core loss in the core materials of an IPMSM though heat treatment offers better physical and mechanical properties.

Chapter 7

Validation of experimental data of SRA and non-SRA motors

Two identical models have been simulated uses the steel data for M-19 SRA and non-SRA samples obtained from the Epstein frame test. The models assume that after manufacturing, the two machines are identical except for steel characteristics. To limit simulation times to acceptable values, the simulations assume current sourced supply (as the output from a current controlled supply) and neglect switching and supply harmonics. Two machines (SRA and one non-SRA motor) have been constructed, again assuming identical characteristics other than the steel. Both lamination sets were obtained from a single supplier, all magnets were purchased as a single batch, both machines were wound by the one company and both frames constructed in the same machine shop. Simulated output data are analyzed in terms of total core loss, copper loss, inductances, efficiency, and controlling current at different desired torque and verified by experiments. Though harmonics core loss estimated from simulation described elsewhere (shown in Appendix C) total core loss are described here in order to compare with the experimentally obtained total core loss of SRA and non-SRA machine. Important factors that may affect the core loss computation experimentally are the windage and friction loss of the physical motor. The friction loss of the motor take place mainly due to the friction in the bearings of the motor and the windage loss of the motor takes place due to the air movement in the motor. The motor must be driven by other motor in order to determine the friction and windage loss of the motor. It is more difficult to determine the friction and windage loss for permanent magnet motor than other motors, because this test can be done for all other motors after full installation of the motor except the permanent magnet motor. The magnet is inserted in completely installed permanent magnet motor which includes the core loss with friction loss and windage loss when the machine is driven by other

machine at open circuit condition. The friction and windage test can be done only before the magnet insertion in the motor. Once the magnet is inserted, it is almost impossible to takeout the magnet without destroying the lamination of rotor especially in case of IPMSM. As the two IPMSMs are assumed identical (shown in Figure 7.1), one machine was used to determine the friction and windage loss of the machine having no magnet attached in it and assumed that the same friction and windage loss occur in other machine by neglecting the manufacturing and assembly dissimilarity. Hence, without separating the friction and windage loss from core loss would give more accurate results than using the core loss only.

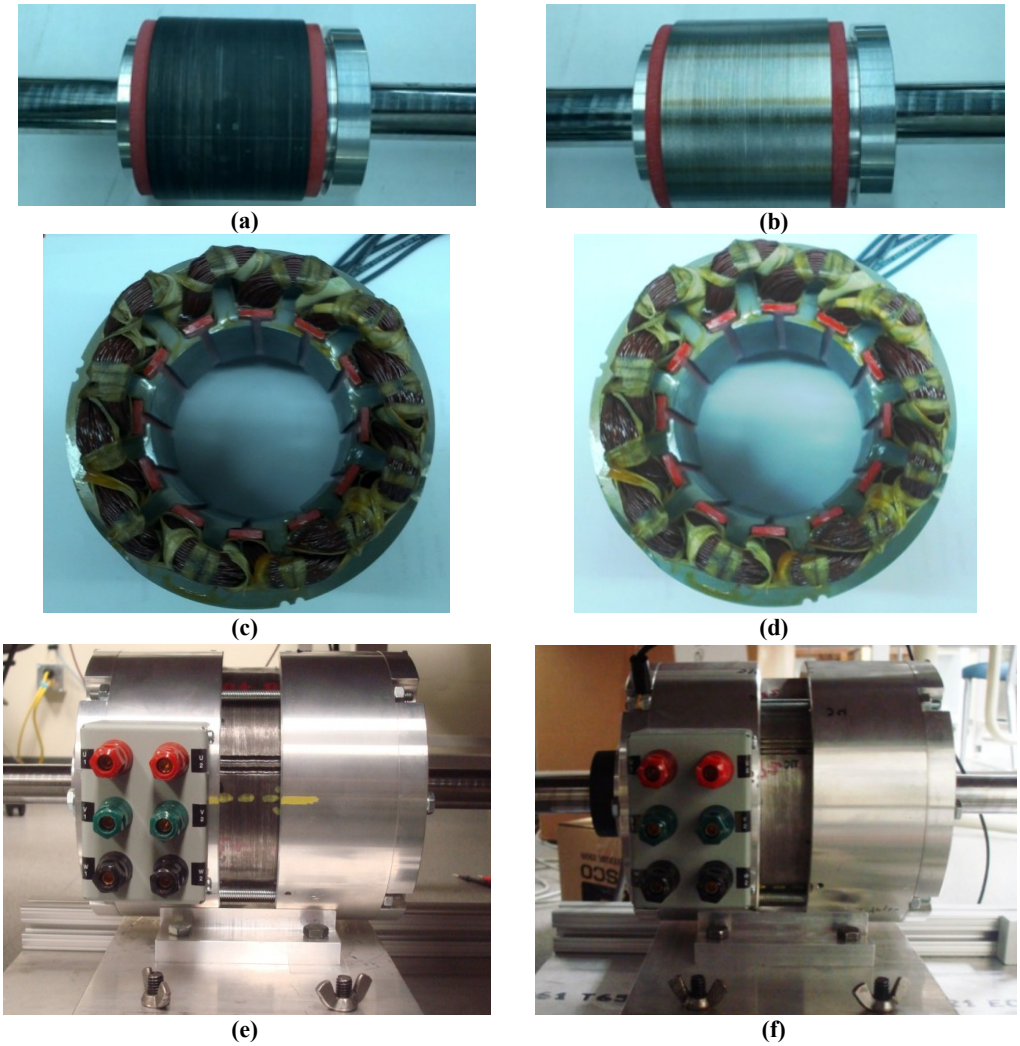

Figure 7.1 Picture of physical rotor (a) SRA (b) Non-SRA, stator (c) SRA (d) Non-SRA, and complete machine (e) SRA (f) Non-SRA

7.1 Experimental setup

A schematic diagram for the experimental setup is shown in Figure 7.2. A single DSC based control scheme is used to control the speed and torque of the machine; two separate inverters are controlled from the single DSC. The DSC is a TI28335 and is part of a PowerCon controller which handles all signals conditioning between the hardware and DSC. Control is implemented in C using TI code composer and is monitored in real time via JTAG emulator connection to a PC. Two identical setups are required for comparing the SRA and non-SRA machines. However, when the SRA machine performs as a motor, the other machine (Non-SRA) performs as a generator and vice versa. Experimental setups of SRA and non-SRA machines test are shown in Figure 7.3. Two machines are coupled through a torque transducer which is used to measure the output torque of the machine as a motor. One of the two inverters having input supply, is connected to the machine input supply (worked as a motor) to control the motor speed and other inverter having load resistor, is connected to the other machine (worked as a generator) to control the torque of the motor. Moreover, auto transformer is used to supply desired input voltage to the inverters which is connected to the motor. DSP code basically controls the gating signal of the inverter in order to get the motor terminal voltage by changing modulation index. However, required speed and required output torque are the input of that controller. Oscilloscope, digital power meter are used to measure the desired parameter such as torque, input power, input current, input voltage at loaded condition, back emf or open circuit voltage, etc.

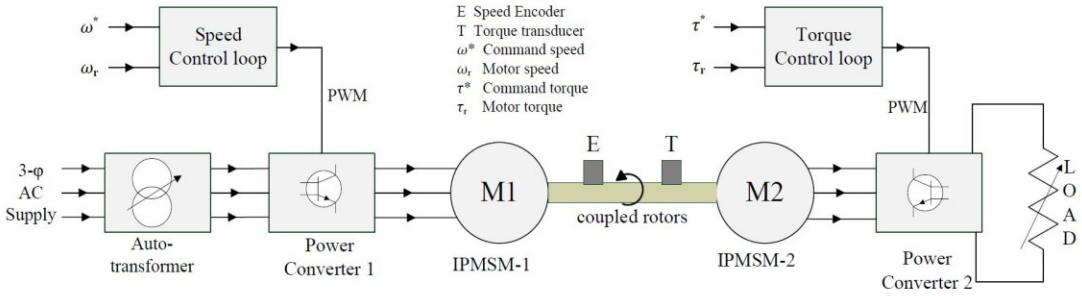

Figure 7.2 Schematic diagram of the experimental setup

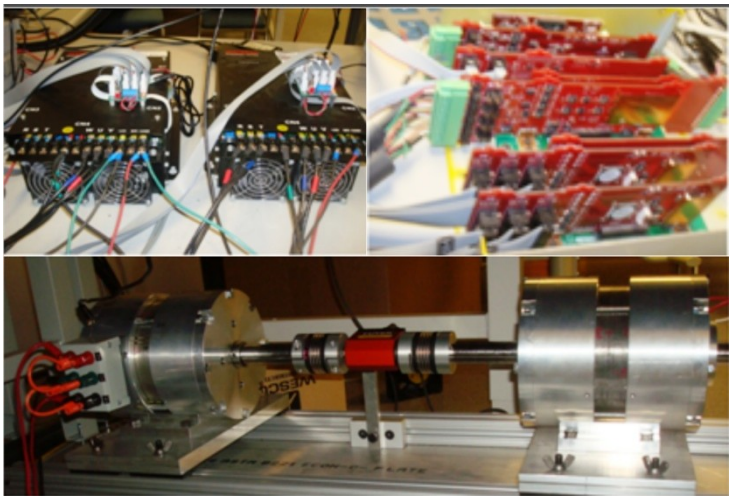

Figure 7.3 Experimental setup of SRA and non-SRA machines test

7.2 Simulated and experimental motor performance

Simulation model for SRA and non-SRA used the magnetic characteristics data obtained from Epstein frame test. Two identical models have been simulated regardless the manufacturing dissimilarity, switching loss and supply harmonics. Different output of two IPMSM such as open circuit voltage or back emf, torque ripple, core loss at open circuit and loaded condition and the efficiency are compared which are not only obtained from simulated value but also from experimental results.

7.2.1 Back emf or Open circuit voltage

Simulated result of open circuit voltage waveform and FFT analysis for SRA and non-SRA at 1000 rpm are shown in Figure 7.4. It is found that both waveforms are almost similar shape and the peak values are 91.74 V and 89.25 V for SRA and non-SRA

machines respectively. The fundamental voltage is 74.95V and THD is 14.65% for SRA machine as shown in figure. It is found from the fundamental voltage and electrical frequency for SRA machine, that the flux linkage to the coil is 143 mW which satisfy the flux linkage simulated value. However, non-SRA fundamental voltage is 73.97 V and THD of the waveform is 13.32% and flux linkage 141mW. The open circuit voltage of SRA machine contains more harmonics than the voltage of non-SRA machine though the fundamental voltages are very close to each other.

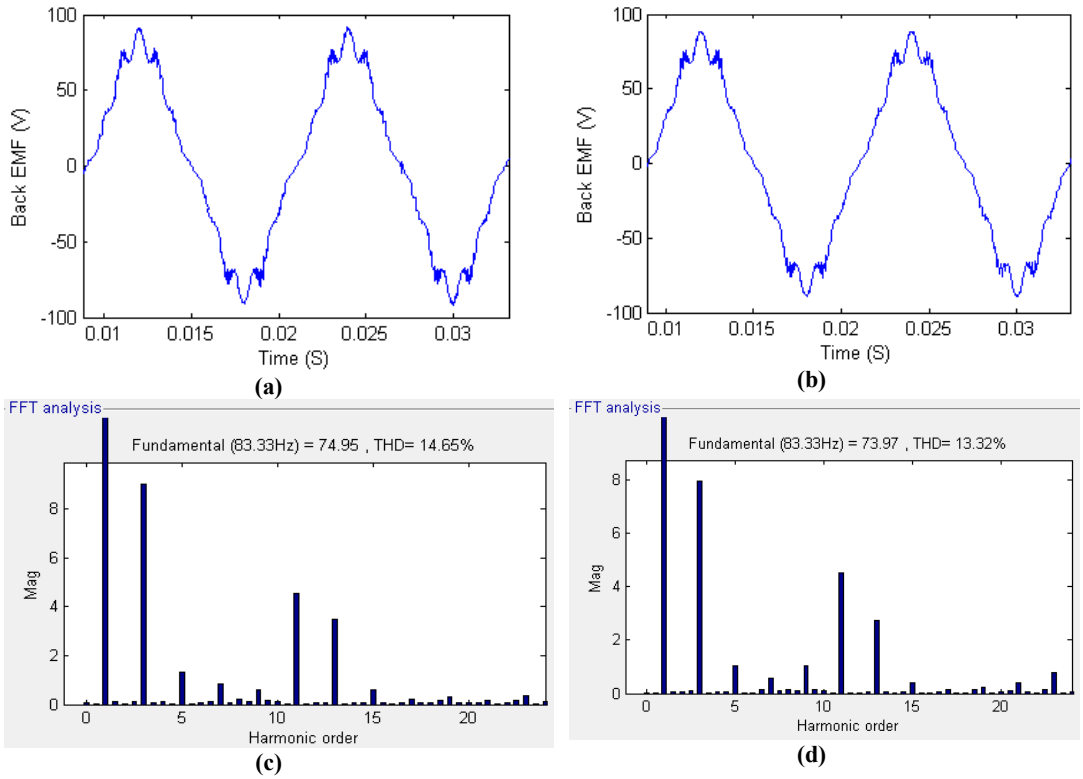

Figure 7.4 Simulated result of open circuit voltage waveform for (a) SRA (b) non-SRA and FFT for(c) SRA (d)non-SRA at 1000 rpm

In the experimental results, the open circuit voltage waveforms, its magnitudes, %THDs of SRA and non-SRA machine are quite different as illustrated in Figure 7. 5. It is found in case of SRA machine that the open circuit peak voltage at 1000 rpm is 81.63 V, fundamental voltage 69.44 V and %THD is 12.46%. However, the open circuit voltage, fundamental voltage and %THD values for non-SRA machine are 66.63 V, 59.5

V and 7.59% respectively. Therefore the flux linkages for SRA and non-SRA machine are 132 mW and 113 mW. Both flux linkage obtained experimentally are lower than the simulated value and these value are 7.7% lower for SRA and 19.9% lower for non-SRA. The harmonic content in open circuit voltage is significantly higher in case of SRA machine than non-SRA machine. One of the main reasons of distorted back emf is due to distorted flux density distribution in air gap [149]. However, the lower flux linkage value and different harmonics contain in back emf can cause dissimilarity of the expected performance of both machines.

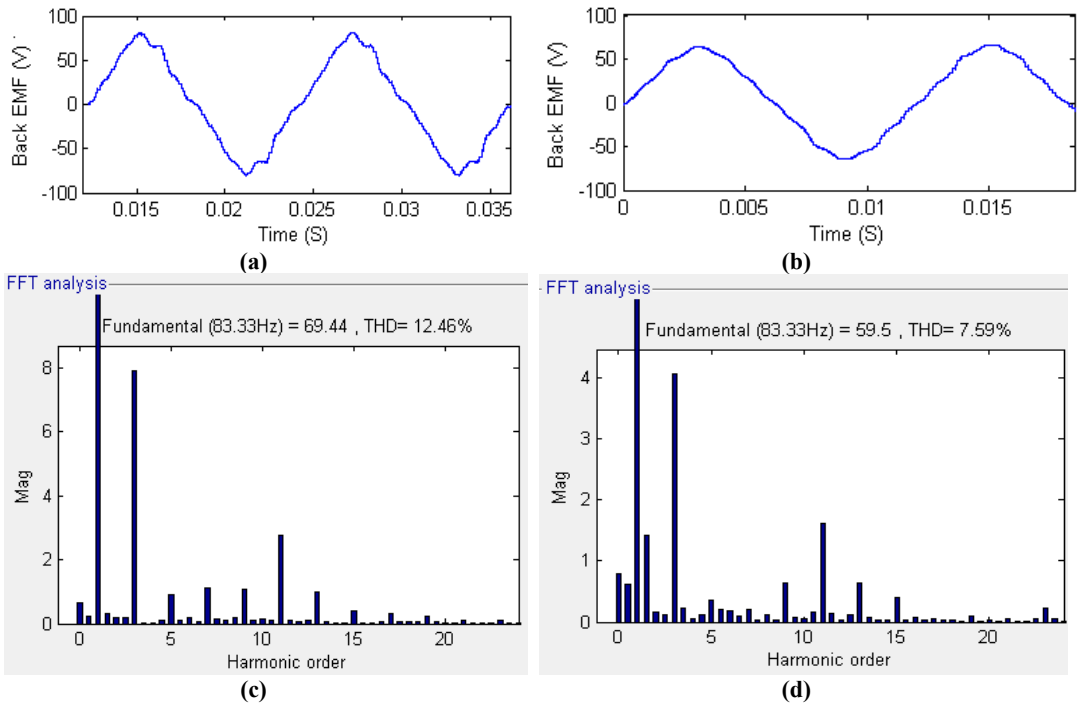

Figure 7. 5 Experimental result of open circuit voltage waveform for (a) SRA (b) non-SRA and FFT for(c) SRA (d)non-SRA at 1000 rpm

7.2.2 Torque ripple

There are different torque developed in an electrical motor such as cogging torque, torque ripple and electromagnetic torque. Torque ripple is a combination of reluctance harmonics, magnet flux space harmonics and supply current harmonics [147]. Electromagnetic torque which is the sum of reluctance torque and magnet torque is responsible to drive the motor at desired load. However, other torques produces noise and

vibration. Therefore less cogging torque and torque ripple are desirable for a good machine. Torque ripple obtained at base speed experimentally for SRA and non-SRA machines are shown in Figure 7.6. It is found even by close inspecting the figure that the ripple torque magnitude for SRA machine is very close to the ripple torque magnitude of non-SRA machine. Therefore the torque ripples are not affected in an important manner due to differently treated core materials.

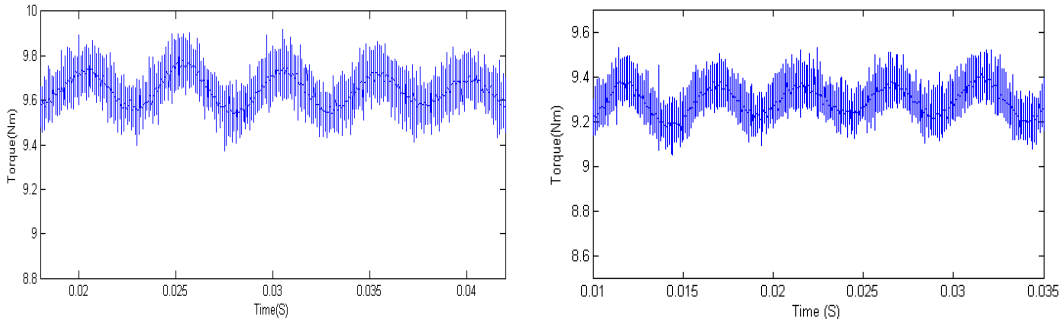

(a) **(b)**

Figure 7.6 Torque ripple of physical (a) SRA and (b) non-SRA machines

7.2.3 Inductance

Inductance can be measured experimentally in several ways. Standstill condition with a locked rotor is commonly used to measure the inductance of a machine. There are different ways to calculate the dq inductances under standstill condition. However inductance calculation method using reactive power is used here. The motor windings is conned as shown in Figure 7.7. A variable voltage is supplied to the motor terminals to calculate the dq inductances at different currents. A variac is used to generate variable amplitude sinusoidal voltage with a supply frequency (60 Hz). Equations (53, 54) are used to calculate the dq inductances separately. The voltage is applied to the stator winding on the condition that the rotor is locked at d axis position for d axis inductance measurement and the rotor is locked at q axis position for q-axis inductance measurement. Figure 7.8 shows the inductance test results of SRA and non-SRA machines w.r.t corresponding i_d and i_q currents. The figures show that L_q inductance is

affected by the saturation and L_d inductance is almost constant at all current level. The L_q inductance of SRA machine is almost same as L_q inductance of non SRA machine at all current range and L_d inductance of SRA machine is significantly lower than non-SRA machine. Therefore higher saliency ratio is established in case of SRA machine. The dq inductances are affected by the controlling currents of the machine. The controlling currents are different for different speed level and for different machines. However, the average L_d, L_q and Saliency ratio of SRA machine are 9.69 mH, 16.6 mH and 1.72 respectively. Whereas, the average L_d, L_q and Saliency ratio of non-SRA machine are 11.14 mH, 16.0 mH and 1.43 respectively. Similar process (like experiment setup) is followed to determine the simulated inductance value in order to compares rationally the experimental and simulated inductance values. Figure 7.9 shows the simulated inductance value of SRA and non-SRA machine. Simulated L_d and L_q values are lower to the corresponding experimental test results mainly because of experimental value considered the end windings of the machines. It is seen from simulation results that SRA machine also established higher saliency ratio compared with non- SRA machine. The experimental and simulation results of both machines vary within 9% in saliency ratio.

$$L_d = \frac{2}{3}\frac{Q_d}{2\pi f I_d^2} \tag{53}$$

$$L_q = \frac{2}{3}\frac{Q_q}{2\pi f I_q^2} \tag{54}$$

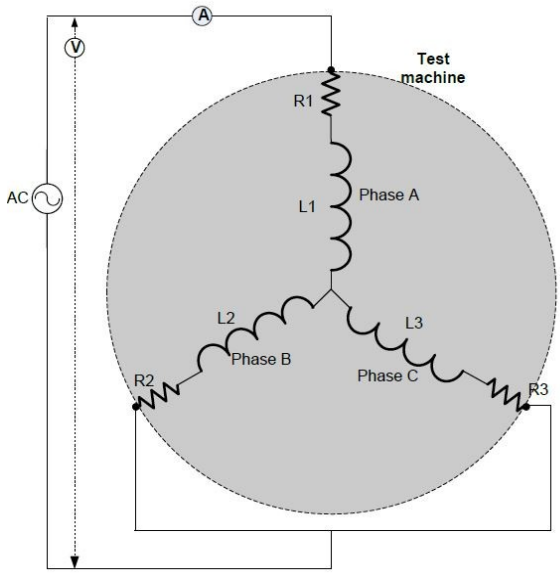

Figure 7.7 Connection diagram of inductance measurement

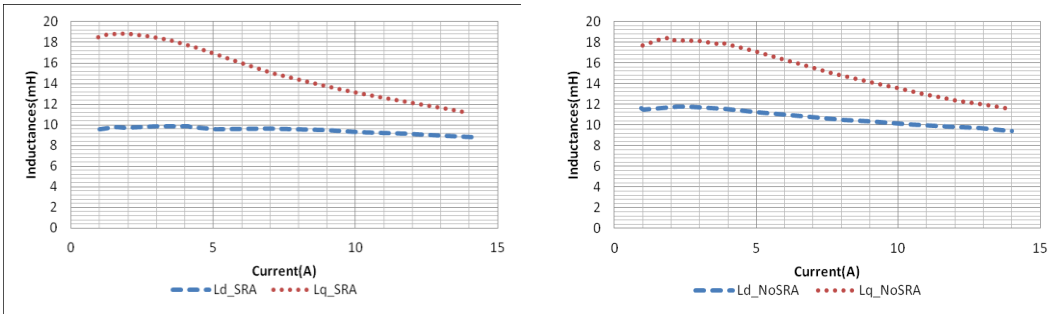

a) **(b)**

Figure 7.8 dq inductance tests results of (a) SRA and (b) Non-SRA machines

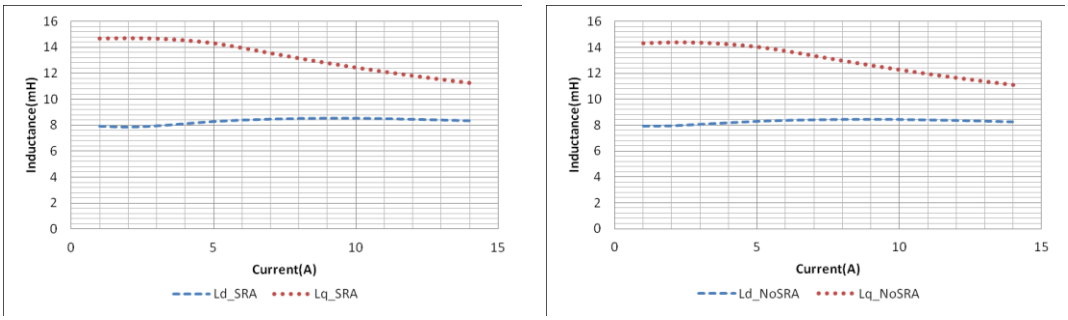

(a) **(b)**

Figure 7.9 Simulated dq inductance of (a) SRA and (b) Non-SRA machines

7.2.4 Core loss

Core loss of an IPMSM is the main dominating part especially at high speed region to determine the efficiency of the motor. Core loss could be calculated at open circuit or

loaded condition. Harmonics core loss affects more at loaded condition than open circuit condition (Shown in Appendix C) mainly due to the air gap flux distortion of the machine. However, the fundamental core loss component at loaded condition is lower than the fundamental core loss at open circuit condition mainly due to flux weakening at loaded condition. Therefore, total core loss at loaded condition is higher or lower than open circuit condition mainly depends on the harmonics core loss contribution at loaded condition. Total simulated core loss at open circuit condition for SRA and non-SRA machine are shown in Figure 7.10. It is found from the core loss data that the non- SRA machine have 18.8% higher core loss than SRA machine at the base speed. However, the core loss differences are not same at all speeds; non-SRA has higher core loss ranges from 14.4-18.8% than core loss of SRA machines for the speed ranges from 1000 - 4000 rpm. Friction and windage loss is not included in the simulation model. Moreover, pure sinusoidal wave is used instead of inverter supply in the simulation model. Therefore the core loss numerical scenario may be different for experimentally tested machine. As mentioned earlier the troublesome of determination of friction and windage loss of an IPMSM, the core loss in addition to friction and windage loss can give the better comparative scenario for experimentally SRA and non-SRA machines. However, the core loss curve for experimentally tested SRA and non-SRA machine at open circuit condition are shown in Figure 7.11 and core loss curve in addition to friction and windage loss at open circuit condition are shown in Figure 7.12. The tested core loss is lower than the predicted core loss provided that the friction losses of both machines are the same. Moreover, the increased core loss of non- SRA machine from core loss of SRA machine is ranging 30-50% and the increased core loss with friction and windage loss of non-SRA machine from SRA machine loss is ranging 10-20% which is almost similar to the increased simulated open circuit core loss.

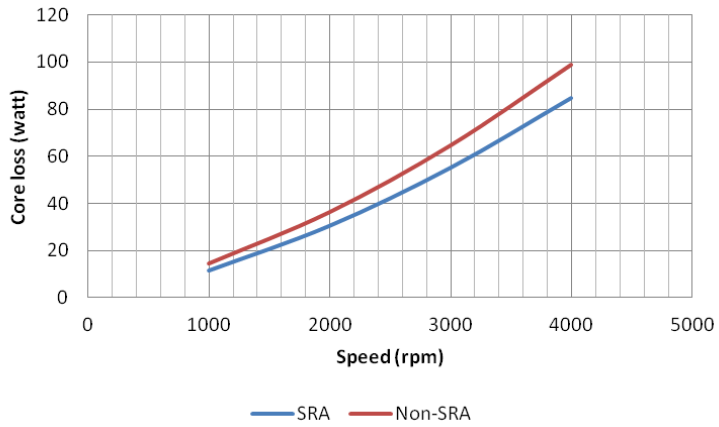

Figure 7.10 Simulated core loss at open circuit condition for SRA and non-SRA machines

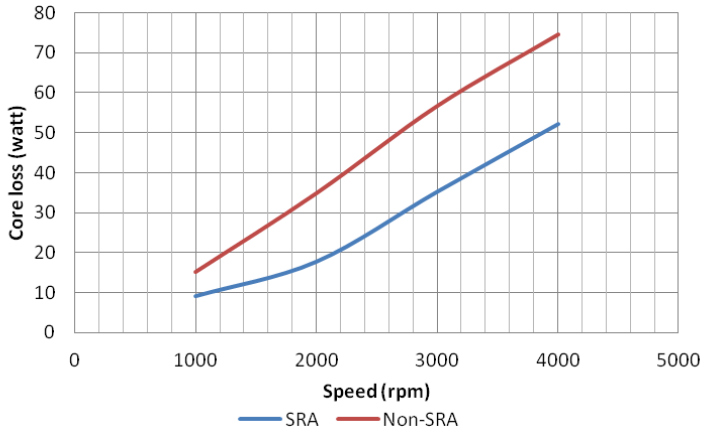

Figure 7.11 Core loss at open circuit condition for experimentally tested SRA and non-SRA machines

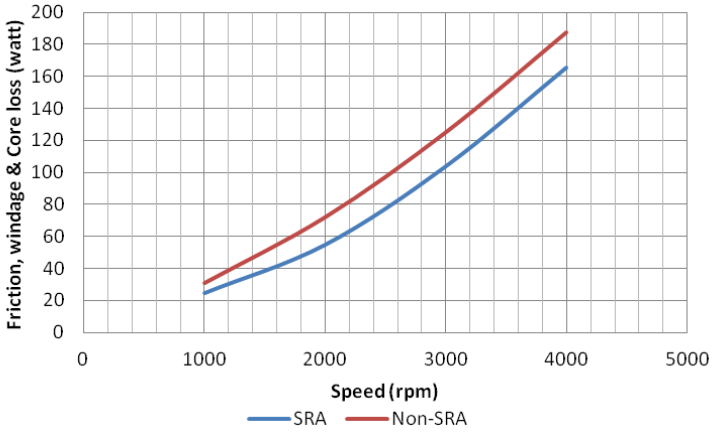

Figure 7.12 Core loss in addition to friction and windage loss of experimentally tested SRA and non-SRA machine at open circuit condition

Experimentally it is found that, core loss at loaded condition is much higher than core loss at open circuit condition for non-SRA machine than SRA machine. As the concerned

machine is coupled to the drive motor at the open circuit condition, the open circuit core loss is not affected by the switching loss, inverter supply voltage harmonics, flux weakening current, etc. On the other hand the core loss at loaded condition is affected by aforementioned factors. Table 7.1 shows the controlling current and joule loss at loaded condition of the tested machines. Core loss at loaded condition for experimentally tested SRA and non-SRA machines are shown in Figure 7.13. It is found form the core loss data that the non-SRA machine gives higher core loss than SRA machine at all speeds except at highest speed and the core loss difference varies in ranges 0-48%. As the SRA machine has physically higher linkage flux, higher flux weakening current is required by all the speeds. In SRA machine higher flux weakening current can make more distorted air-gap flux which may produce enough core loss harmonics to increase the core loss than expected. This harmonics effect is seen explicitly at highest speed in case of SRA machine. Core loss in addition with friction and windage loss increases in the range of 0-40% for non-SRA machine compared with SRA machine as shown in Figure 7.14. Since the friction and windage loss are assumed the same, the core loss curve and core loss in addition with friction & windage loss follow the same trend.

TABLE 7.1 CONTROLLING CURRENT, FRICTION LOSS AND JOULE LOSS OF TESTED MACHINE

Speed (rpm)	Friction loss (Watt)	SRA machine			Non-SRA machines		
		I_d current (A)	I_q current (A)	Joule loss (watt)	I_d current (A)	I_q current (A)	Joule loss (watt)
1000	15.36	-2.63	11.58	139.51	-2.57	14.03	201.34
2000	36.97	-3.98	4.92	39.65	-3.80	5.60	45.30
3000	68.48	-6.92	3.26	57.95	-7.60	2.12	61.63
4000	109.58	-7.87	1.74	64.33	-7.80	1.37	62.09

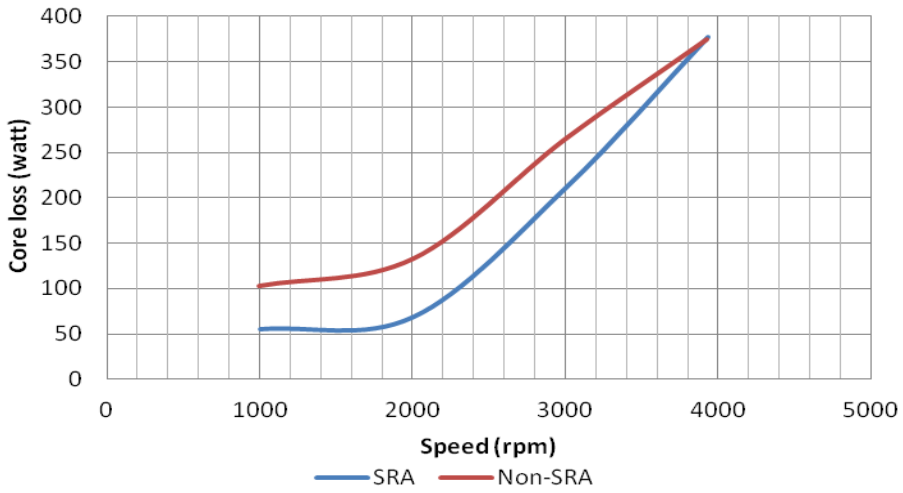

Figure 7.13 Core loss at loaded condition for experimentally tested SRA and non-SRA machines

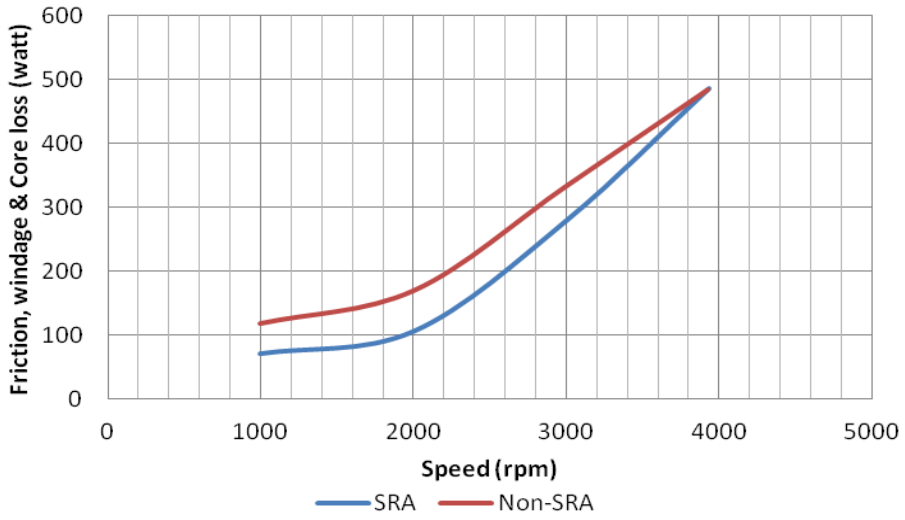

Figure 7.14 Core loss in addition to friction and windage loss of experimentally tested SRA and non-SRA machines at loaded condition

The non- SRA machine requires different d and q-axis current to meet the same torque as well as same power compared with SRA machine. One of the reasons is that the flux linkages in both machines are not same. This different current condition affect on joule loss which results affects the efficiency of the machine. The efficiency of the SRA and non-SRA machines for rated output power is shown in

Figure 7.15. The figure shows that the efficiency of the SRA machine is always higher than non-SRA machine at all operated speed levels and the efficiency variation range is in between 2-7.5% where the efficiency variation is decreased with the increase of speed.

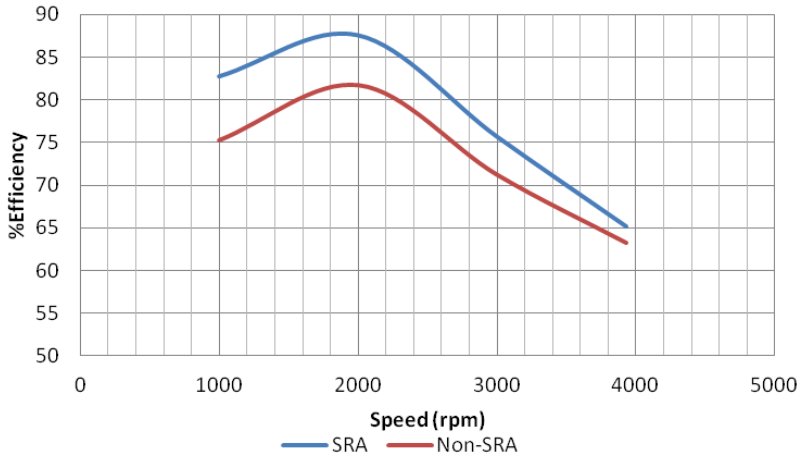

Figure 7.15 Efficiency of experimentally tested SRA and non-SRA machines

As the field weakening current is different due to different flux linkage, it is preferable to compare both machines at different torque point without applying the field weakening current. At that condition q axis current produce the magnet torque which is equal to the electromagnetic torque as the reluctance torque is zero. Required q axis currents obtained from the simulation and experimentally are shown in Figure 7.16. As the flux linkages are almost same in simulated models and there is no field weakening current contributes in torque, the q axis simulated currents are almost same for both machines. Whereas tested q axis currents to meet the specific torque are higher due to lower flux linkage in case of tested non-SRA machine compared with tested SRA machine. These q-axis current differences are within 16-25% range. Moreover, at that condition the simulated and tested core loss of SRA machine is lower compared with non-SRA machine at any specific torque point and at the base speed shown in Figure 7.17. The loss discrepancy is within 10-47% range obtained in experiment. However the core loss curve with friction and windage loss follows the same trends like core loss curves as the friction and

windage loss are assumed the same for both machines. Figure 7. 18 shows the efficiency of SRA and non-SRA machine without applying field weakening current at base speed. As friction and windage losses are ignored in simulated model, the simulated efficiency is higher than the efficiency obtained in experiments for both SRA and non SRA machines. However, efficiency curves obtained from simulation and experiment follow the same trends.

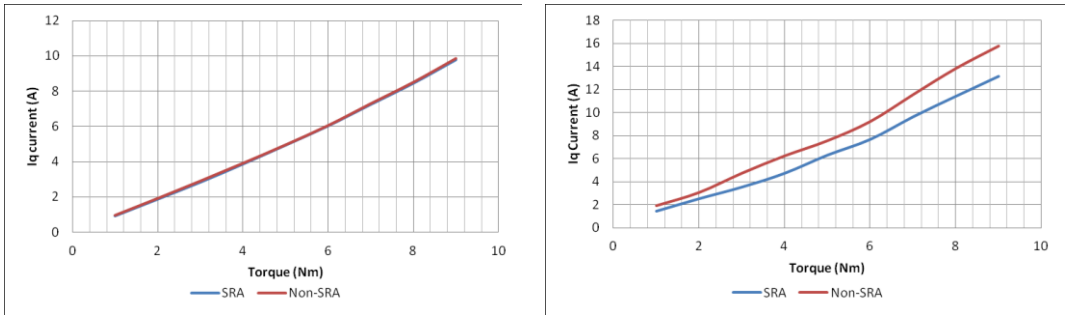

(a) (b)

Figure 7.16 (a) Simulated and (b) experimental q-axis current vs torque profile for SRA and non-SRA machines without flux weakening condition

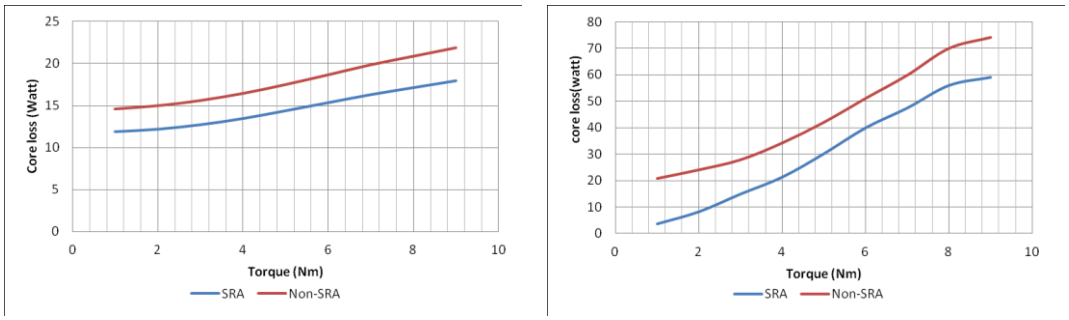

(a) **(b)**

Figure 7.17 Core loss of (a) simulated and (b) tested SRA and non-SRA machines without applying field weakening current

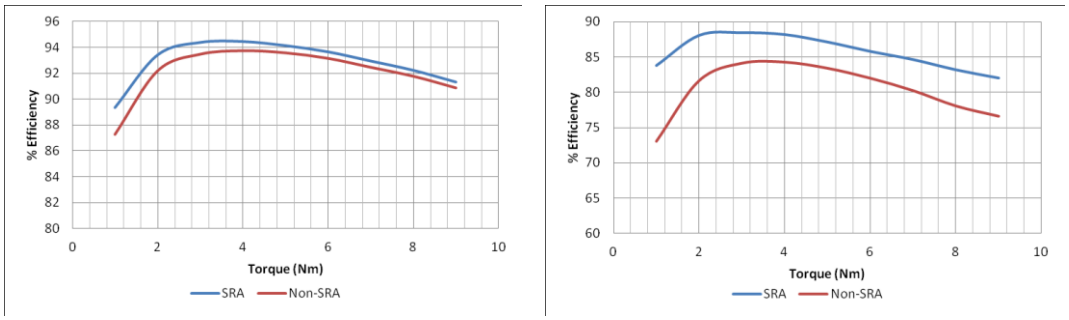

(a) **(b)**

Figure 7. 18 Efficiency of (a) simulated and (b) tested SRA and non-SRA machines without applying field weakening current at base speed

In case of SRA machine the core loss are lower, q axis current which effects on joule loss are lower, friction & windage loss are the same for both machines, resulting the efficiency of SRA machine is higher compared with non-SRA machine. The analysis based on zero field-weakening is done in order to consider the same boundary condition for comparing the both machines. Therefore, the rational judgment is more acceptable than numerical conclusion.

Experimental results highlight the difficulty of components losses based on material properties in a functioning motor. It is clear that difference in permeability mean that the two machines are operating at different flux levels. Therefore, it require different stator currents to obtain similar performance.

Chapter 8

Conclusion

This thesis focuses on the design and analysis of the core loss of an IPMSM for a hybrid vehicle. A number of parameters affecting motor performance like treatment of core material, magnet orientation in the rotor, and magnetic strength have been identified through simulation. However, effect of annealing on motor performance has also been investigated experimentally. Co-relation and incongruity between simulated and experimental results have been done. The results obtained from this research can be divided into two phases. First phase includes finite element analysis for investigating the influence of magnet orientation, influence of magnetic strength, stress analysis of the motor, effect of SRA, and impact of heat treatment on motor performance, etc. Second phase involves investigation experimentally where Epstein frame tests for different treated core materials is done for estimation of magnetic properties. Two machines (SRA and non-SRA) were constructed with the same dimensions for analysis and comparison of the performances of both machine types.

8.1 Summary of simulation results

Simulation results (FEA) illustrate the impact of correctly accounting for harmonic core losses in concentrated winding IPMSM. The influence of magnet leakage flux and magnet orientation is highlighted. As the speed is increased, the influence of harmonics fluxes becomes more significant when the machine is loaded. These issues are illustrated using design studies on three optimized IPM machines. The importance of trading off reluctance torque and excitation torque is highlighted through the adjustment to magnet strength and it is noted that this has less impact on harmonic losses than the design of the flux barrier magnet shapes.

FEA also investigates the effect of different heat treated (T5, T61) core materials on performance of the IPMSM model. It shows that different heat treated core materials do not have any effect on the flux linkage of the core, open circuit voltage of the motor, back emf of the motor, torque per amp as well as the controlling current for the machine. Moreover, the saliency ratio of the IPMSM is not considerably affected due to the different heat treated core materials. Hence the reluctance torque as well as magnet torque is un-affected. The joule loss and hysteresis loss of the IPMSM model are not affected due to different specified heat treated core materials. However, the eddy current loss and corresponding harmonic eddy current loss are lower in the case of the IPMSM with the core material that has not been heat treated, which leads to slightly higher efficiency of the IPMSM. Thus, there is a trade-off between better physical, mechanical properties and lower core loss in the core materials of an IPMSM.

FEA also presents the variation in performance of machines used tested JFE steel SRA data, tested JFE steel non-SRA data and JFE steel manufacturer's data under same rated power output. As the saliency ratio is lower in case of SRA and non-SRA, an increased field weakening currents are used in order to meet the output torque, resulting in an increase in winding copper losses and limit the efficiency. The model using test data of SRA core material provides highest efficiency among all the investigated models. However the predicted efficiency discrepancy level among all the cases is within ±6.8%. Moreover, both M-19 SRA steel and non-SRA steel (AK steel) which are used to build physical machine are considered to build a simulation model. Though numerical loss data are not same for AK and JFE steel, Ak SRA and non-SRA machines performance follow the same trends like JFE SRA and non-SRA machines.

8.2 Summary of the experimental test

There are two experimental setups regarding core loss. First one uses Epstein frame test setup to predict the core loss and magnetic characteristics such as dc magnetisation curve, dc permeability, ac peak permeability, ac BH curve of the core materials. Second one uses the physical machine to get the motor performance in terms of open circuit voltage waveform, torque ripple, core loss, efficiency, etc.

8.2.1 Epstein frame test summary

Using an ASTM standard Epstein frame test, it is found that the magnetic properties of T5 heat treated material and the core material that has not been heat treated are very close to each other in terms of relative permeability, DC BH curve and AC BH loop. The T61 heat treated core material gets saturated faster than the T5 heat treated core materials and the core material that has not been heat treated. However, the core material that has not been heat treated gives the lowest specific core loss among all the specified heat treated core materials.

In the case of SRA and non-SRA steels, Epstein test data indicates that the SRA process will improve permeability and reduce core loss. The influence of SRA is most clearly seen when considering core loss. The measured core loss density from the Epstein tests is lower after SRA, resulting in lower iron loss predictions in the machine model. However, the core loss maintains linear relationship with frequency up to mid speed ranges and maintains square relationship with frequency in high speed ranges.

8.2.2 Summary of experimentally tested SRA and non-SRA machines

It is found experimentally that flux linkage are 7.7% lower and 19.9% lower than expected simulation value for SRA and non-SRA machine respectively. Therefore the fundamental back emf voltage of SRA machine is higher than non-SRA machine. However the composite back emf of SRA machine is more distorted from sinusoidal

voltage compared with back emf of non-SRA machine. Torque ripple magnitude for SRA machine is slightly higher than of non-SRA machine mainly due to back emf harmonics distinction and reluctance torque distinction. SRA core treatment of the machine does not affect on L_q inductance value but affects on L_d inductance value. However, SRA machine have the higher saliency ratio than non-SRA machine at all motor's controlling currents. Though, non-SRA has higher simulated core loss at open circuit condition of 14.4-18.8% than core loss of SRA machines for the speed ranges of 1000- 4000 rpm, experimentally when considering core loss with friction & windage loss this range is 10-20% following the same trend. Core loss at loaded condition is much higher than core loss at open circuit condition due to switching loss, inverter supply voltage harmonics, and distorted air-gap flux by producing core loss harmonics. Core loss in addition with friction and windage loss increases in the range of 0-40% for non-SRA machine compared with SRA machine. However, efficiency of the SRA machine is always higher than non-SRA machine in the range of 2-7.5% for the speed range of 1000-4000 rpm. Moreover, for rated output power the SRA machine gives the higher efficiency than non-SRA machine at base speed when no field weakening current is applied in order to maintain the same boundary condition for both machines.

In conclusion, the research outputs pointed out in the PhD thesis is a complete solution to predict, address, and verify the core losses, through modeling and analysis of the core loss of a motor using the same core materials differently treated. This research will not only make easy fundamental understanding of differently treated core materials of an electric machine but also evolvement of motor in hybrid vehicle applications.

References:

[1] C. C. Chan, "The state of the art of electric and hybrid vehicles," *Proceedings of the IEEE,* vol. 90, pp. 247-275, 2002.

[2] D. Diallo, M. E. H. Benbouzid, and A. Makouf, "A fault-tolerant control architecture for induction motor drives in automotive applications," *Vehicular Technology, IEEE Transactions on,* vol. 53, pp. 1847-1855, 2004.

[3] A. G. Jack, B. C. Mecrow, and J. A. Haylock, "A comparative study of permanent magnet and switched reluctance motors for high-performance fault-tolerant applications," *Industry Applications, IEEE Transactions on,* vol. 32, pp. 889-895, 1996.

[4] N. Bianchi, Pre, x, M. D., G. Grezzani, and S. Bolognani, "Design considerations on fractional-slot fault-tolerant synchronous motors," in *Electric Machines and Drives, 2005 IEEE International Conference on*, 2005, pp. 902-909.

[5] A. J. Moses and J. Leicht, "Measurement and prediction of iron loss in electrical steel under controlled magnetization condition," *in Przegl. Elektrotech,* pp. 1181-1187, 2004.

[6] M. Popescu, D. M. Ionel, A. Boglietti, A. Cavagnino, C. Cossar, and M. I. McGilp, "A General Model for Estimating the Laminated Steel Losses Under PWM Voltage Supply," *Industry Applications, IEEE Transactions on,* vol. 46, pp. 1389-1396, 2010.

[7] Z. Gmyrek, A. Boglietti, and A. Cavagnino, "Estimation of Iron Losses in Induction Motors: Calculation Method, Results, and Analysis," *Industrial Electronics, IEEE Transactions on,* vol. 57, pp. 161-171, 2010.

[8] K. Matsumura and B. Fukuda, "Recent developments of non-oriented electrical steel sheets," *Magnetics, IEEE Transactions on,* vol. 20, pp. 1533-1538, 1984.

[9] A. Chaudhurya, R. Khatirkar, N. N. Viswanathan, V. Singal, S. J. Ingle, A.;, and I. Samajdar, "Low silicon non-grain-oriented electrical steel: Linking magnetic properties with metallurgical factors," *Journal of Magnetism and Magnetic Materials,* vol. 313, pp. .21–28, 2007.

[10] M. Ibrahim and P. Pillay, "Advanced Testing and Modeling of Magnetic Materials Including a New Method of Core Loss Separation for Electrical Machines," *Industry Applications, IEEE Transactions on,* vol. 48, pp. 1507-1515, 2012.

[11] K. H. Carpenter, "A differential equation approach to minor loops in the Jiles-Atherton hysteresis model," *Magnetics, IEEE Transactions on,* vol. 27, pp. 4404-4406, 1991.

[12] E. Dlala, J. Saitz, and A. Arkkio, "Hysteresis Modeling Based on Symmetric Minor Loops," *Magnetics, IEEE Transactions on,* vol. 41, pp. 2343-2348, 2005.

[13] D. C. Jiles, "A self consistent generalized model for the calculation of minor loop excursions in the theory of hysteresis," *Magnetics, IEEE Transactions on,* vol. 28, pp. 2602-2604, 1992.

[14] T. L. Mthombeni, P. Pillay, and R. M. W. Strnat, "New Epstein Frame for Lamination Core Loss Measurements Under High Frequencies and High Flux Densities," *Energy Conversion, IEEE Transactions on,* vol. 22, pp. 614-620, 2007.

[15] E. Dlala, "A Simplified Iron Loss Model for Laminated Magnetic Cores," *Magnetics, IEEE Transactions on,* vol. 44, pp. 3169-3172, 2008.

[16] T. Kosaka, H. Hasegawa, N. Matsui, T. Shikayama, and R. Oguro, "Experimental investigations into skin effect influences on current distortion and increase in loss for 20 kHz PWM-VSI-fed slotless PMSM drives," in *Industry Applications*

Conference, 2001. Thirty-Sixth IAS Annual Meeting. Conference Record of the 2001 IEEE, 2001, pp. 2374-2379 vol.4.

[17] M. Ibrahim and P. Pillay, "Core Loss Prediction in Electrical Machine Laminations Considering Skin Effect and Minor Hysteresis Loops," *Industry Applications, IEEE Transactions on,* vol. PP, pp. 1-1, 2013.

[18] H. Yunkai, D. Jianning, Z. Jian Guo, and G. Youguang, "Core Loss Modeling for Permanent-Magnet Motor Based on Flux Variation Locus and Finite-Element Method," *Magnetics, IEEE Transactions on,* vol. 48, pp. 1023-1026.

[19] L. R. Dupre, O. Bottauscio, M. Chiampi, M. Repetto, and J. A. A. Melkebeek, "Modeling of electromagnetic phenomena in soft magnetic materials under unidirectional time periodic flux excitations," *Magnetics, IEEE Transactions on,* vol. 35, pp. 4171-4184, 1999.

[20] S. E. Zirka, Y. I. Moroz, P. Marketos, and A. J. Moses, "Loss Separation in Nonoriented Electrical Steels," *Magnetics, IEEE Transactions on,* vol. 46, pp. 286-289, 2010.

[21] D. M. Ionel, M. Popescu, S. J. Dellinger, T. J. E. Miller, R. J. Heideman, and M. I. McGilp, "On the variation with flux and frequency of the core loss coefficients in electrical machines," *Industry Applications, IEEE Transactions on,* vol. 42, pp. 658-667, 2006.

[22] S. A. Rahman, B. Vaseghi, and A. M. Knight, "Influence of steel BH characteristics on IPMSM performance," in *Electrical Machines (ICEM), 2012 XXth International Conference on*, 2012, pp. 321-327.

[23] S. Yanase, H. Kimata, Y. Okazaki, and S. Hashi, "A simple predicting method for magnetic losses of electrical steel sheets under arbitrary induction waveform," *Magnetics, IEEE Transactions on,* vol. 41, pp. 4365-4367, 2005.

[24] F. Fiorillo and A. Novikov, "Power losses under sinusoidal, trapezoidal and distorted induction waveform," *Magnetics, IEEE Transactions on,* vol. 26, pp. 2559-2561, 1990.

[25] E. Barbisio, F. Fiorillo, and C. Ragusa, "Predicting loss in magnetic steels under arbitrary induction waveform and with minor hysteresis loops," *Magnetics, IEEE Transactions on,* vol. 40, pp. 1810-1819, 2004.

[26] M. Amar and R. Kaczmarek, "A general formula for prediction of iron losses under nonsinusoidal voltage waveform," *Magnetics, IEEE Transactions on,* vol. 31, pp. 2504-2509, 1995.

[27] P. Rasilo and A. Arkkio, "Modeling the effect of inverter supply on eddy-current losses in synchronous machines," in *Power Electronics Electrical Drives Automation and Motion (SPEEDAM), 2010 International Symposium on*, 2010, pp. 861-865.

[28] K. Yamazaki and A. Abe, "Loss Investigation of Interior Permanent-Magnet Motors Considering Carrier Harmonics and Magnet Eddy Currents," *Industry Applications, IEEE Transactions on,* vol. 45, pp. 659-665, 2009.

[29] G. Bertotti, "General properties of power losses in soft ferromagnetic materials," *Magnetics, IEEE Transactions on,* vol. 24, pp. 621-630, 1988.

[30] D. Lin, P. Zhou, W. N. Fu, Z. Badics, and Z. J. Cendes, "A dynamic core loss model for soft ferromagnetic and power ferrite materials in transient finite element analysis," *Magnetics, IEEE Transactions on,* vol. 40, pp. 1318-1321, 2004.

[31] I. D. Mayergoyz and F. Abdel-Kader, "The analytical calculation of eddy current losses in steel laminations subjected to rotating magnetic fields," *Magnetics, IEEE Transactions on,* vol. 20, pp. 2007-2009, 1984.

[32] M. Popescu and D. M. Ionel, "A Best-Fit Model of Power Losses in Cold Rolled-Motor Lamination Steel Operating in a Wide Range of Frequency and Magnetization," *Magnetics, IEEE Transactions on,* vol. 43, pp. 1753-1756, 2007.

[33] A. Boglietti, M. Lazzari, and M. Pastorelli, "Iron losses prediction with PWM inverter supply using steel producer data sheets," in *Industry Applications Conference, 1997. Thirty-Second IAS Annual Meeting, IAS '97., Conference Record of the 1997 IEEE*, 1997, pp. 83-88 vol.1.

[34] C. Yicheng and P. Pillay, "An improved formula for lamination core loss calculations in machines operating with high frequency and high flux density excitation," in *Industry Applications Conference, 2002. 37th IAS Annual Meeting. Conference Record of the*, 2002, pp. 759-766 vol.2.

[35] L. T. Mthombeni and P. Pillay, "Core losses in motor laminations exposed to high-frequency or nonsinusoidal excitation," *Industry Applications, IEEE Transactions on,* vol. 40, pp. 1325-1332, 2004.

[36] A. Boglietti, A. Cavagnino, M. Lazzari, and M. Pastorelli, "Predicting iron losses in soft magnetic materials with arbitrary voltage supply: an engineering approach," *Magnetics, IEEE Transactions on,* vol. 39, pp. 981-989, 2003.

[37] A. Boglietti, A. Cavagnino, M. Lazzari, and M. Pastorelli, "Two simplified methods for the iron losses prediction in soft magnetic materials supplied by PWM inverter," in *Electric Machines and Drives Conference, 2001. IEMDC 2001. IEEE International*, 2001, pp. 391-395.

[38] A. M. Knight, J. C. Salmon, and J. Ewanchuk, "Integration of a First Order Eddy Current Approximation With 2D FEA for Prediction of PWM Harmonic Losses in Electrical Machines," *Magnetics, IEEE Transactions on,* vol. 49, pp. 1957-1960, 2013.

[39] K. Yamazaki and Y. Seto, "Iron loss analysis of interior permanent-magnet synchronous motors-variation of main loss factors due to driving condition," *Industry Applications, IEEE Transactions on,* vol. 42, pp. 1045-1052, 2006.

[40] J. Pippuri, A. Belahcen, E. Dlala, and A. Arkkio, "Inclusion of Eddy Currents in Laminations in Two-Dimensional Finite Element Analysis," *Magnetics, IEEE Transactions on,* vol. 46, pp. 2915-2918, 2010.

[41] I. Lar and M. M. Radulescu, "Equivalent core-loss resistance identification for interior permanent-magnet synchronous machines," in *Electrical Machines (ICEM), 2012 XXth International Conference on*, pp. 1667-1671.

[42] Z. Yu, M. C. Cheng, and P. Pillay, "A Novel Hysteresis Core Loss Model for Magnetic Laminations," *Energy Conversion, IEEE Transactions on,* vol. 26, pp. 993-999.

[43] P. Rasilo, A. Belahcen, and A. Arkkio, "Experimental determination and numerical evaluation of core losses in a 150-kVA wound-field synchronous machine," *Electric Power Applications, IET,* vol. 7.

[44] M. Barcaro, N. Bianchi, and F. Magnussen, "Rotor Flux-Barrier Geometry Design to Reduce Stator Iron Losses in Synchronous IPM Motors Under FW Operations," *Industry Applications, IEEE Transactions on,* vol. 46, pp. 1950-1958, 2010.

[45] L. Alberti, E. Fornasiero, N. Bianchi, and S. Bolognani, "Impact of Rotor Losses in a 12-Slot 10-Pole Axial Flux PM Machine," in *Industry Applications Society Annual Meeting, 2008. IAS '08. IEEE*, 2008, pp. 1-8.

[46] H. Toda, X. Zhenping, W. Jiabin, K. Atallah, and D. Howe, "Rotor eddy-current loss in permanent magnet brushless machines," *Magnetics, IEEE Transactions on,* vol. 40, pp. 2104-2106, 2004.

[47] G. De Donato, F. G. Capponi, G. A. Rivellini, and F. Caricchi, "Integral-Slot Versus Fractional-Slot Concentrated-Winding Axial-Flux Permanent-Magnet Machines: Comparative Design, FEA, and Experimental Tests," *Industry Applications, IEEE Transactions on,* vol. 48, pp. 1487-1495, 2012.

[48] A. M. El-Refaie, "Fractional-Slot Concentrated-Windings Synchronous Permanent Magnet Machines: Opportunities and Challenges," *Industrial Electronics, IEEE Transactions on,* vol. 57, pp. 107-121, 2010.

[49] J. J. Germishuizen and M. J. Kamper, "IPM Traction Machine With Single Layer Non-Overlapping Concentrated Windings," *Industry Applications, IEEE Transactions on,* vol. 45, pp. 1387-1394, 2009.

[50] R. Wrobel, P. H. Mellor, N. McNeill, and D. A. Staton, "Thermal Performance of an Open-Slot Modular-Wound Machine With External Rotor," *Energy Conversion, IEEE Transactions on,* vol. 25, pp. 403-411, 2010.

[51] M. R. Shah, A. M. El-Refaie, and K. Sivasubramaniam, "Analysis of turn-to-turn faults in surface PM machines with multi-layer fractional-slot concentrated windings," in *Electrical Machines, 2008. ICEM 2008. 18th International Conference on*, 2008, pp. 1-4.

[52] S. Morimoto, "Trend of Permanent Magnet Synchronous Machines," *Electrical and Electronic Engineering, IEEJ Transactions on,* vol. 2, pp. 101-108, 2007.

[53] N. Bianchi, S. Bolognani, Pre, x, M. D., and G. Grezzani, "Design considerations for fractional-slot winding configurations of synchronous machines," *Industry Applications, IEEE Transactions on,* vol. 42, pp. 997-1006, 2006.

[54] Y. Honda, T. Nakamura, T. Higaki, and Y. Takeda, "Motor design considerations and test results of an interior permanent magnet synchronous motor for electric vehicles," in *Industry Applications Conference, 1997. Thirty-Second IAS Annual Meeting, IAS '97., Conference Record of the 1997 IEEE*, 1997, pp. 75-82 vol.1.

[55] J. Cros and P. Viarouge, "Synthesis of high performance PM motors with concentrated windings," in *Electric Machines and Drives, 1999. International Conference IEMD '99*, 1999, pp. 725-727.

[56] E. Levi, "Multiphase Electric Machines for Variable-Speed Applications," *Industrial Electronics, IEEE Transactions on,* vol. 55, pp. 1893-1909, 2008.

[57] C. Gerada and K. J. Bradley, "Integrated PM Machine Design for an Aircraft EMA," *Industrial Electronics, IEEE Transactions on,* vol. 55, pp. 3300-3306, 2008.

[58] S. Brisset, D. Vizireanu, and P. Brochet, "Design and Optimization of a Nine-Phase Axial-Flux PM Synchronous Generator With Concentrated Winding for Direct-Drive Wind Turbine," *Industry Applications, IEEE Transactions on,* vol. 44, pp. 707-715, 2008.

[59] Z. Zhuoran, Y. Yangguang, Y. Shanshui, and B. Zhou, "Development of a New Permanent-Magnet BLDC Generator Using 12-Phase Half-Wave Rectifier," *Industrial Electronics, IEEE Transactions on,* vol. 56, pp. 2023-2029, 2009.

[60] F. Locment, E. Semail, and X. Kestelyn, "Vectorial Approach-Based Control of a Seven-Phase Axial Flux Machine Designed for Fault Operation," *Industrial Electronics, IEEE Transactions on,* vol. 55, pp. 3682-3691, 2008.

[61] L. Chong, R. Dutta, and M. F. Rahman, "Design of a highly efficient 1kW concentric wound IPM machine with a very wide constant power speed range," in *Power Electronics Conference (IPEC), 2010 International*, 2010, pp. 1956-1961.

[62] A. M. El-Refaie and T. M. Jahns, "Impact of Winding Layer Number and Magnet Type on Synchronous Surface PM Machines Designed for Wide Constant-Power Speed Range Operation," *Energy Conversion, IEEE Transactions on,* vol. 23, pp. 53-60, 2008.

[63] A. M. El-Refaie and T. M. Jahns, "Scalability of surface PM Machines with concentrated windings designed to achieve wide speed ranges of constant-power operation," *Energy Conversion, IEEE Transactions on,* vol. 21, pp. 362-369, 2006.

[64] A. M. El-Refaie and T. M. Jahns, "Optimal flux weakening in surface PM machines using fractional-slot concentrated windings," *Industry Applications, IEEE Transactions on,* vol. 41, pp. 790-800, 2005.

[65] F. Magnussen and C. Sadarangani, "Winding factors and Joule losses of permanent magnet machines with concentrated windings," in *Electric Machines and Drives Conference, 2003. IEMDC'03. IEEE International*, 2003, pp. 333-339 vol.1.

[66] J. Cros and P. Viarouge, "Synthesis of high performance PM motors with concentrated windings," *Energy Conversion, IEEE Transactions on,* vol. 17, pp. 248-253, 2002.

[67] F. Magnussen, P. Thelin, and C. Sadarangani, "Performance evaluation of permanent magnet synchronous machines with concentrated and distributed windings including the effect of field-weakening," in *Power Electronics, Machines and Drives, 2004. (PEMD 2004). Second International Conference on (Conf. Publ. No. 498)*, 2004, pp. 679-685 Vol.2.

[68] D. Ishak, Z. Q. Zhu, and D. Howe, "Comparison of PM brushless motors, having either all teeth or alternate teeth wound," *Energy Conversion, IEEE Transactions on,* vol. 21, pp. 95-103, 2006.

[69] H. Murakami, H. Kataoka, Y. Honda, S. Morimoto, and Y. Takeda, "Highly efficient brushless motor design for an air-conditioner of the next generation 42 V vehicle," in *Industry Applications Conference, 2001. Thirty-Sixth IAS Annual Meeting. Conference Record of the 2001 IEEE*, 2001, pp. 461-466 vol.1.

[70] F. Rahman and R. Dutta, "A new rotor design of interior permanent magnet machine suitable for wide speed range," in *Industrial Electronics Society, 2003. IECON '03. The 29th Annual Conference of the IEEE*, 2003, pp. 699-704 vol.1.

[71] A. G. Jack, B. C. Mecrow, P. G. Dickinson, D. Stephenson, J. S. Burdess, J. N. Fawcett, and T. Evans, "Permanent magnet machines with powdered iron cores and pre-pressed windings," in *Industry Applications Conference, 1999. Thirty-Fourth IAS Annual Meeting. Conference Record of the 1999 IEEE*, 1999, pp. 97-103 vol.1.

[72] G. De Donato, F. G. Capponi, and F. Caricchi, "Fractional-Slot Concentrated-Winding Axial-Flux Permanent-Magnet Machine With Core-Wound Coils," *Industry Applications, IEEE Transactions on,* vol. 48, pp. 630-641, 2012.

[73] A. Di Gerlando, G. M. Foglia, R. Perini, and M. Ubaldini, "Design and operation aspects of field regulated PM synchronous machines with concentrated armature windings," in *Electric Machines and Drives, 2005 IEEE International Conference on*, 2005, pp. 1165-1172.

[74] L. Alberti and N. Bianchi, "Theory and Design of Fractional-Slot Multilayer Windings," *Industry Applications, IEEE Transactions on,* vol. 49, pp. 841-849, 2013.

[75] Chaifeng, H. Gao, Y. Yu, and S. Cheng, "The research on performances of interior permanent magnet synchronous motor with different pole and slot combinations," in *Electrical Machines and Systems, 2008. ICEMS 2008. International Conference on*, 2008, pp. 3724-3727.

[76] T. Finken, M. Felden, and K. Hameyer, "Comparison and design of different electrical machine types regarding their applicability in hybrid electrical

vehicles," in *Electrical Machines, 2008. ICEM 2008. 18th International Conference on*, 2008, pp. 1-5.

[77] F. Libert and J. Soulard, "Investigation on pole-slot combinations for permanent-magnet machines with concentrated windings," in *International Conference on Electrical Machines (ICEM 04)*, 2004, pp. 5-8.

[78] S. E. Skaar, Ø. Krøve, and R. Nilssen, "Distribution, coil-span and winding factors for PM machines with concentrated windings," in *International Conference on Electrical Machines (ICEM 06)*, 2006, pp. 346-151.

[79] A. M. El-Refaie, Z. Q. Zhu, T. M. Jahns, and D. Howe, "Winding Inductances of Fractional Slot Surface-Mounted Permanent Magnet Brushless Machines," in *Industry Applications Society Annual Meeting, 2008. IAS '08. IEEE*, 2008, pp. 1-8.

[80] L. Chong and M. F. Rahman, "Comparison of d- and q-axis inductances in an IPM machine with integral-slot distributed and fractional-slot concentrated windings," in *Electrical Machines, 2008. ICEM 2008. 18th International Conference on*, 2008, pp. 1-5.

[81] O. K. Soon, K. Sung-Il, Z. Peng, and H. Jung-Pyo, "Performance comparison of IPMSM with distributed and concentrated windings," in *Industry Applications Conference, 2006. 41st IAS Annual Meeting. Conference Record of the 2006 IEEE*, 2006, pp. 1984-1988.

[82] M. Valavi, A. Nysveen, and R. Nilssen, "Magnetic forces and vibration in permanent magnet machines with non-overlapping concentrated windings: A review," in *Industrial Technology (ICIT), 2012 IEEE International Conference on*, 2012, pp. 977-984.

[83] Y. Asano, Y. Honda, H. Murakami, Y. Takeda, and S. Morimoto, "Novel noise improvement technique for a PMSM with concentrated winding," in *Power Conversion Conference, 2002. PCC-Osaka 2002. Proceedings of the*, 2002, pp. 460-465 vol.2.

[84] G. Pellegrino, P. Guglielmi, A. Vagati, and F. Villata, "Core Losses and Torque Ripple in IPM Machines: Dedicated Modeling and Design Tradeoff," *Industry Applications, IEEE Transactions on,* vol. 46, pp. 2381-2391, 2010.

[85] P. Arumugam, T. Hamiti, and C. Gerada, "Modeling of Different Winding Configurations for Fault-Tolerant Permanent Magnet Machines to Restrain Interturn Short-Circuit Current," *Energy Conversion, IEEE Transactions on,* vol. 27, pp. 351-361, 2012.

[86] M. T. Abolhassani and H. A. Toliyat, "Fault tolerant permanent magnet motor drives for electric vehicles," in *Electric Machines and Drives Conference, 2009. IEMDC '09. IEEE International*, 2009, pp. 1146-1152.

[87] A. M. El-Refaie and T. M. Jahns, "Comparison of synchronous PM machine types for wide constant-power speed range operation," in *Industry Applications Conference, 2005. Fourtieth IAS Annual Meeting. Conference Record of the 2005*, 2005, pp. 1015-1022 Vol. 2.

[88] A. M. El-Refaie, T. M. Jahns, P. J. McCleer, and J. W. McKeever, "Experimental verification of optimal flux weakening in surface PM Machines using concentrated windings," *Industry Applications, IEEE Transactions on,* vol. 42, pp. 443-453, 2006.

[89] C. Deak, A. Binder, B. Funieru, and M. Mirzaei, "Extended field weakening and overloading of high-torque density permanent magnet motors," in *Energy Conversion Congress and Exposition, 2009. ECCE 2009. IEEE*, 2009, pp. 2347-2353.

[90] W. L. Soong, P. B. Reddy, A. M. El-Refaie, T. M. Jahns, and N. Ertugrul, "Surface PM Machine Parameter Selection for Wide Field-Weakening Applications," in *Industry Applications Conference, 2007. 42nd IAS Annual Meeting. Conference Record of the 2007 IEEE*, 2007, pp. 882-889.

[91] A. R. Munoz, F. Liang, and M. W. Degner, "Evaluation of Interior PM and Surface PM Synchronous machines with distributed and concentrated windings," in *Industrial Electronics, 2008. IECON 2008. 34th Annual Conference of IEEE*, 2008, pp. 1189-1193.

[92] P. H. Mellor, R. Wrobel, and D. Holliday, "A computationally efficient iron loss model for brushless AC machines that caters for rated flux and field weakened operation," in *Electric Machines and Drives Conference, 2009. IEMDC '09. IEEE International*, 2009, pp. 490-494.

[93] R. Nuscheler, "Two-dimensional analytical model for eddy-current loss calculation in the magnets and solid rotor yokes of permanent magnet synchronous machines," in *Electrical Machines, 2008. ICEM 2008. 18th International Conference on*, 2008, pp. 1-6.

[94] F. Meier and J. Soulard, "Analysis of Flux Measurements on a PMSM With Non-Overlapping Concentrated Windings," in *Industry Applications Society Annual Meeting, 2008. IAS '08. IEEE*, 2008, pp. 1-8.

[95] J. Wang, Z. P. Xia, S. A. Long, and D. Howe, "Radial force density and vibration characteristics of modular permanent magnet brushless ac machine," *Electric Power Applications, IEE Proceedings -,* vol. 153, pp. 793-801, 2006.

[96] S. Araki, T. Kondou, and A. Yamagiwa, "Analyses of electromagnetic forces of concentrated winding permanent magnet brushless motors with rotor eccentricity," in *Electrical Machines and Systems, 2009. ICEMS 2009. International Conference on*, 2009, pp. 1-4.

[97] F. Xu and L. Tiecai, "A research on the radial unbalanced force in the unsymmetrical brushless PM motors," in *Industrial Electronics and Applications, 2008. ICIEA 2008. 3rd IEEE Conference on*, 2008, pp. 1695-1698.

[98] L. Sang-Ho, H. Jung-Pyo, H. Sang-Moon, L. Woo-Taik, L. Ji-Young, and K. Young-Kyoun, "Optimal Design for Noise Reduction in Interior Permanent-Magnet Motor," *Industry Applications, IEEE Transactions on,* vol. 45, pp. 1954-1960, 2009.

[99] H. Seok-Hee, T. M. Jahns, and Z. Q. Zhu, "Analysis of Rotor Core Eddy-Current Losses in Interior Permanent-Magnet Synchronous Machines," *Industry Applications, IEEE Transactions on,* vol. 46, pp. 196-205, 2010.

[100] K. Sung-Il, B. Ji-Hyung, H. Jung-Pyo, and L. Ki-Chae, "Optimization Technique for Improving Torque Performance of Concentrated Winding Interior PM Synchronous Motor with Wide Speed Range," in *Industry Applications Conference, 2006. 41st IAS Annual Meeting. Conference Record of the 2006 IEEE*, 2006, pp. 1933-1940.

[101] Y. Kawaguchi, T. Sato, I. Miki, and M. Nakamura, "A reduction method of cogging torque for IPMSM," in *Electrical Machines and Systems, 2005. ICEMS 2005. Proceedings of the Eighth International Conference on*, 2005, pp. 248-250 Vol. 1.

[102] Y. Kano, T. Terahai, T. Kosaka, N. Matsui, and T. Nakanishi, "A new flux-barrier design of torque ripple reduction in saliency-based sensorless drive IPM motors for general industrial applications," in *Energy Conversion Congress and Exposition, 2009. ECCE 2009. IEEE*, 2009, pp. 1939-1945.

[103] K.-j. Lee, K. Kim, S. Kim, J.-S. Ahn, S. Lim, and L. Ju, "Optimal magnet shape to improve torque characteristics of interior permanent magnet synchronous motor," *Journal of Applied Physics,* vol. 97, pp. 10Q505-10Q505-3, 2005.

[104] S. Y. Lim and L. Ju, "A design for improved performance of interior permanent magnet synchronous motor for hybrid electric vehicle," *Journal of Applied Physics,* vol. 99, pp. 08R308-08R308-3, 2006.

[105] P. M. Lindh, H. K. Jussila, M. Niemela, A. Parviainen, and J. Pyrhonen, "Comparison of Concentrated Winding Permanent Magnet Motors With Embedded and Surface-Mounted Rotor Magnets," *Magnetics, IEEE Transactions on,* vol. 45, pp. 2085-2089, 2009.

[106] P. Salminen, J. Pyrhonen, H. Jussila, and M. Niemela, "Concentrated Wound Permanent Magnet Machines with Different Rotor Designs," in *Power Engineering, Energy and Electrical Drives, 2007. POWERENG 2007. International Conference on*, 2007, pp. 514-517.

[107] K. Ki-Chan, K. Kwangsoo, K. Hee-jun, and L. Ju, "Demagnetization Analysis of Permanent Magnets According to Rotor Types of Interior Permanent Magnet Synchronous Motor," *Magnetics, IEEE Transactions on,* vol. 45, pp. 2799-2802, 2009.

[108] A. M. El-Refaie, M. R. Shah, J. P. Alexander, S. Galioto, K. K. Huh, and W. D. Gerstler, "Rotor End Losses in Multiphase Fractional-Slot Concentrated-Winding Permanent Magnet Synchronous Machines," *Industry Applications, IEEE Transactions on,* vol. 47, pp. 2066-2074, 2011.

[109] H. Polinder, M. J. Hoeijmakers, and M. Scuotto, "Eddy-Current Losses in the Solid Back-Iron of PM Machines for different Concentrated Fractional Pitch Windings," in *Electric Machines & Drives Conference, 2007. IEMDC '07. IEEE International*, 2007, pp. 652-657.

[110] M. Nakano, H. Kometani, and M. Kawamura, "A study on eddy-current losses in rotors of surface permanent-magnet synchronous machines," *Industry Applications, IEEE Transactions on,* vol. 42, pp. 429-435, 2006.

[111] O. Bottauscio, G. Pellegrino, P. Guglielmi, M. Chiampi, and A. Vagati, "Rotor loss estimation in permanent magnet machines with concentrated windings," *Magnetics, IEEE Transactions on,* vol. 41, pp. 3913-3915, 2005.

[112] K. Yamazaki, M. Shina, Y. Kanou, M. Miwa, and J. Hagiwara, "Effect of Eddy Current Loss Reduction by Segmentation of Magnets in Synchronous Motors: Difference Between Interior and Surface Types," *Magnetics, IEEE Transactions on,* vol. 45, pp. 4756-4759, 2009.

[113] W. Jingai, Z. Dongqi, and A. Satake, "The torque research on concentrated winding brushless PM motor," in *TENCON '02. Proceedings. 2002 IEEE Region 10 Conference on Computers, Communications, Control and Power Engineering*, 2002, pp. 2026-2029 vol.3.

[114] I. Abdennadher, R. Kessentini, and A. Masmoudi, "Analytical derivation and FEA validation of the inductances of CWPMM," in *Systems, Signals and Devices, 2009. SSD '09. 6th International Multi-Conference on*, 2009, pp. 1-7.

[115] Q. Ronghai and T. A. Lipo, "General closed-form analytical expressions of air-gap inductances for surface-mounted permanent magnet and induction machines," in *Electric Machines and Drives Conference, 2003. IEMDC'03. IEEE International*, 2003, pp. 443-448 vol.1.

[116] J. K. Tangudu, T. M. Jahns, A. El-Refaie, and Z. Q. Zhu, "Lumped parameter magnetic circuit model for fractional-slot concentrated-winding interior permanent magnet machines," in *Energy Conversion Congress and Exposition, 2009. ECCE 2009. IEEE*, 2009, pp. 2423-2430.

[117] Y. Duan, R. G. Harley, and T. G. Habetler, "Method for multi-objective optimized designs of Surface Mount Permanent Magnet motors with concentrated or distributed stator windings," in *Electric Machines and Drives Conference, 2009. IEMDC '09. IEEE International*, 2009, pp. 323-328.

[118] F. Meier and J. Soulard, "dq theory applied to a permanent magnet synchronous machine with concentrated windings," in *Power Electronics, Machines and Drives, 2008. PEMD 2008. 4th IET Conference on*, 2008, pp. 194-198.

[119] A. Eilenberger, M. Schroedl, and J. Heissenberger, "Comparison of outer rotor PMSM with single- and double-layer windings at same machine geometry with respect to the sensorless control capability," in *Power Electronics and Applications, 2009. EPE '09. 13th European Conference on*, 2009, pp. 1-7.

[120] N. Imai, S. Morimoto, M. Sanada, and Y. Takeda, "Influence of Rotor Configuration on Sensorless Control for Permanent-Magnet Synchronous Motors," *Industry Applications, IEEE Transactions on,* vol. 44, pp. 93-100, 2008.

[121] K. Kojima, M. Hasegawa, T. Ohnuma, M. Tomita, S. Doki, S. Okuma, and K. Matsui, "Position sensorless control by reduced-order extended-flux observer applicable to IPMSM with concentrated windings," in *Power Electronics Electrical Drives Automation and Motion (SPEEDAM), 2010 International Symposium on*, 2010, pp. 1018-1023.

[122] D. D. Reigosa, K. Akatsu, N. Limsuwan, Y. Shibukawa, and R. D. Lorenz, "Self-Sensing Comparison of Fractional Slot Pitch Winding Versus Distributed Winding for FW- and FI-IPMSMs Based on Carrier Signal Injection at Very Low Speed," *Industry Applications, IEEE Transactions on,* vol. 46, pp. 2467-2474, 2010.

[123] D. M. Ionel, "High-efficiency variable-speed electric motor drive technologies for energy savings in the US residential sector," in *Optimization of Electrical and Electronic Equipment (OPTIM), 2010 12th International Conference on*, 2010, pp. 1403-1414.

[124] W. Youlong, X. Wen, X. Shan, F. Tao, and L. Zeng, "Analysis and design of high power factor interior permanent magnet motor with concentrated windings for undersea vehicle propulsion," in *Vehicle Power and Propulsion Conference, 2008. VPPC '08. IEEE*, 2008, pp. 1-6.

[125] M. V. Cistelecan and M. Popescu, "Study of the Number of Slots/Pole Combinations for Low Speed Permanent Magnet Synchronous Generators," in *Electric Machines & Drives Conference, 2007. IEMDC '07. IEEE International*, 2007, pp. 1616-1620.

[126] L. Alberti, M. Barcaro, Pre, x, M. D., A. Faggion, L. Sgarbossa, N. Bianchi, and S. Bolognani, "IPM Machine Drive Design and Tests for an Integrated Starter & Alternator Application," *Industry Applications, IEEE Transactions on,* vol. 46, pp. 993-1001, 2010.

[127] E. V. Kazmin, E. A. Lomonova, and J. J. H. Paulides, "Brushless traction PM machines using commercial drive technology, Part II: Comparative study of the motor configurations," in *Electrical Machines and Systems, 2008. ICEMS 2008. International Conference on*, 2008, pp. 3772-3780.

[128] N. Alatawneh and P. Pillay, "Test Specimen Shape Considerations for the Measurement of Rotational Core Losses," *Energy Conversion, IEEE Transactions on,* vol. 27, pp. 151-159.

[129] L. Yongjian, Z. Jianguo, Y. Qingxin, L. Zhi Wei, G. Youguang, and Z. Chuang, "Study on Rotational Hysteresis and Core Loss Under Three-Dimensional Magnetization," *Magnetics, IEEE Transactions on,* vol. 47, pp. 3520-3523.

[130] G. Youguang, Z. Jian Guo, Z. Jinjiang, L. Haiyan, and J. Jian Xun, "Measurement and Modeling of Rotational Core Losses of Soft Magnetic Materials Used in Electrical Machines: A Review," *Magnetics, IEEE Transactions on,* vol. 44, pp. 279-291, 2008.
[131] M. J. Manyage and P. Pillay, "New Epstein Frame for Core Loss Measurements at High Frequencies and High Flux Densities," in *Industry Applications Society Annual Meeting, 2008. IAS '08. IEEE*, 2008, pp. 1-6.
[132] S. A. Rahman and A. M. Knight, "Influence of design parameters on wide speed range concentrated winding PM machines," in *Electric Machines & Drives Conference (IEMDC), 2011 IEEE International*, 2011, pp. 1001-1006.
[133] M. S. Lancarotte and A. de A.Penteado, Jr., "Estimation of core losses under sinusoidal or nonsinusoidal induction by analysis of magnetization rate," *Energy Conversion, IEEE Transactions on,* vol. 16, pp. 174-179, 2001.
[134] P. Beckley and E. Institution of Electrical, *Electrical steels for rotating machines*: Institution of Electrical Engineers, 2002.
[135] P. K. Rastogi, "Lamination steel technology for appliance industry," *Industry Applications, IEEE Transactions on,* vol. 24, pp. 982-986, 1988.
[136] A. M. Knight and D. G. Dorrell, "Improving the Torque Prediction of Saturated Automotive Drive Machines by Accurate Representation of Saturated Curves," *Magnetics, IEEE Transactions on,* vol. 48, pp. 4630-4633.
[137] Y. Honda, T. Higaki, S. Morimoto, and Y. Takeda, "Rotor design optimisation of a multi-layer interior permanent-magnet synchronous motor," *Electric Power Applications, IEE Proceedings -,* vol. 145, pp. 119-124, 1998.
[138] S. Yul-kyu, K.-Y. Hwang, and K. Byung-Il, "Maximum torque control for optimal design to reduce cogging torque in spoke type interior permanent magnet synchronous motor," in *Energy Conversion Congress and Exposition (ECCE), 2010 IEEE*, pp. 3654-3658.
[139] G. Gallegos-Lopez, F. S. Gunawan, and J. E. Walters, "Optimum torque control of permanent-magnet AC Machines in the field-weakened region," *Industry Applications, IEEE Transactions on,* vol. 41, pp. 1020-1028, 2005.
[140] T. Finken and K. Hameyer, "Design and optimization of an IPMSM with fixed outer dimensions for application in HEVs," in *Electric Machines and Drives Conference, 2009. IEMDC '09. IEEE International*, 2009, pp. 1743-1748.
[141] Z. Q. Zhu, K. Ng, and D. Howe, "Design and analysis of high-speed brushless permanent magnet motors," in *Electrical Machines and Drives, 1997 Eighth International Conference on (Conf. Publ. No. 444)*, 1997, pp. 381-385.
[142] J. Germishuizen and M. Kamper, "Design and Performance Characteristics of IPM Machines with Single Layer Non-Overlapping Concentrated Windings," in *Industry Applications Conference, 2007. 42nd IAS Annual Meeting. Conference Record of the 2007 IEEE*, 2007, pp. 141-147.
[143] M. N. Uddin, T. S. Radwan, and M. Azizur Rahman, "Performance of interior permanent magnet motor drive over wide speed range," *Energy Conversion, IEEE Transactions on,* vol. 17, pp. 79-84, 2002.
[144] B. Jaenam, J. Chang-Sung, K. Won-Ho, J. Ik-sang, W. Sung-Hong, and L. Ju, "Inductance calculation by relative permeance for the IPMSM design," in *Electromagnetic Field Computation (CEFC), 2010 14th Biennial IEEE Conference on*, 2010, pp. 1-1.
[145] M. N. Uddin and F. Abera, "Online loss minimization based vector control of IPMSM drive," in *Electric Machines and Drives Conference, 2009. IEMDC '09. IEEE International*, 2009, pp. 30-35.

[146] E. Armando, P. Guglielmi, G. Pellegrino, M. Pastorelli, and A. Vagati, "Accurate Modeling and Performance Analysis of IPM-PMASR Motors," *Industry Applications, IEEE Transactions on,* vol. 45, pp. 123-130, 2009.

[147] J. Chang-Sung, S. Kim, Y.-H. Kim, and L. Ju, "Design of IPMSM to reduce cogging torque considering tapping the rotor and shape of barrier," in *Telecommunications Energy Conference, 2009. INTELEC 2009. 31st International*, 2009, pp. 1-4.

Appendix A

The core loss curve for 35JN250 are shown in Figure A 1 and the DC magnetisation curve are shown in Figure A 2. These data are provided by the JFE manufacturer. So, the DC magnetisation curve are plotted to the max B value as high as around 2T.

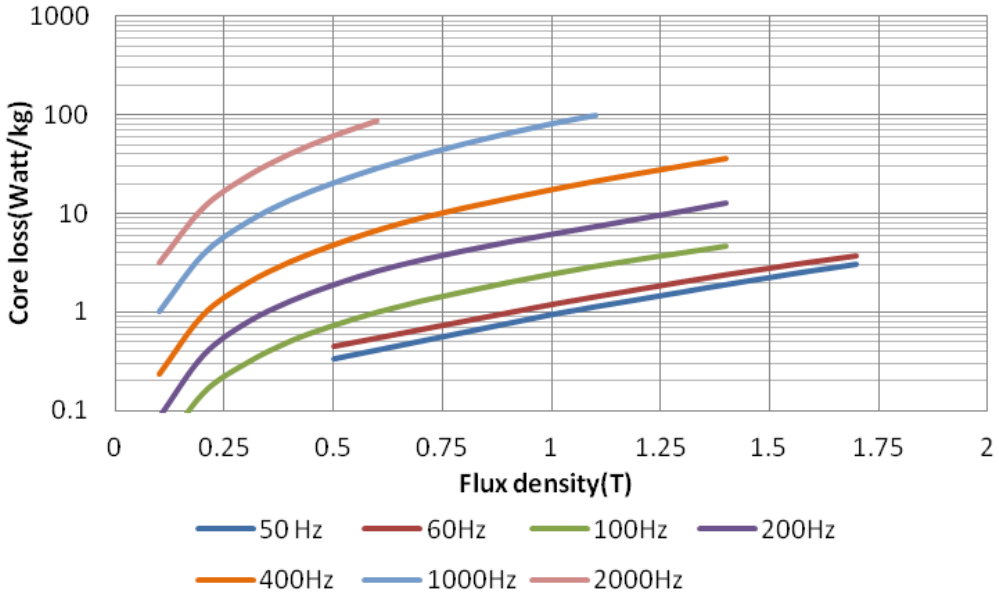

Figure A 1 Core loss curves of 35JN250 core material

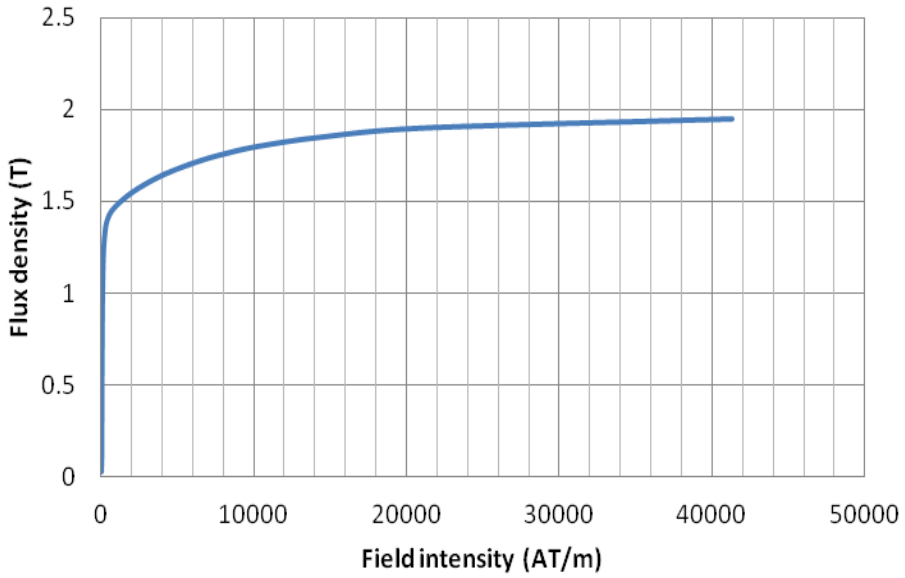

Figure A 2 Initial DC magnetization curve

Appendix B

The d-axis and q-axis voltage numerically can be calculated from the motor parameter are as follows

$$\begin{bmatrix} V_d \\ V_q \end{bmatrix} = \begin{bmatrix} R + pL_d & -\omega L_q \\ \omega L_d & R + pL_q \end{bmatrix} \begin{bmatrix} I_d \\ I_q \end{bmatrix} + \omega \begin{bmatrix} 0 \\ \Psi_m \end{bmatrix}$$

$V_d = RI_d + pI_dL_d - \omega_e L_q I_q$ $pI_dL_d = 0$, $pI_qL_q = 0$ as Id and Iq are time invariant.

$V_q = RI_q + pI_qL_q + \omega_e L_d I_d + \omega_e \Psi_m$ where $p = \frac{d}{dt}$

The FEA analysis can be used to obtain the open circuit voltage. However, d-axis and q-axis voltage at open circuit condition can be obtained from the three phase abc voltage waveform shown as follows. The open circuit d-axis and q-axis voltage is also used to determine the initial angle of the rotor.

And, $V_{qdo}=KV_{abc}$

where $K=\frac{2}{3}\begin{bmatrix} k_{11} & k_{12} & k_{13} \\ k_{21} & k_{22} & k_{23} \\ k_{31} & k_{32} & k_{33} \end{bmatrix}$

$V_q=\frac{2}{3}[K_{11}V_a + K_{12}V_b + K_{13}V_c]$

$V_d=\frac{2}{3}[K_{21}V_a + K_{22}V_b + K_{23}V_c]$

K value can be obtained from the following matrix

$$K = \frac{2}{3}\begin{bmatrix} \cos(\omega_e t - \theta_{(off.e)}) & \cos(\omega_e t - \theta_{(off.e)} - \frac{2\pi}{3}) & \cos(\omega_e t - \theta_{(off.e)} + \frac{2\pi}{3}) \\ \sin(\omega_e t - \theta_{(of.e)}) & \sin(\omega_e t - \theta_{(off.e)} - \frac{2\pi}{3}) & \sin(\omega_e t - \theta_{(off.e)} + \frac{2\pi}{3}) \\ 1/2 & 1/2 & 1/2 \end{bmatrix}$$

Where $\theta_{(off.e)}$ in radians

Three cases using the 35JN250 core materials are investigated to find out the suitable magnet orientation. Harmonics core losses for all the cases at open circuit condition are

shown in Figure B 1 and Harmonics core losses for all the cases at loaded condition are shown in Figure B 2.

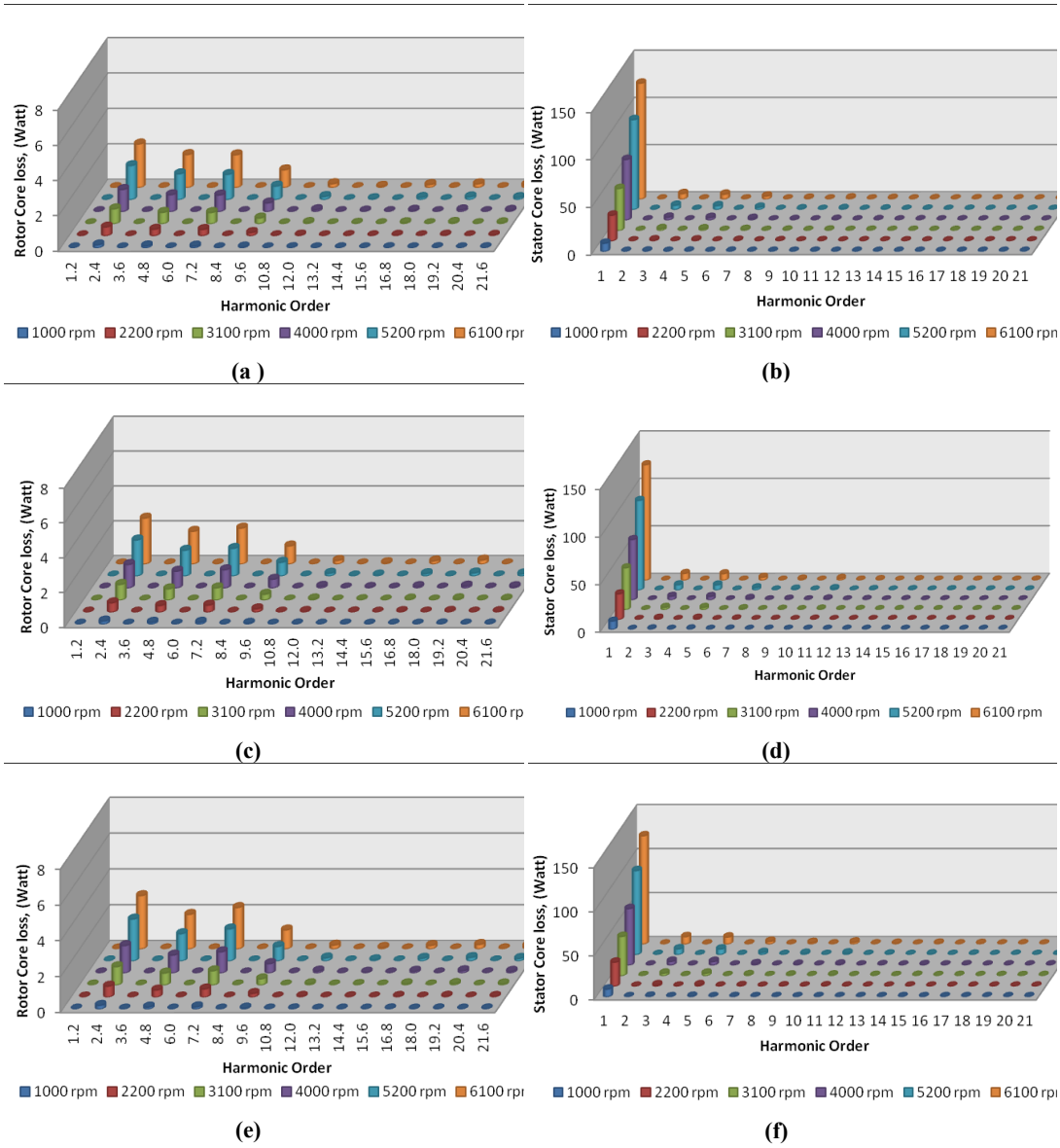

Figure B 1 Core loss harmonics of machine used 35JN250 materials at open circuit condition (a) case1-rotor (b) Case1-Stator (c) case2-Rotor (b) Case2-Stator (a) case3-rotor (b) Case3-Stator

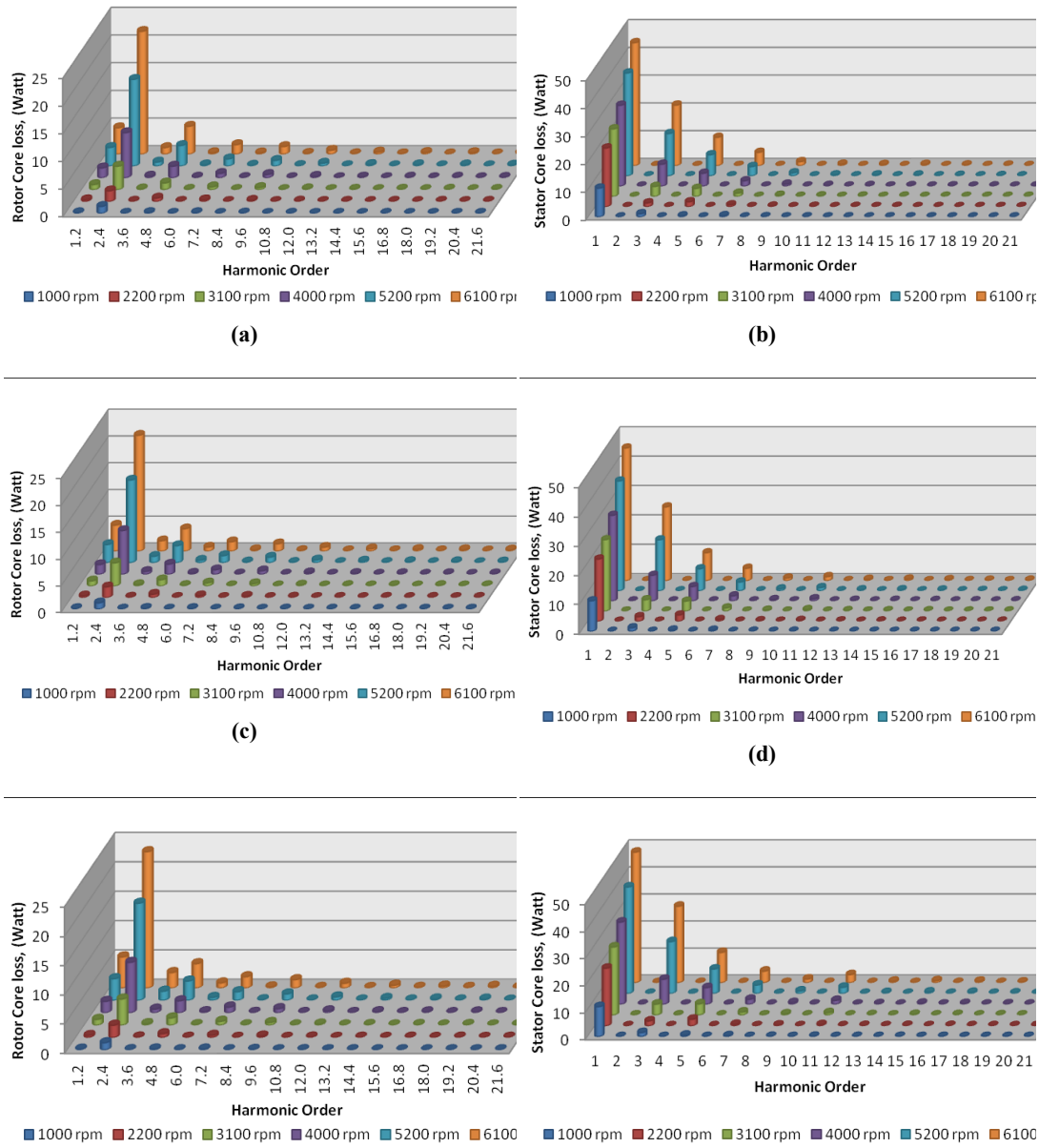

Figure B 2 Core loss harmonics of machine used 35JN250 materials at loaded condition (a) case1-rotor (b) Case1-Stator (c) case2-Rotor (b) Case2-Stator (a) case3-rotor (b) Case3-Stator

Appendix C

Harmonics core loss at different speed level (1000rpm, 2000rpm, 3000rpm, 4000rpm) under open circuit condition for SRA and non-SRA are shown in Figure C 1. The figure shows that the rotor core losses are negligible compared with corresponding stator core losses. However, all harmonics core loss in stator is zero except the fundamental stator core loss which contributes almost equal amount of the open circuit core loss. Harmonics core loss at different speed level (1000rpm, 2000rpm, 3000rpm, and 4000rpm) under loaded condition for SRA and non-SRA are shown in Figure C 2. The rotor harmonics core loss take part with stator core loss to produce total core loss. The fundamental stator harmonics core loss at loaded condition are less compared with corresponding fundamental stator core loss at open circuit condition mainly due to flux weakening at loaded condition. In both open circuit and loaded condition the SRA machine gives the lower harmonics losses corresponding with harmonics losses of non-SRA machines.

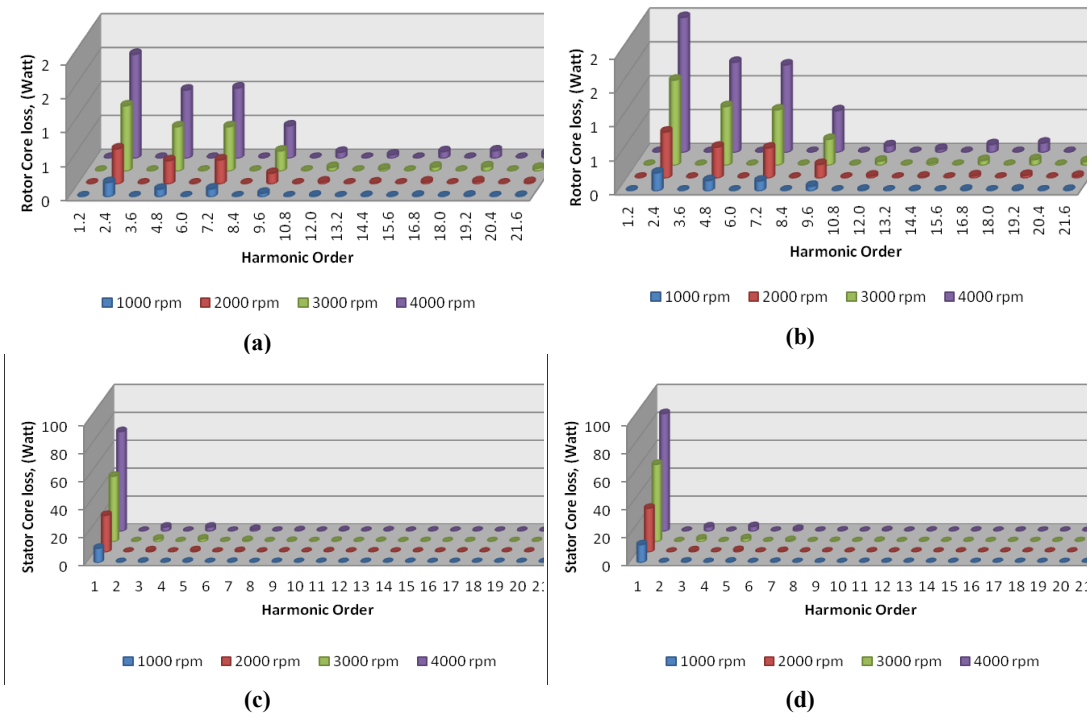

Figure C 1 Core loss harmonics of rotors (a) SRA (b) Non-SRA and Stator (c) SRA (d) Non -SRA at open circuit condition

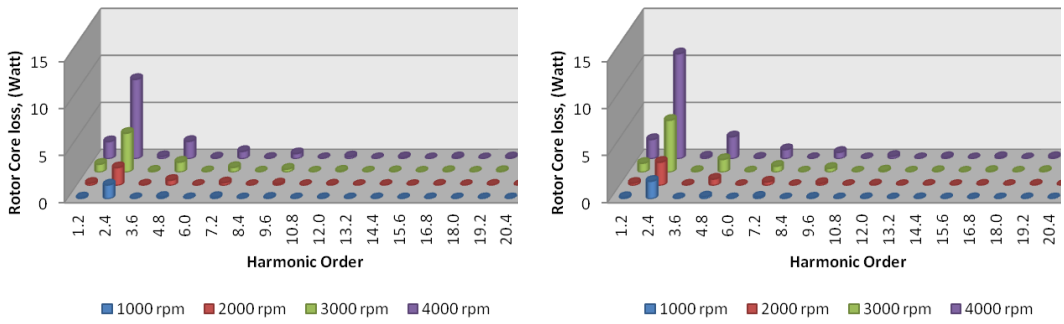

(a) **(b)**

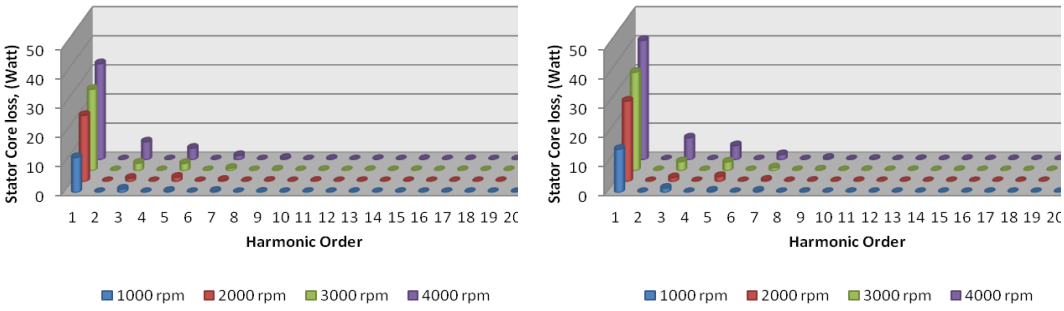

(c) **(d)**

Figure C 2 Core loss harmonics of rotors (a) SRA (b) Non-SRA and Stator (c) SRA (d) Non -SRA at loaded condition